Supporting Information

Neutralization of Reactive Oxygen Species at Dinuclear Cu(II) Cores: Tuning the Anti-Oxidant Manifold in Water by Ligand Design

Andrea Squarcina[a], Alice Santoro[a], Neal Hickey[b], Rita De Zorzi,[b] Mauro Carraro[a], Silvano Geremia[b], Marco Bortolus [a], Marilena Di Valentin [a], Marcella Bonchio[a]

[a]ITM-CNR and Department of Chemical Sciences, University of Padova,
Via Marzolo 1, 35131 Padova, Italy.
[b]Department of Chemical and Pharmaceutical Sciences, University of Trieste,
Via Licio Giorgieri 1, 34127 Trieste, Italy.

To whom correspondence should be addressed. E-mail: marcella.bonchio@unipd.it

Table of Content:

1. General Information

1.1 Materials

Commercially available reagents were used directly, unless otherwise noted. Copper (II) perchlorate hydrate, xanthine, xanthine oxidase from bovine milk, cytochrome c from horse heart, catalase from bovine liver, morin, di-2-pyridyl ketone, hydroxylamine hydrochloride, pyridine, ammonium acetate, sodium bromide, zinc powder, salicylaldehyde, 2-hydroxy-5-nitrobenzaldehyde, sodium borohydride, sodium triacetoxyborohydride, formaldehyde aqueous solution 37 % wt, hydrogen peroxide solution 30% wt, triethylamine, diethyl ether, dichloromethane, 1,2-dichloroethane, methanol, acetonitrile, magnesium sulphate, sodium dihydrogen phosfate, boric acid, were purchased by Sigma-Aldrich. Silica gel (particle size 0.040-0.064 mm, 230-400 mesh) was purchased by Machery-Nagel. Milli-Q water was used to prepare all of the buffer solutions. The ligands 2-{[[di(2-pyridyl)methyl](methyl)amino]methyl} phenol (HL^1) and 2-(((di(pyridin-2-yl)methyl)amino)methyl)-4-nitrophenol (HL^3) were synthesized according to the literature procedures.[S1,S2]

1.2 Instrumentation

UV-Vis spectra were recorded with an UV-Vis Varian Cary 100 for the SOD activity determination and an UV-Vis Varian Cary 50 for other measures. FT-IR spectra of the KBr pellets of the compounds were recorded on a Nicolet 5700 FT-IR instrument. Cyclic voltammetry experiments were performed using a BAS Cell C3 EC-epsilon potentiostat. A standard three-electrode electrochemical cell was used. Glassy carbon electrode (3 mm diameter, geometric surface area = 7 mm^2) from BAS and a Pt wire were used respectively as working and auxiliary electrode. Potentials were referred to an Ag/AgCl/(3 M NaCl) reference electrode. Prior to each experiment, the electrode was polished with 1 µm alumina, rinsed with deionised water and wiped with a paper tissue. Potential were then reported vs NHE. ESI-MS measurements were carried out by using an Agilent Technologies MSD SL Trap mass spectrometer with ESI source. Sample solutions in water with 0.1 % v/v HCOOH were injected into the ion source without the addition of any other solvent at a flow rate of 50 µL/min. For electrospray ionization, the drying gas (nitrogen) was heated at 325 °C. Each species is indicated with the m/z value of the first peak of its isotopic cluster. The peaks in ESI-MS spectra were assigned by comparing the experimental isotopic patterns with the corresponding simulated profiles. EPR spectra were recorded on an ELEXSYS E580 spectrometer equipped with a rectangular cavity, ER4102ST, both from Bruker, Germany, and fitted with a cryostat (ESR900) and a variable-temperature controller (ITC503S), both from Oxford Instruments, UK. All experiments were performed at 50 K on samples frozen in dry ice and sealed under vacuum in quartz tubes (i.d. 3 mm, o.d. 4 mm). The experiments were performed using the following parameters: microwave frequency 9.35 GHz, microwave power 6.4 mW (attenuation 15

dB), sweep width 150 mT, center field 300 mT, conversion time 82 ms, time constant 82 ms, modulation amplitude 0.95 mT, 1024 points, 3 averages.

2. Synthetic Procedures

2.1. Synthesis of $Cu_2L^1_2$

185 mg (0.5 mmol) of $Cu(ClO_4)_2 \cdot 6H_2O$ and ligand 2-{[[di(2-pyridyl)methyl](methyl)amino]methyl}phenol (150 mg, 0.5 mmol) were dissolved in 10 mL of methanol. After all solids were dissolved, an excess of triethylamine was added (80 µL, 0.6 mmol) and the solution turned dark green. After stirring, a formation of a green precipitate occurred. The solution was heated until boiling and gradually acetonitrile was added until complete dissolution of the solid. The solution was then let cool down. After a week green crystals were obtained, washed with methanol and ether and finally dried under vacuum. Yield: 153 mg, 56 %. UV-Vis (H_2O): λ_{max}/nm (ε/M^{-1} cm^{-1}) 269 ($2.1 \cdot 10^4$), 410 ($1.0 \cdot 10^3$). FT-IR (KBr): ν (cm^{-1}) 3089(w), 3024(w), 3005(w), 2926(w), 2906(w), 2867(w), 2855(w), 2819(w), 1614(m), 1603(m), 1598(sh), 1574(w), 1480(s), 1453(s), 1448(sh), 1426(w), 1292(m), 1264(m), 1246(m), 1234(m), 1093(s), 984(m), 893(m), 885(m), 781(m), 768(s), 758(s), 623(s), 554(w), 543(w). ESI(+)-MS m/z calcd. for ($C_{38}H_{36}Cu_2N_6O_2^{2+}$+$HCO_2^-$) (M+$HCO_2^-$) 779.1, found 779.0 and ($C_{38}H_{36}Cu_2N_6O_2^{2+}$+$ClO_4^-$) (M+ ClO_4^-) 833.1, found 833.0. Elemental Analysis, calcd. for $C_{38}H_{36}Cl_2Cu_2N_6O_{10}$: C = 48.83, H = 3.88, N = 8.99; found C = 48.65, H = 3.92, N = 8.85.

2.2. Synthesis of $Cu_2L^2_2$

75 mg (0.2 mmol) of $Cu(ClO_4)_2 \cdot 6H_2O$ and ligand 2-({[di(2-pyridyl)methyl]amino}methyl)phenol (60 mg, 0.2 mmol) were dissolved in 5 mL of ethanol. After all solids were dissolved, an excess of triethylamine was added (35 µL, 0.25 mmol) and the solution turned dark green. After stirring, the formation of a green precipitate occurred. The solution was heated until boiling and gradually DMF was added until complete dissolution of the solid. The solution was then let cool down. After a week green crystals were obtained, washed with methanol and ether and finally dried under vacuum. Yield: 50 mg, 55 %. UV-Vis (H_2O): λ_{max}/nm (ε/M^{-1} cm^{-1}) 265.1 ($2.3 \cdot 10^4$), 397.4 ($3.6 \cdot 10^3$), 667.5 ($6.2 \cdot 10^2$). FT-IR (KBr): ν (cm^{-1}) 3239(w), 3094(w), 3070(w), 3034(sh), 2925(w), 2870(w), 1680(sh), 1658(s), 1610(s), 1597(s), 1573(m), 1482(s), 1471(s), 1452(s), 1441(s), 1389(m), 1291(w), 1273(w), 1248(m), 1098(s), 1002(m), 928(w), 882(m), 868(w), 791(w), 778(m), 758(m), 699(w), 640(w), 625(m), 598(w), 551(w), 473 (w). ESI(+)-MS m/z calcd. for ($C_{36}H_{32}Cu_2N_6O_2^{2+}$-$H^+$) (M-$H^+$) 705.1, found 705.0 ($C_{36}H_{32}Cu_2N_6O_2^{2+}$+$HCO_2^-$) (M+$HCO_2^-$) 751.1, found 751.0 and ($C_{36}H_{32}Cu_2N_6O_2^{2+}$+$ClO_4^-$) (M+$ClO_4^-$) 805.1, found 805.0. Elemental Analysis, calcd. for $C_{36}H_{32}Cl_2Cu_2N_6O_{10} \cdot$DMF: C = 47.81, H = 4.01, N = 10.01; found C = 47.62, H = 4.23, N = 10.24.

2.3. Synthesis of $Cu_2L^3_2$

68 mg (0.18 mmol) of $Cu(ClO_4)_2 \cdot 6H_2O$ and ligand 2-({[di(2-pyridyl)methyl]amino}methyl)-4-nitrophenol (60 mg, 0.18 mmol) were dissolved in 5 mL of ethanol. After all solids were dissolved, an excess of triethylamine was added (35 µL, 0.25 mmol) and the solution turned dark green. After stirring, the formation of a green precipitate occurred. The solution was heated until boiling and gradually DMF was added until complete dissolution of the solid. The solution was then let cool down. After a week green crystals were obtained, washed with methanol and ether and finally dried under vacuum. Yield: 80 mg, 45 %. UV-Vis (H_2O): λ_{max}/nm ($\varepsilon/M^{-1}\,cm^{-1}$) 255.9 ($2.1 \cdot 10^4$), 375.8 ($2.3 \cdot 10^3$), 652.1 ($2.4 \cdot 10^2$). FT-IR (KBr): ν ($cm^{-1}$) 3228(w), 3089(w), 2971(w), 2921(w), 1599(s), 1575(m), 1504(sh), 1478(s), 1442(m), 1332(s), 1297(s), 1263(s), 1119(sh), 1096(s), 1056(m), 1006(w), 934(w), 903(w), 840(w), 789(w), 760(w), 652(w), 624(m), 559(w), 467(w). ESI(+)-MS m/z calcd. for ($C_{36}H_{31}Cu_2N_7O_4^{2+}+HCO_2^-$) ($M+HCO_2^-$) 841.1, found 841.1 and ($C_{36}H_{31}Cu_2N_7O_4^{2+}+ClO_4^-$) ($M+ ClO_4^-$) 895.1, found 895.0. Elemental Analysis, calcd. for $C_{36}H_{30}Cl_2Cu_2N_8O_{14}$: C = 43.38, H = 3.03, N = 11.24; found C = 43.09, H = 3.16, N = 10.92.

Caution: Although the salts and the complexes reported do not appear to be mechanically sensitive, perchlorates should be treated with due caution.

3. X-Ray Diffraction Analysis

Diffraction data from single crystals of dinuclear complexes [$\mathbf{Cu_2L^1_2}$], [$\mathbf{Cu_2L^2_2}$] and [$\mathbf{Cu_2L^3_2}$] were collected by the rotating crystal method using synchrotron radiation at the XRD1 beam-line of the Elettra Synchrotron, Trieste, Italy. In all cases, a single crystal of the complex was dipped in the paratone cryoprotectant and flash-frozen to 100 K in a stream of N_2 vapour. Diffraction images were indexed and integrated using the XDS package and the resulting data sets were scaled using XSCALE.[S3,S4] The structure of [$\mathbf{Cu_2L^1_2}$] was solved in space group P-1 with SHELXS (Direct Methods); while the structures of complexes [$\mathbf{Cu_2L^2_2}$] and [$\mathbf{Cu_2L^3_2}$] were solved in space groups P-1 and $P2_1/a$, respectively, with SIR-2014 (VLD and Patterson Phasing, respectively). Refinements were implemented with SHELXL-14, operating through the WinGX GUI, by full-matrix least-squares (FMLS) methods on F^2.[S5-S7] Thermal parameters of all non-hydrogen atoms were refined anisotropically. Hydrogen atoms were placed at the geometrically calculated positions and refined using the riding model. Crystal data and final refinement details for the three complexes are reported in Table S1. The asymmetric unit of [$\mathbf{Cu_2L^1_2}$] contains one half of the dinuclear dimer, a perchlorate ion and two acetonitrile solvent molecules. Extinction correction was applied using the card EXTI in SHELXL-14.[S6] The asymmetric unit of [$\mathbf{Cu_2L^2_2}$] contains one half of the dinuclear dimer, which includes a DMF molecule to complete the coordination sphere, a perchlorate anion and half an ethanol molecule. All atoms of the perchlorate anion are disordered in two positions and the occupancies were refined freely to 0.73/0.27. DFIX and DANG restraints were applied, using idealised tetrahedral bond lengths and angles as targets, to maintain the tetrahedral

geometry. The ethanol molecule lays on an inversion centre and was refined at half occupancy. DFIX and DANG instructions were used to restrain distances and angles. EADP restraints were used to restrain the thermal parameters of selected atoms of the perchlorate ions and DMF molecule, while thermal parameters of the ethanol molecule were restrained with RIGU, SIMU and ISOR instructions. A FLAT instruction was used to maintain all the non-hydrogen atoms of the DMF molecule on a single plane. Analogously to [$\mathbf{Cu_2L^2_2}$], the asymmetric unit of [$\mathbf{Cu_2L^3_2}$] contains one half of the dinuclear dimer, which includes a dimethylformamide (DMF) molecule to complete the coordination sphere, a perchlorate anion and half an ethanol molecule. During refinement restrains were applied to disordered and/or partially occupied atoms, as outlined below. The DMF molecule in the coordination sphere is disordered in two positions, with the coordinating oxygen atom common to both disordered fragments at full occupancy. The occupancies of the disordered atoms were freely refined to 0.54/0.46. Bond lengths and angles were restrained with DFIX and DANG instructions using the idealised values as targets. The perchlorate anion is disordered in two positions around a 3-fold common axis and the occupancies of the disordered atoms were freely refined to 0.74/0.26. Bond lengths and angles were restrained with DFIX instructions using the idealised values as targets. Finally, the ethanol molecule lays on an inversion centre and was refined at half occupancy. Distances and angles were restrained with DFIX and DANG instructions using idealised values as targets. EADP instructions were used to restrain thermal parameters of selected disordered atoms of the perchlorate and DMF fragments.

Table S1: Crystallographic data for complexes [$Cu_2L^1_2$], [$Cu_2L^2_2$] and [$Cu_2L^3_2$].

	$Cu_2L^1_2$	$Cu_2L^2_2$	$Cu_2L^3_2$
Formula	$C_{38}H_{36}N_6O_2Cu_2 \cdot 2(ClO_4)$	$C_{42}H_{46}N_8O_4Cu_2 \cdot 2(ClO_4)$	$C_{42}H_{44}N_{10}O_8Cu_2 \cdot 2(ClO_4)$
Temperature (K)	100	100	100
Wavelength (Å)	0.8	0.7	0.7
Crystal system	Triclinic	Triclinic	Monoclinic
Space group	P-1	P-1	P21/a
a (Å)	8.911 (2)	8.704 (3)	12.048 (9)
b (Å)	11.282 (2)	12.259 (2)	18.859 (6)
c (Å)	13.011 (3)	12.347 (1)	12.560 (10)
α (°)	111.76 (3)	108.18 (2)	90
β (°)	95.18 (3)	97.25 (3)	116.69 (6)
γ (°)	101.80 (3)	101.81 (3)	90
V (Å^3)	1169.2 (5)	1199.3(5)	2550 (3)
Z, ρ_{calc} (g.mm^{-3})	1, 1.561	1, 1.522	2, 1.549
μ (mm^{-1})	1.446	1.025	0.976
F (000)	566	568	1224
Data collection θ range	3.359 – 29.966	1.747 - 25.993	2.080 – 33.042
Refl. Collected / unique	7080 / 3992	15469 / 4503	25463 / 8639
R_{int}	0.0112	0.0650	0.0379
Completeness (%)	84.1	91.5	85.5
Data/Restraints/Parameters	3992 / 0 / 320	4503 / 64 / 338	8639 / 39 / 369
GooF	1.185	1.074	1.029
R_1, wR_2 [I>2σ(I)]	0.0328 / 0.0903	0.0784 / 0.2122	0.0569 / 0.1637
R_1, wR_2 all data	0.0328 / 0.0904	0.0916 / 0.2273	0.0772 / 0.1842

CCDC code	1564618	1564619	1564620

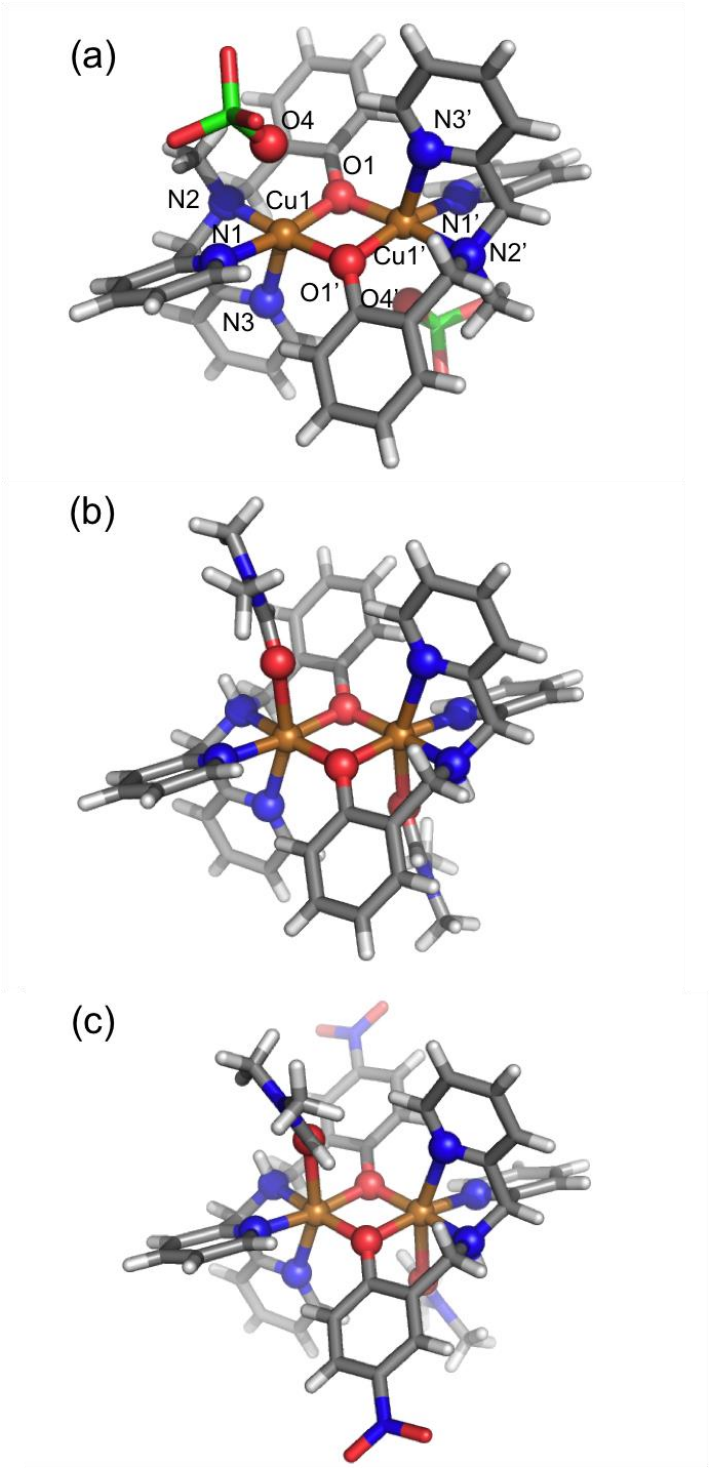

Figure S1. Crystallographic structures of [$\mathbf{Cu_2L^1_2}$] (a), [$\mathbf{Cu_2L^2_2}$] (b) and [$\mathbf{Cu_2L^3_2}$] (c). For clarity, counter ions and solvent molecules which are not part of the Cu coordination spheres have been omitted. The atom numbering scheme for [$Cu_2L^2_2$] and [$Cu_2L^3_2$] is the same as that shown for [$Cu_2L^1_2$], with the exception of oxygen atoms O4 and the inversion related O4' of the perchlorate ions and the O2 and O2' atoms of the DMF molecules.

Table S2: Bond lengths, bond angles and interatomic distances around the Cu – Cu sites in complexes $[Cu_2L^1_2]$, $[Cu_2L^2_2]$ and $[Cu_2L^3_2]$. Atom numbering scheme is reported in Figure S1.

Distances (Å) and Angles (°) [a]	$Cu_2L^1_2$	$Cu_2L^2_2$	$Cu_2L^3_2$
	Equatorial Distances		
Cu1 – N1	1.9993(18)	2.020(4)	2.018(3)
Cu1 – N2	2.0315(16)	1.998(4)	1.980(2)
Cu1 – O1	1.9614(17)	1.988(3)	2.011(2)
Cu1 – O1’	1.9578(14)	1.951(3)	1.952(2)
Cu1 ····· Cu1’	3.0072(10)	3.015(1)	3.033(3)
	Cis Angles		
N1 – Cu1 – N2	81.16(7)	80.72(16)	81.52(11)
O1 – Cu1 – O1’	79.78(7)	80.09(14)	80.14(9)
N1 – Cu1 – O1’	105.09(7)	106.01(16)	106.19(10)
N2 – Cu1 – O1	93.88(6)	93.40(14)	92.50(10)
N3 - Cu1 – N1	86.10(7)	81.64 (17)	82.94(9)
N3 - Cu1 – N2	78.93(6)	74.23 (16)	76.35(8)
N3 - Cu1 – O1	102.06(6)	100.65 (15)	101.47(7)
N3 - Cu1 – O1’	102.31(6)	103.29 (15)	101.83(8)
“O” – Cu1 – O1 [b]	92.58 (7)	92.07 (17)	89.24 (9)
“O” – Cu1 – O1’ [b]	90.20 (7)	91.53 (17)	95.31 (9)
“O” – Cu1 – N1	78.27 (7)	84.27 (19)	84.32 (10)
“O” – Cu1 – N2	90.05 (7)	92.30 (18)	88.15 (11)
Cu1-O1-Cu1’	100.22(7)	99.91(14)	99.86(9)
	Axial Distances		
Cu1-N3	2.3265(14)	2.525 (4)	2.438(2)
Cu1-“O” [b]	2.9893(19)	2.446 (5)	2.485 (3)
	Trans Angles		
N1 – Cu1 – O1	169.54(6)	172.92(16)	171.33(8)
N2 – Cu1 – O1’	173.65(5)	172.55(14)	171.80(9)
N3 – Cu1 -“O” [b]	162.19 (6)	161.87 (18)	161.20 (8)

[a] Symmetry related atoms are distinguished by the prime symbol.

[b] In the case of $Cu_2L^1_2$ “O” is an oxygen atom of a perchlorate ion, while for the other two complexes it is the oxygen atom of a DMF molecule.

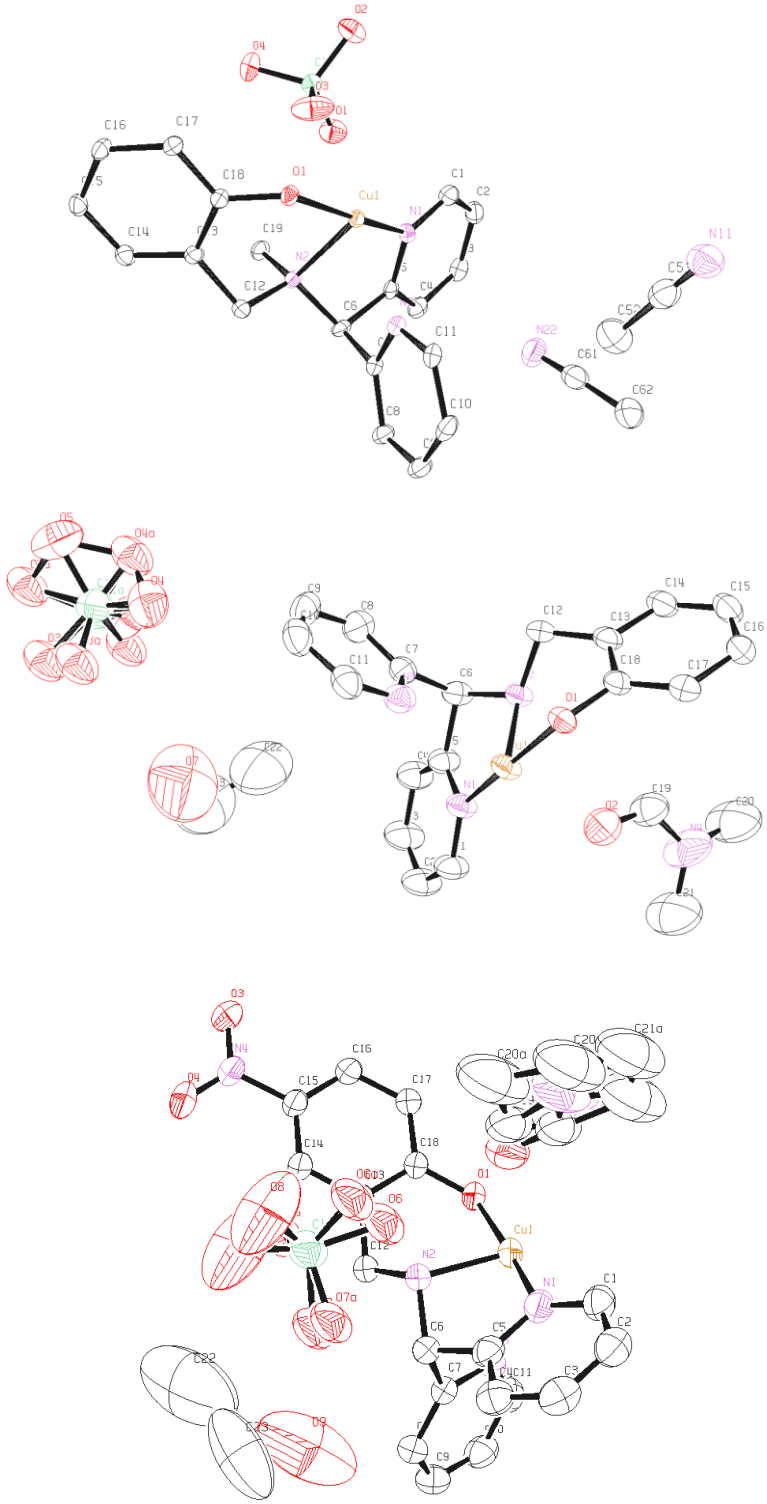

Figure S2. ORTEP views of the structures of [$Cu_2L^1_2$] (a), [$Cu_2L^2_2$] (b) and [$Cu_2L^3_2$] (c). Carbon atoms are depicted as grey ellipsoids, oxygen atoms as red ellipsoids, nitrogen atoms as pink ellipsoids, chlorine atoms as green ellipsoids and copper atoms as orange ellipsoids. Ellipsoid probability is set to 50%. Hydrogen atoms have been omitted for clarity.

4. UV-Vis Spectra

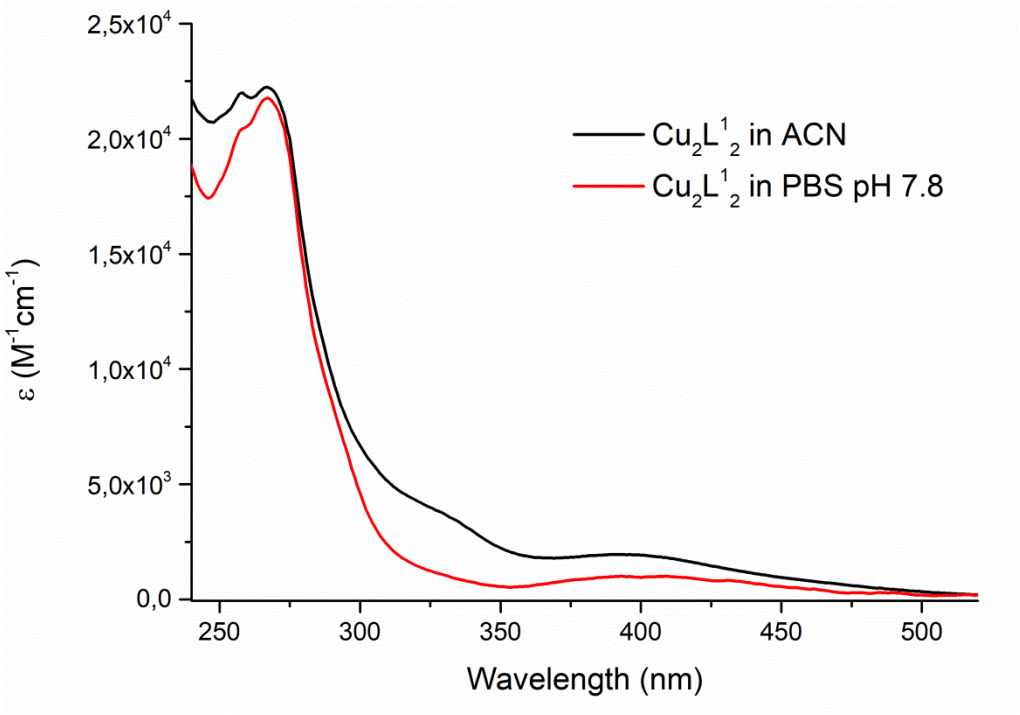

Figure S3. UV-Vis spectra of **$Cu_2L^1_2$**, in phosphate buffer 50 mM, pH 7.8 (red line), in CH_3CN (black line).

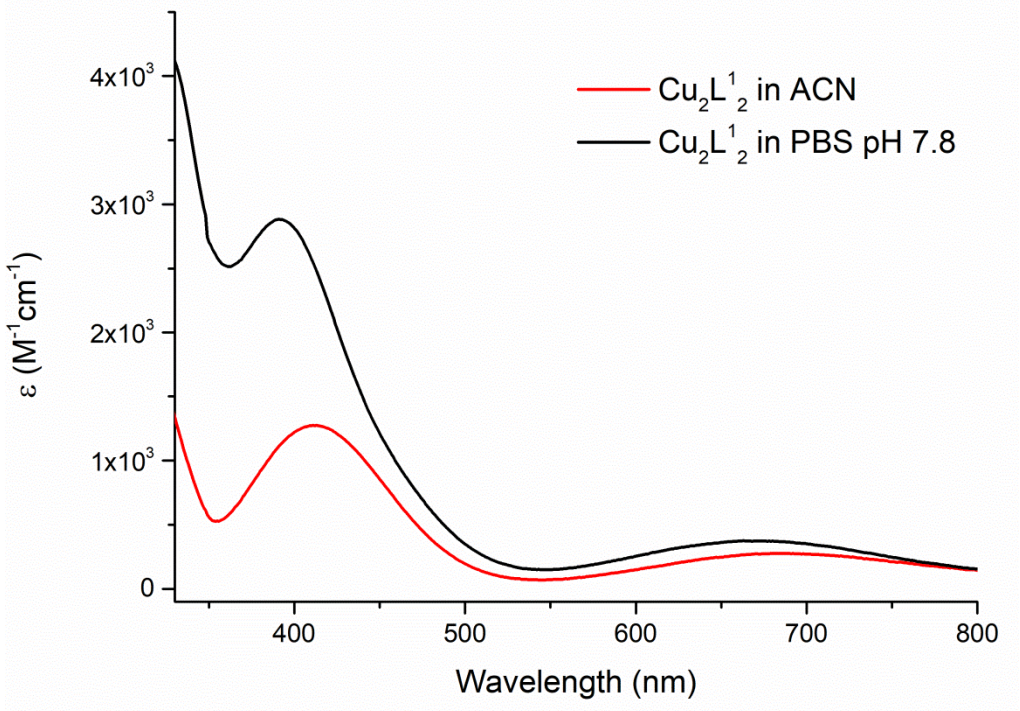

Figure S4. UV-Vis spectra of **$Cu_2L^1_2$** in phosphate buffer 50 mM pH = 7.8, λ_{max}/nm (ε/M^{-1} cm^{-1}) 410 ($1.3\cdot10^3$) (LMCT band) and 675 ($2.9\cdot10^2$) (d-d band) (red line), in CH_3CN (black line) 391 ($2.9\cdot10^3$) (LMCT band) and 670 ($3.7\cdot10^2$) (d-d band).

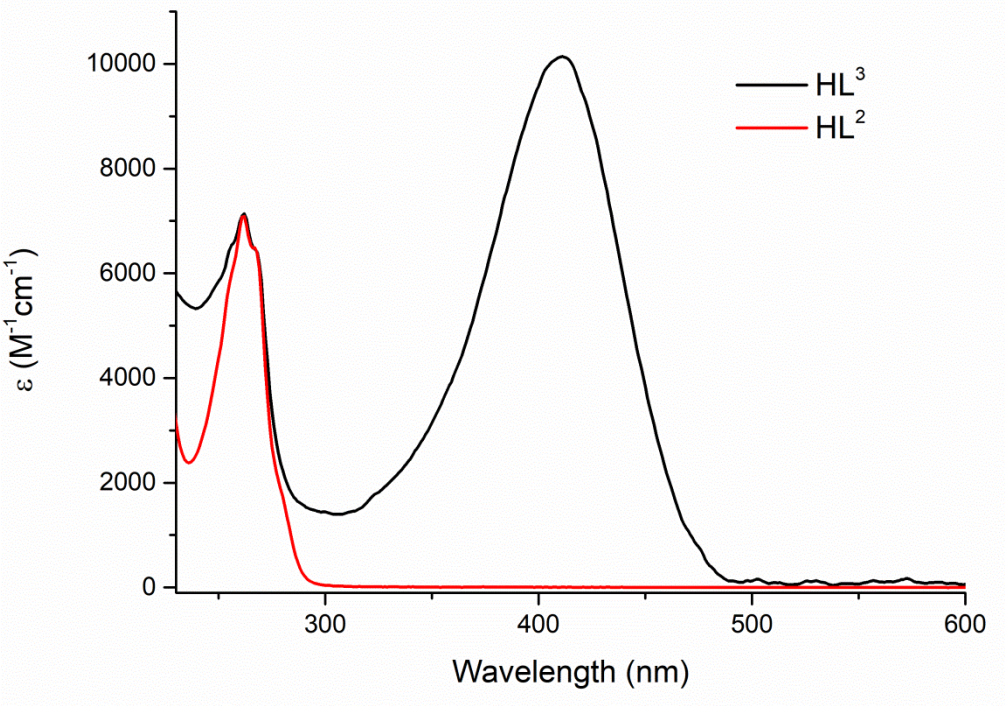

Figure S5. UV-Vis spectra of **HL²**, λ_{max}/nm (ε/M^{-1} cm^{-1}) 261.5 (7.1·10³), 266.7 (6.5·10³)(red line) and **HL³** 261.9 (7.1·10³), 410.9 (1.0·10⁴) (black line) in phosphate buffer 50 mM pH 7.8.

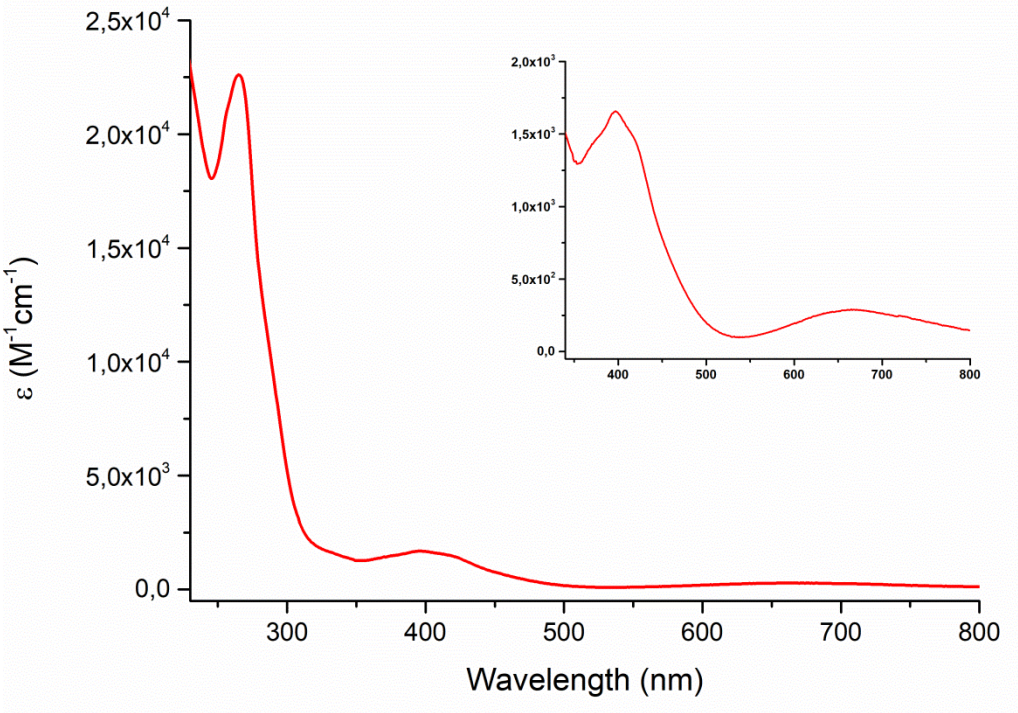

Figure S6. UV-vis spectrum of **$Cu_2L^2_2$** in phosphate buffer 50 mM pH = 7.8, λ_{max}/nm (ε/M^{-1} cm^{-1}) 265(2.3·10⁴), 397 (1.7·10³) (LMCT band) and 668 (2.9·10²) (d-d band). The inset highlights the LMCT and d-d bands.

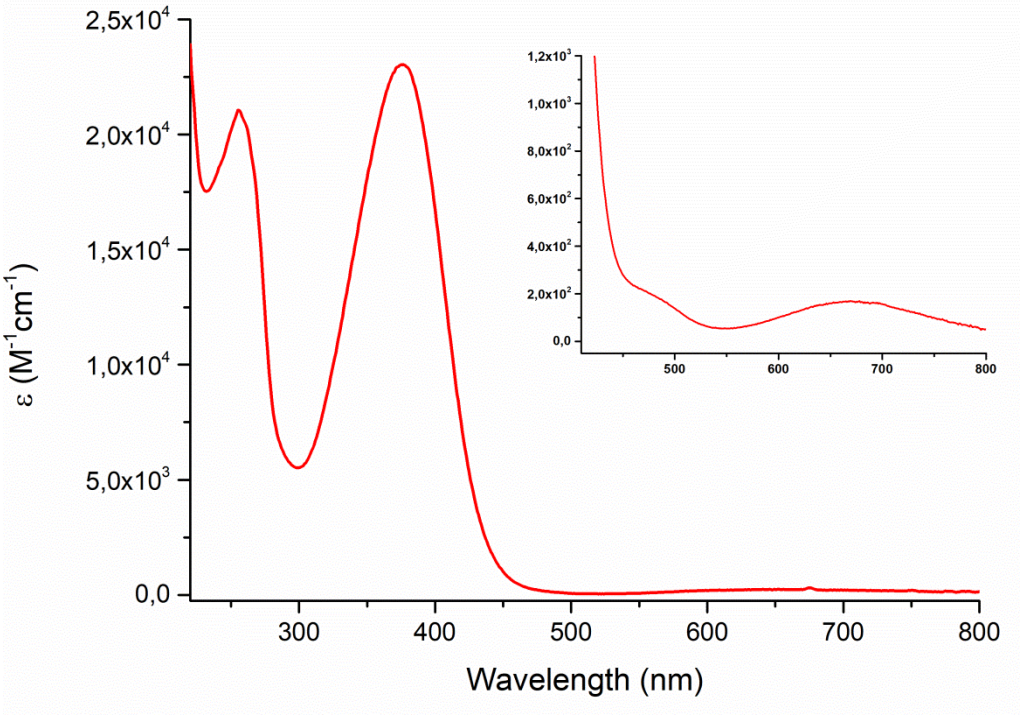

Figure S7. UV-vis spectrum of $Cu_2L^3_2$ in phosphate buffer 50 mM pH = 7.8, λ_{max}/nm (ε/M^{-1} cm^{-1}) 256 ($2.1\cdot10^4$), 376 ($2.3\cdot10^4$) and 670 ($1.7\cdot10^2$) (d-d band). The inset highlights the LMCT and d-d bands.

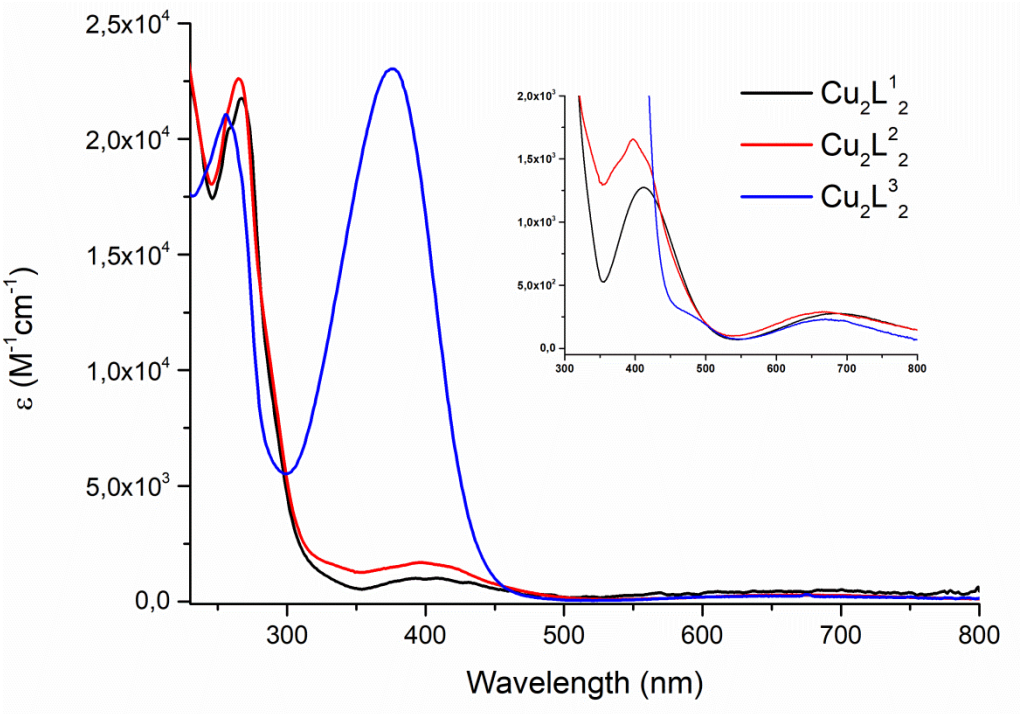

Figure S8. Comparison of the UV-Vis spectra of $Cu_2L^1_2$, $Cu_2L^2_2$ and $Cu_2L^3_2$ in phosphate buffer 50 mM pH 7.8. The inset highlights the LMCT and d-d bands.

5. FT-IR Spectra

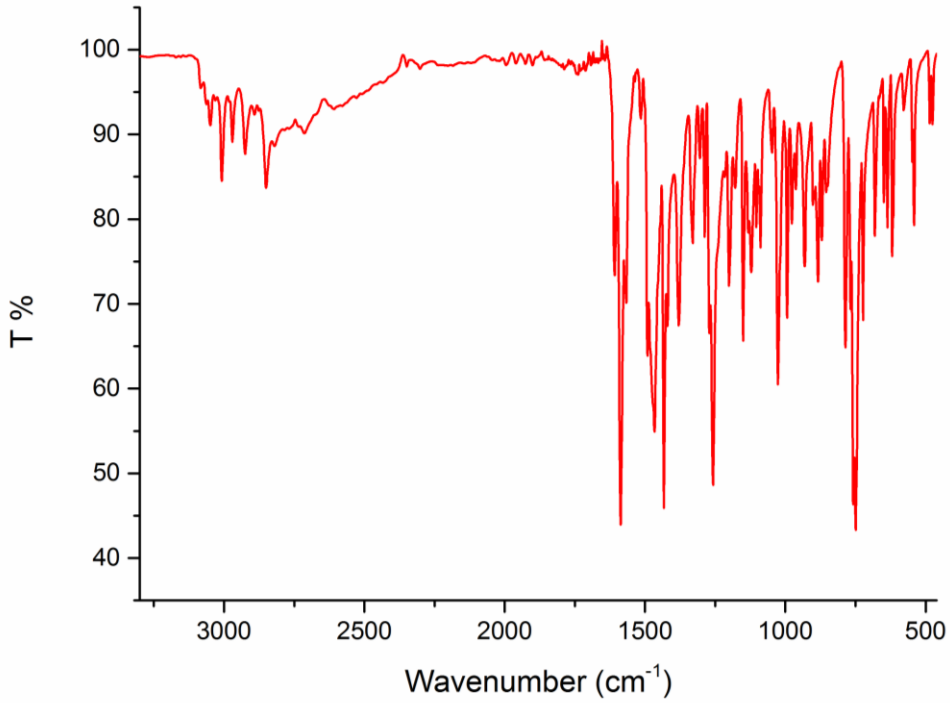

Figure S9. FT-IR spectrum (KBr pellet) of 2-{[[di(2-pyridyl)methyl](methyl)amino]methyl}phenol (**HL¹**).

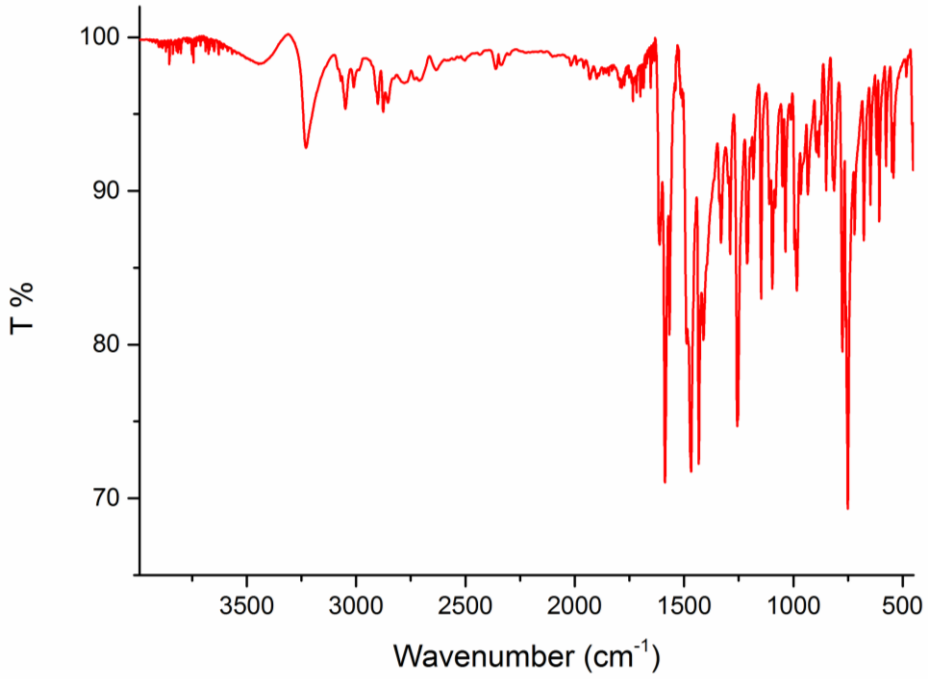

Figure S10. FT-IR spectrum (KBr pellet) of 2-({[di(2-pyridyl)methyl]amino}methyl)phenol (**HL²**).

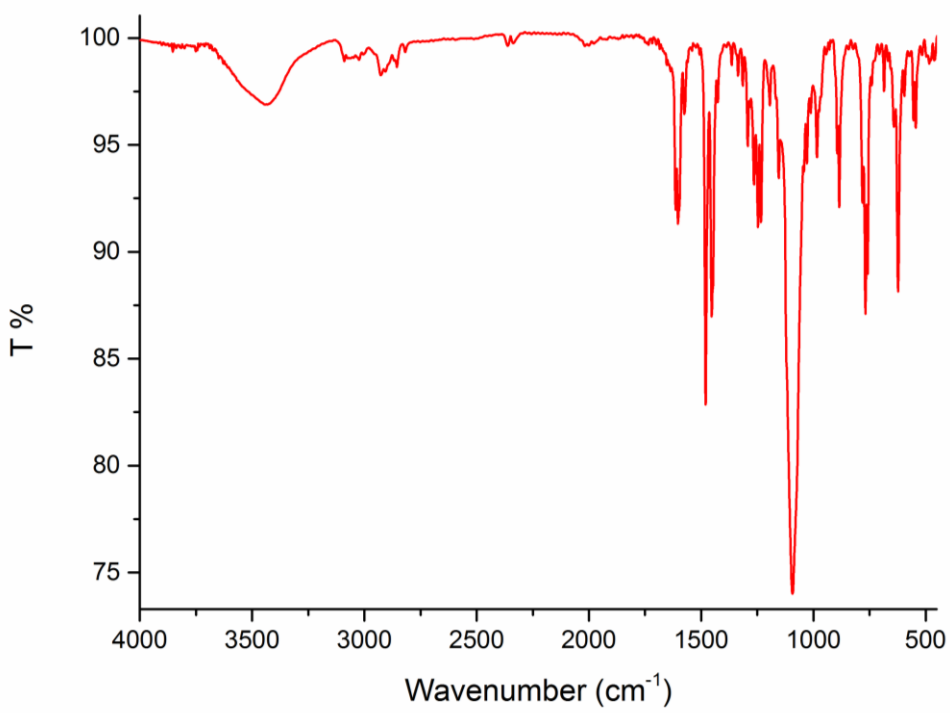

Figure S11. FT-IR spectrum (KBr pellet) of the complex $[\mathbf{Cu_2L^1_2}](ClO_4)_2$.

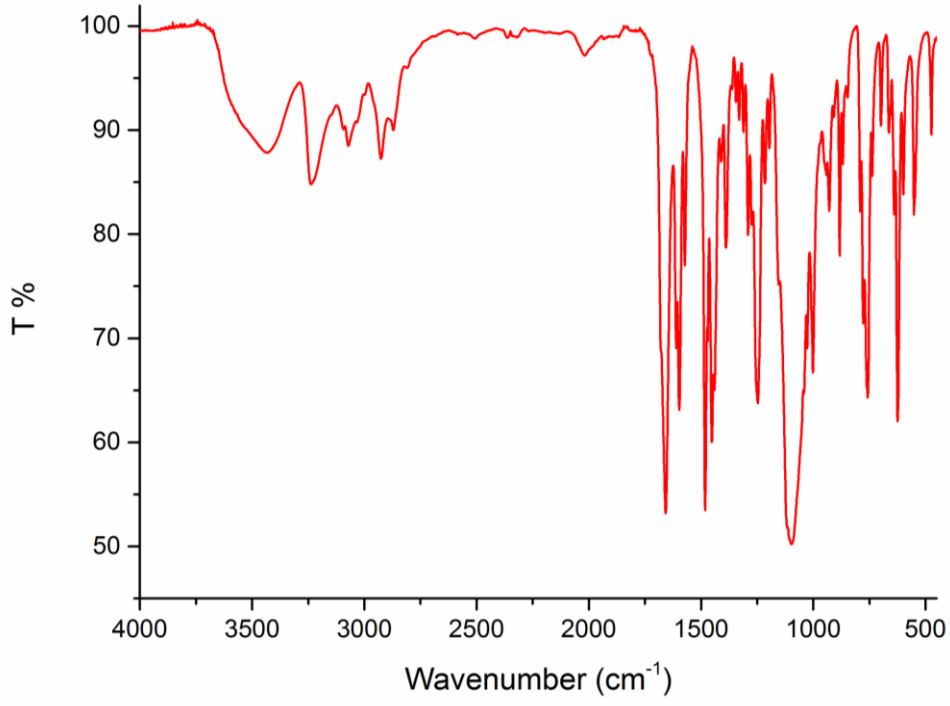

Figure S12. FT-IR spectrum (KBr pellet) of the complex $[\mathbf{Cu_2L^2_2}](ClO_4)_2$.

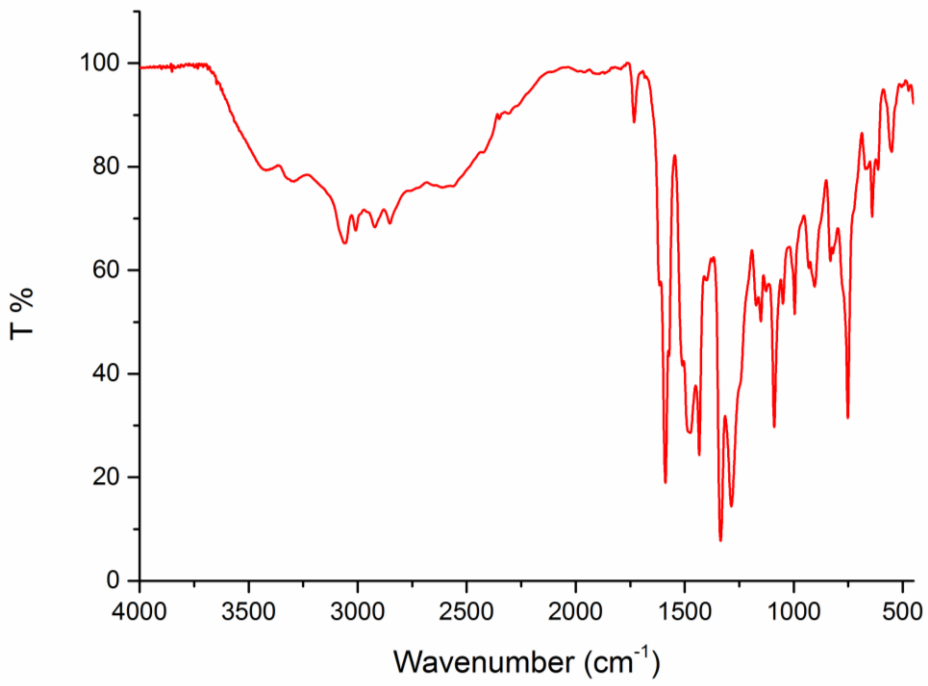

Figure S13. FT-IR spectrum (KBr pellet) of 2-({[di(2-pyridyl)methyl]amino}methyl)-4-nitrophenol (**HL³**).

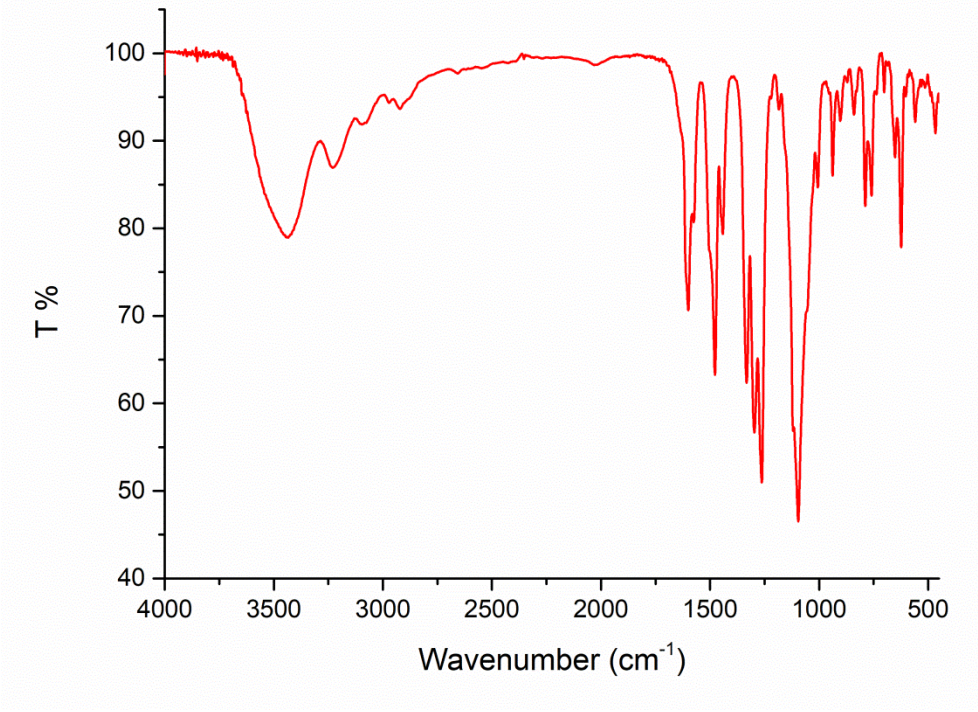

Figure S14. FT-IR spectrum (KBr pellet) of the complex $\mathbf{Cu_2L^3_2}(ClO_4)_2$.

6. Cyclic Voltammograms

CV experiments were performed using a three-electrode setup system in a small volume cell. Glassy carbon electrode (3 mm diameter, geometric surface area = 7 mm^2) from BAS and a Pt wire were used respectively as working and auxiliary electrode. Potentials were referred to an Ag/AgCl/(3 M NaCl) reference electrode; scan rate of 50 mV/s. Prior to each experiment, the electrode was polished with 1 µm alumina, rinsed with deionised water and wiped with a paper tissue. In a typical experiment, a 0.5-1 mM solution of the copper compound in 0.05 M phosphate buffer, pH = 7.8, with 0.1 M NaCl as support electrolyte was purged with nitrogen and then analysed. Potential were then reported vs NHE.

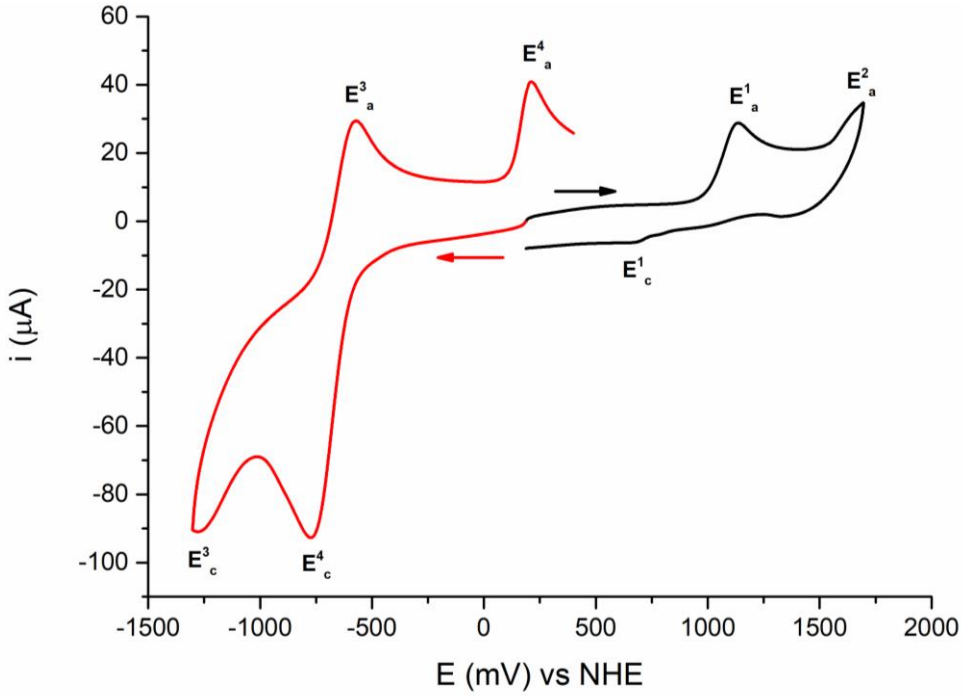

Figure S15. CV of 2-{[[di(2-pyridyl)methyl](methyl)amino]methyl}phenol (**HL^1**) (1 mM) in CH_3CN ($TBAClO_4$ 0.1 M); E^3_c = -1285 mV, E^4_c = -772 mV, E^3_a = -599 mV, E^4_a = 197 mV, E^1_c = 654 mV, E^1_a = 1133 mV and E^2_a =1690 mV.[S8]

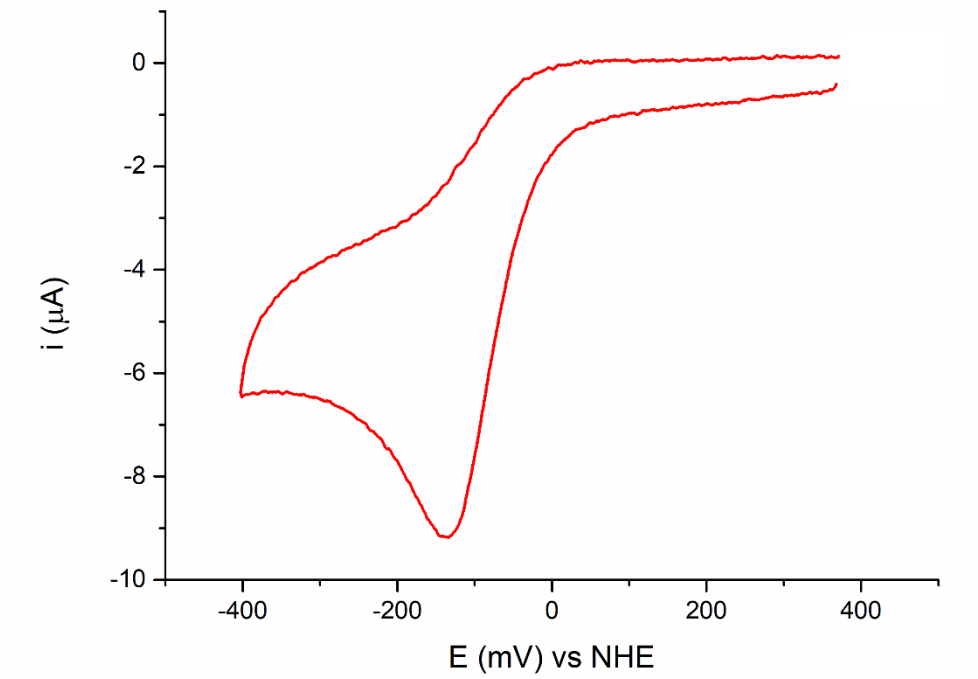

Figure S16. CV of $Cu_2L^1_2$ (0.5 mM) in CH_3CN ($TBAClO_4$ 0.1 M), E_c = -136 mV.

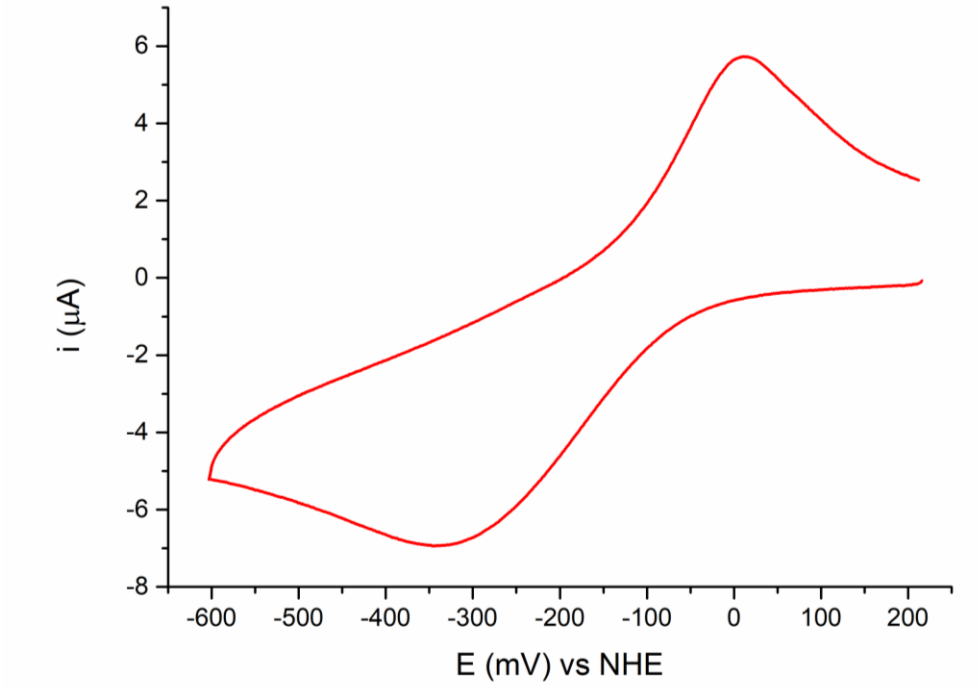

Figure S17. CV of $Cu_2L^1_2$ (0.5mM) in phosphate buffer 50 mM (pH = 7.8, $TEABF_4$ 0.1 M), $E_{1/2}$ = -161 mV, ΔE =350 mV.

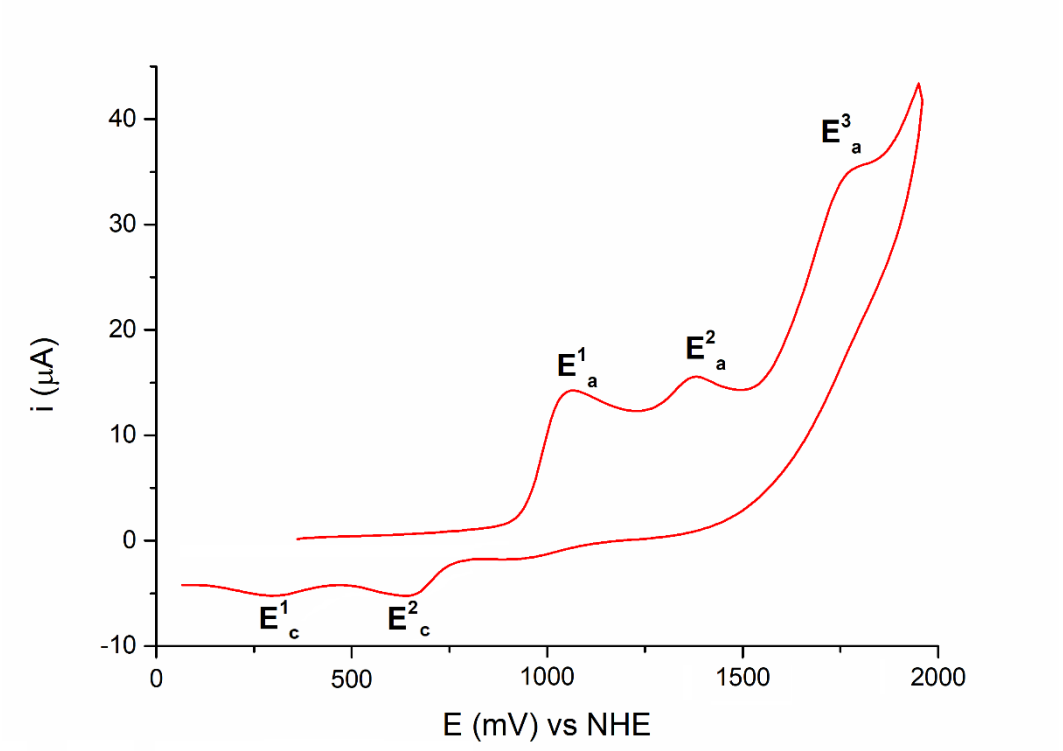

Figure S18. Cyclic voltammetry of $Cu_2L^1_2$ (1mM) in acetonitrile ($TBAClO_4$ 0.1M), E^1_c = 296 mV, E^2_c = 635 mV, E^1_a = 1060 mV, mV, E^2_a = 1380 mV, and E^3_a = 1780 mV (vs NHE).

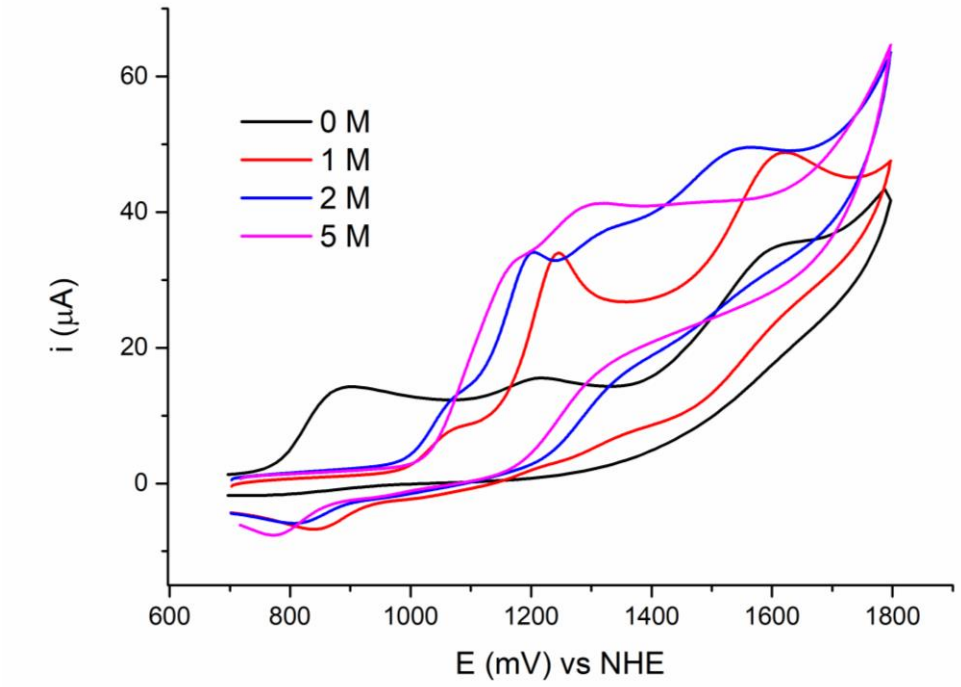

Figure S19. CV of the oxidation of $Cu_2L^1_2$ (1 mM) in CH_3CN ($TBAClO_4$ 0.1 M) with increasing aliquots of water.

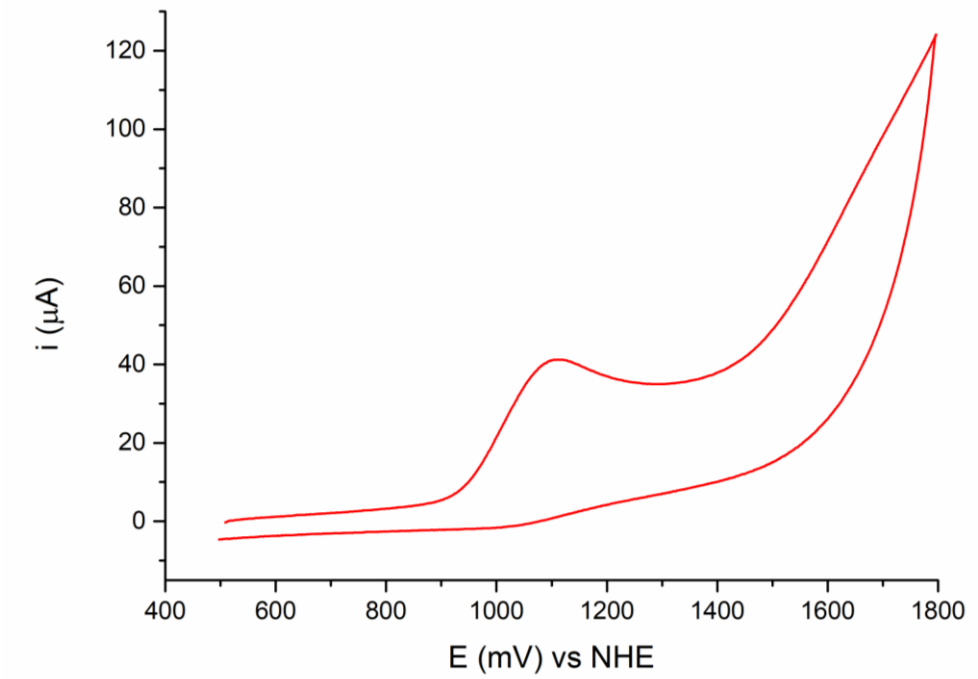

Figure S20. CV of the oxidation of $Cu_2L^1_2$ (1 mM) in phosphate buffer 50 mM (pH 7.8, $TEABF_4$ 0.1 M), E_a = 1.11 V.

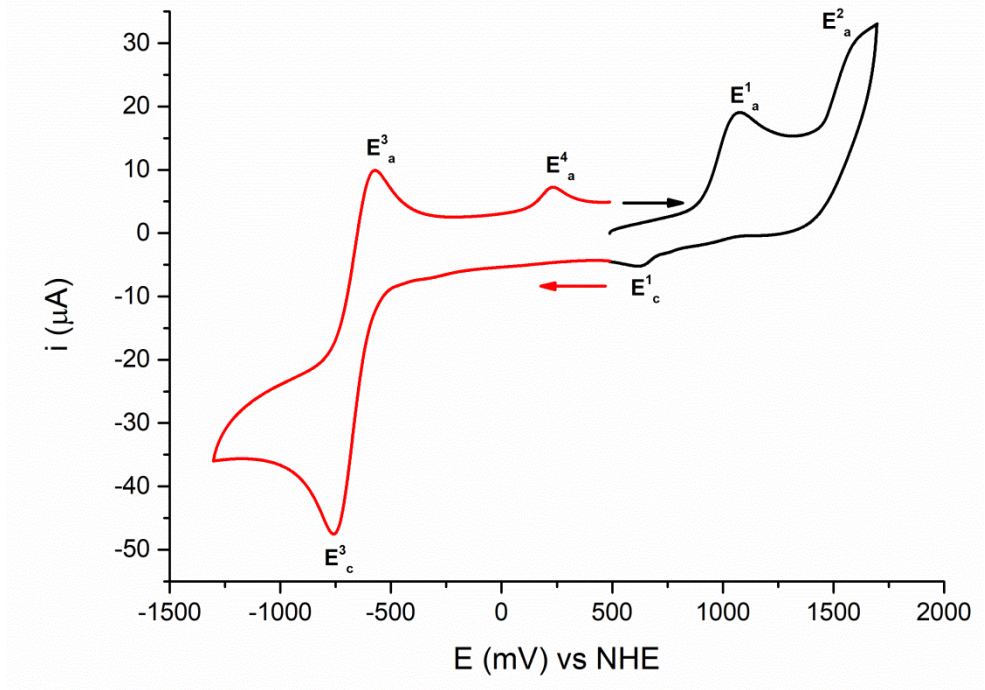

Figure S21. CV of 2-({[di(2-pyridyl)methyl]amino}methyl)phenol (**HL^2**) (1 mM) in CH_3CN ($TBAClO_4$ 0.1 M); E^3_c = -758 mV, E^3_a = -573 mV, E^4_a = 231 mV, mV, E^1_c = 621 mV, E^1_a = 1079 mV and E^2_a = 1635 mV.

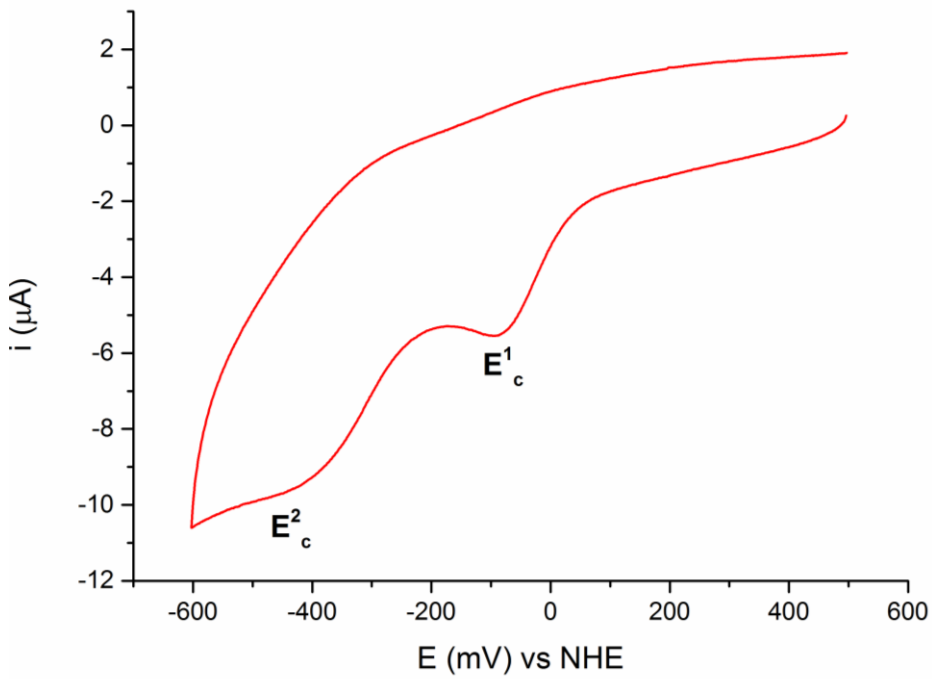

Figure S22. CV of $Cu_2L^2_2$ (0.5 mM) in CH_3CN ($TEABF_4$ 0.1 M), E^1_c = -96 mV and E^2_c = -465 mV.

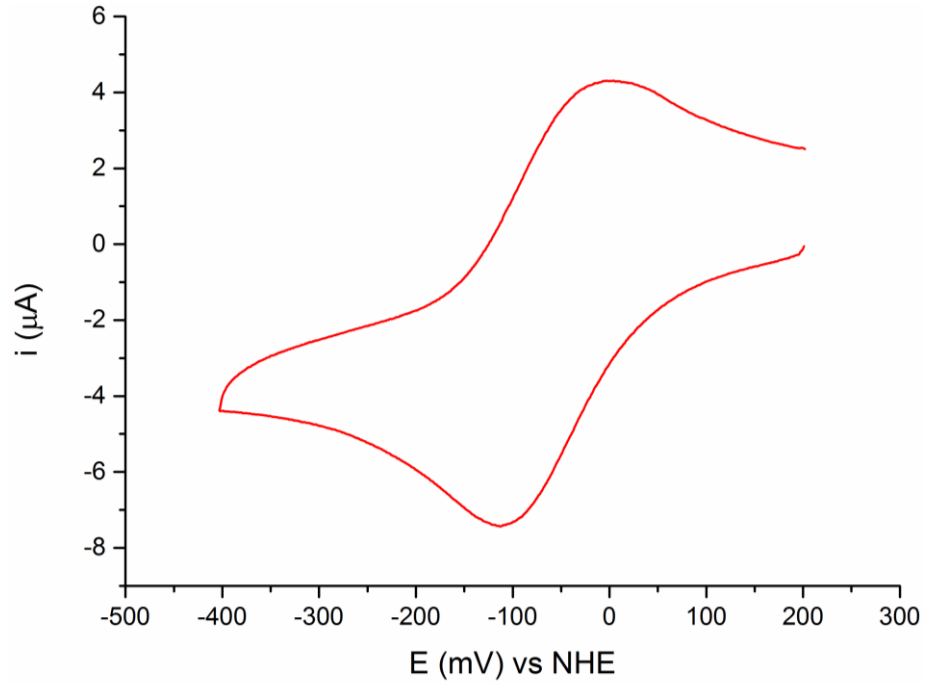

Figure S23. CV of $Cu_2L^2_2$ (0.5 mM) in phosphate buffer 50 mM (pH = 7.8, $TEABF_4$ 0.1 M), $E_{1/2}$ = -55 mV, ΔE =116 mV.

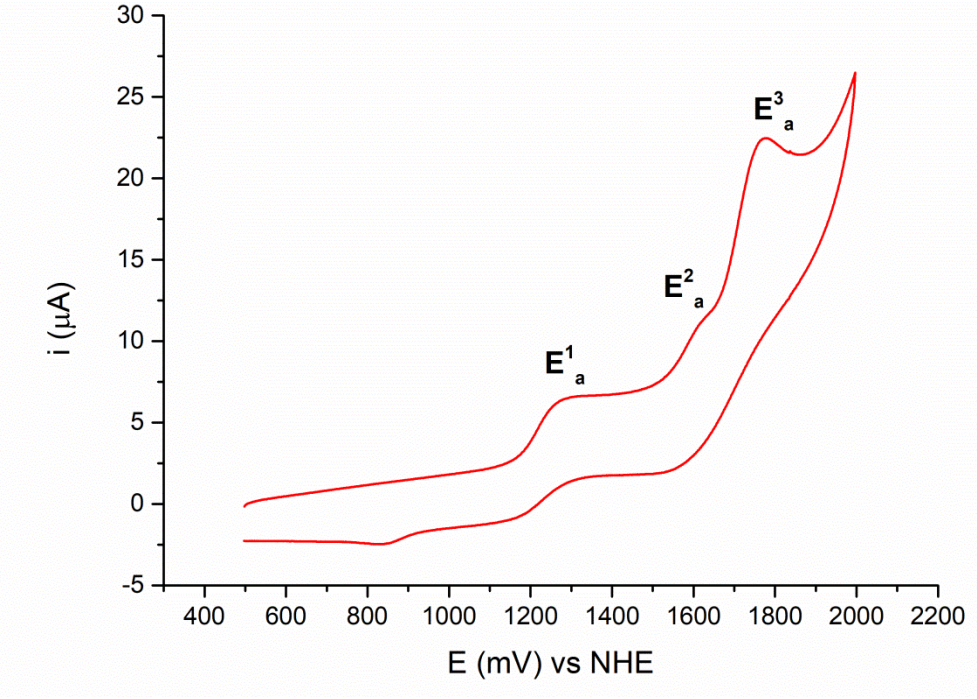

Figure S24. Cyclic voltammetry of $Cu_2L^2_2$ (1 mM) in acetonitrile ($TEABF_4$ 0.1M), with E^1_a = 1281 mV and E^2_a = 1620 mV. E^3_a = 1775 mV.

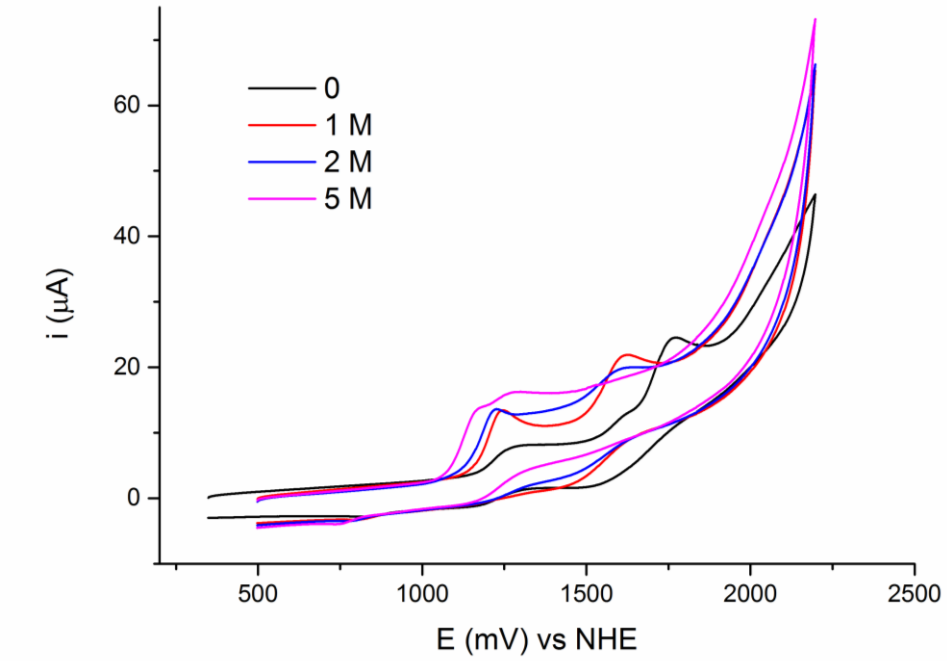

Figure S25. CV of the oxidation of $Cu_2L^2_2$ (1 mM) in CH_3CN ($TEABF_4$ 0.1 M) with increasing aliquots of water.

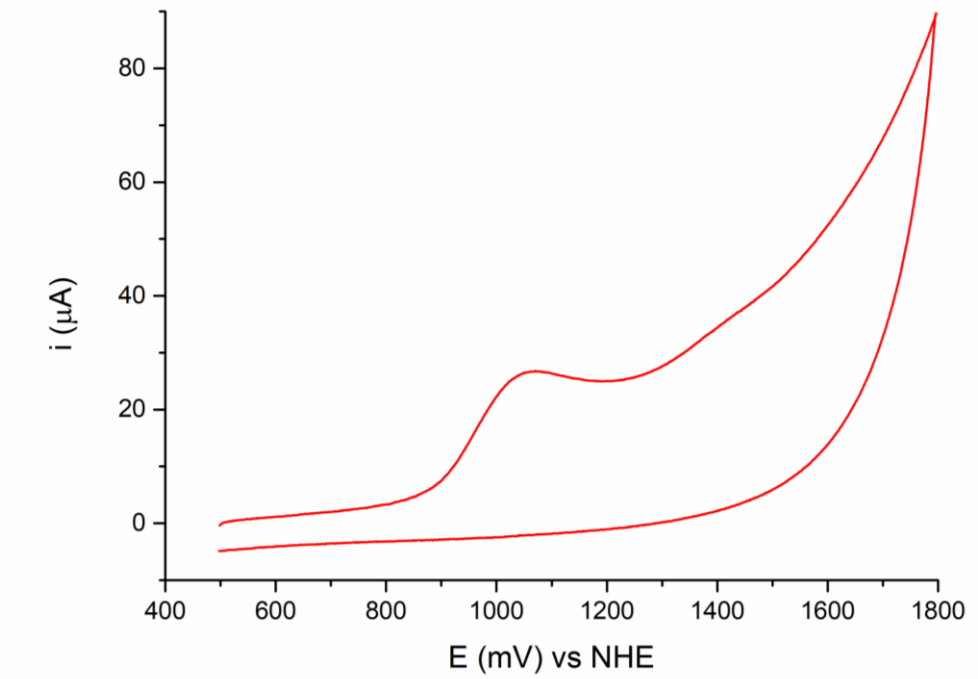

Figure S26. CV of the oxidation of $Cu_2L^2_2$ (1 mM) in phosphate buffer 50 mM (pH 7.8, $TEABF_4$ 0.1 M), E_a = 1.07 V.

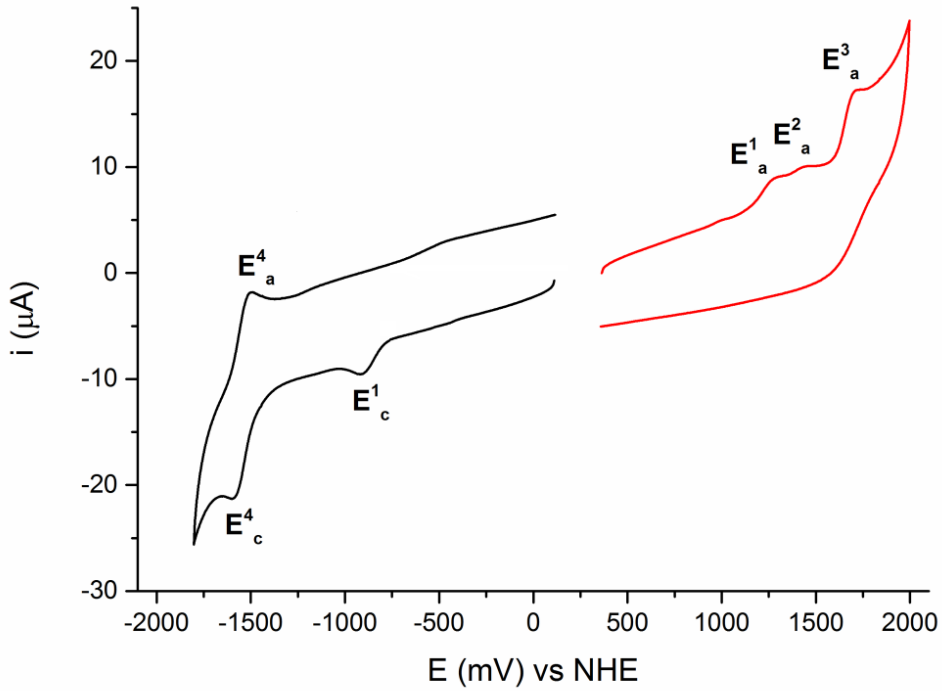

Figure S27. CV of 2-({[di(2-pyridyl)methyl]amino}methyl)-4-nitrophenol (**HL^3**) (1 mM) in CH_3CN ($TEABF_4$ 0.1 M); E^4_c = -1600 mV, E^4_a = -1499 mV, E^1_c = -916 mV, E^1_a = 1299 mV, E^2_a = 1452 mV and E^3_a = 1727 mV.

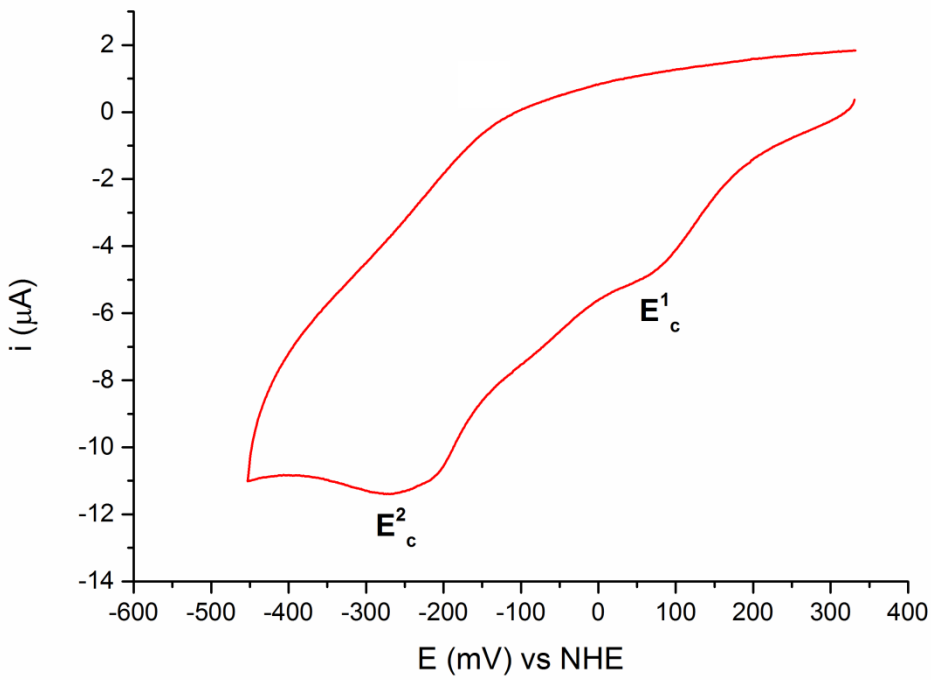

Figure S28. CV of $Cu_2L^3_2$ (0.5 mM) in CH_3CN ($TEABF_4$ 0.1 M), E^1_c = 62 mV and E^2_c = -273 mV.

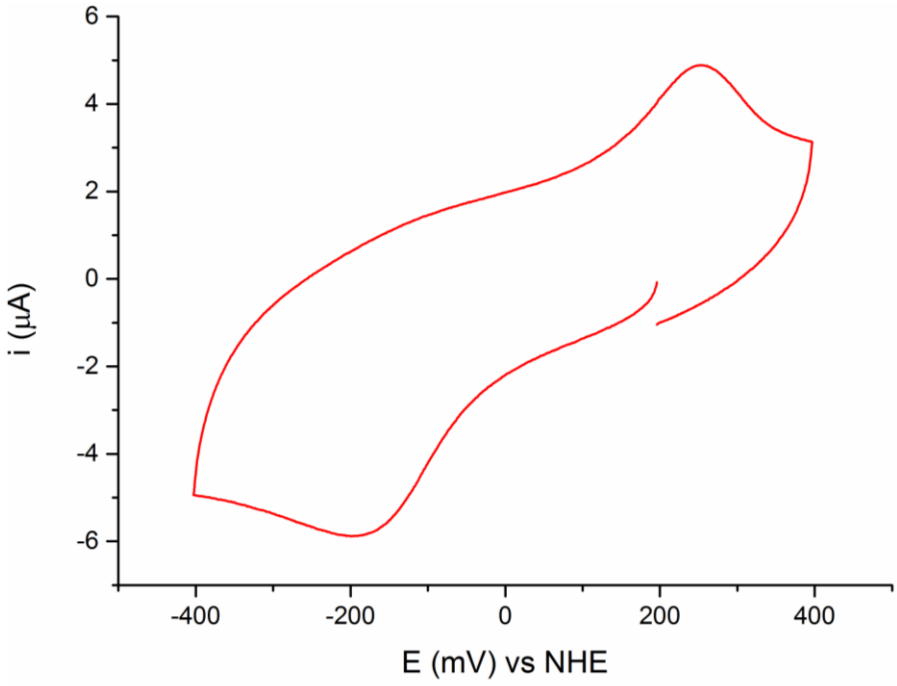

Figure S29. CV of $Cu_2L^3_2$ (0.5 mM) in phosphate buffer 50 mM (pH = 7.8, $TEABF_4$ 0.1 M), $E_{1/2}$ = 60 mV, ΔE =450 mV.

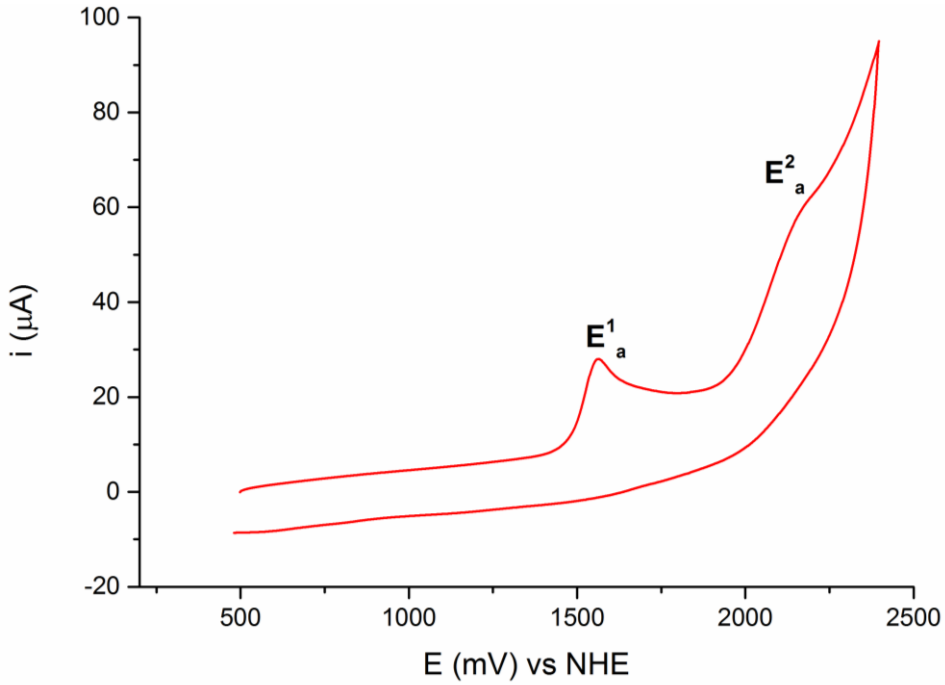

Figure S30. Cyclic voltammetry of $\mathbf{Cu_2L^3_2}$ (1 mM) in acetonitrile ($TEABF_4$ 0.1M), with E^1_a = 1.56 V and E^2_a = 2.19 V (vs NHE).

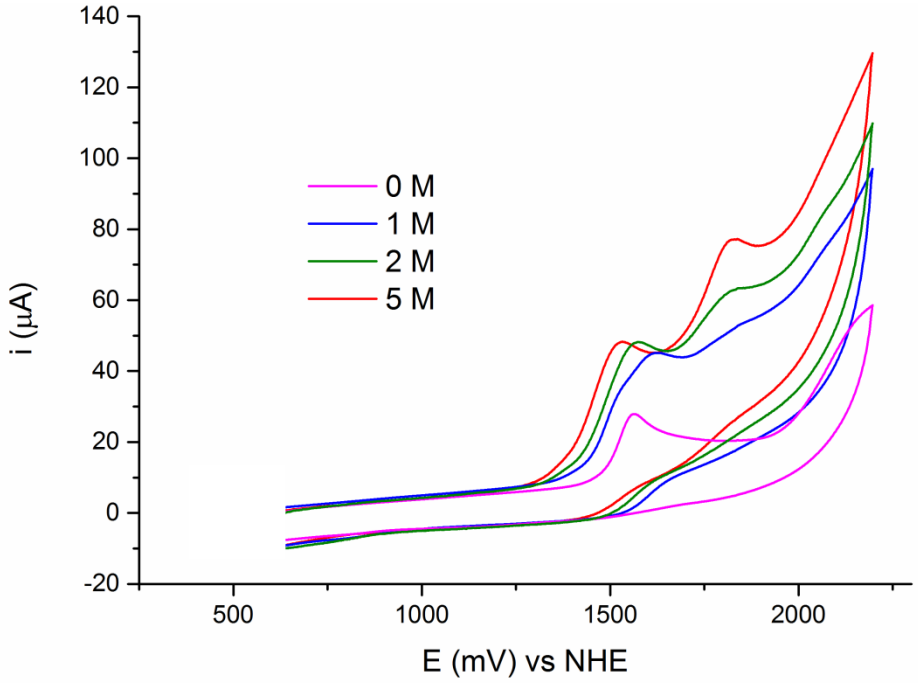

Figure S31. CV of the oxidation of $\mathbf{Cu_2L^3_2}$ (1 mM) in CH_3CN ($TEABF_4$ 0.1 M) with increasing aliquots of water.

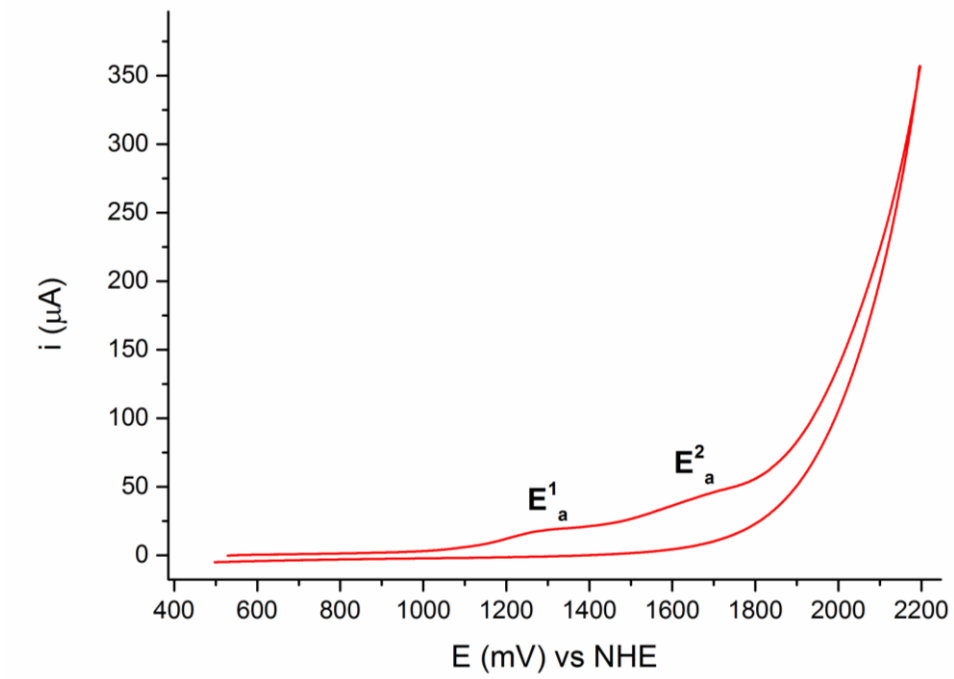

Figure S32. CV of the oxidation of $Cu_2L^3_2$ (1 mM) in phosphate buffer 50 mM (pH 7.8, $TEABF_4$ 0.1 M), E^1_a = 1.31 V and E^2_a = 1.71 V (vs NHE).

7. ESI-MS

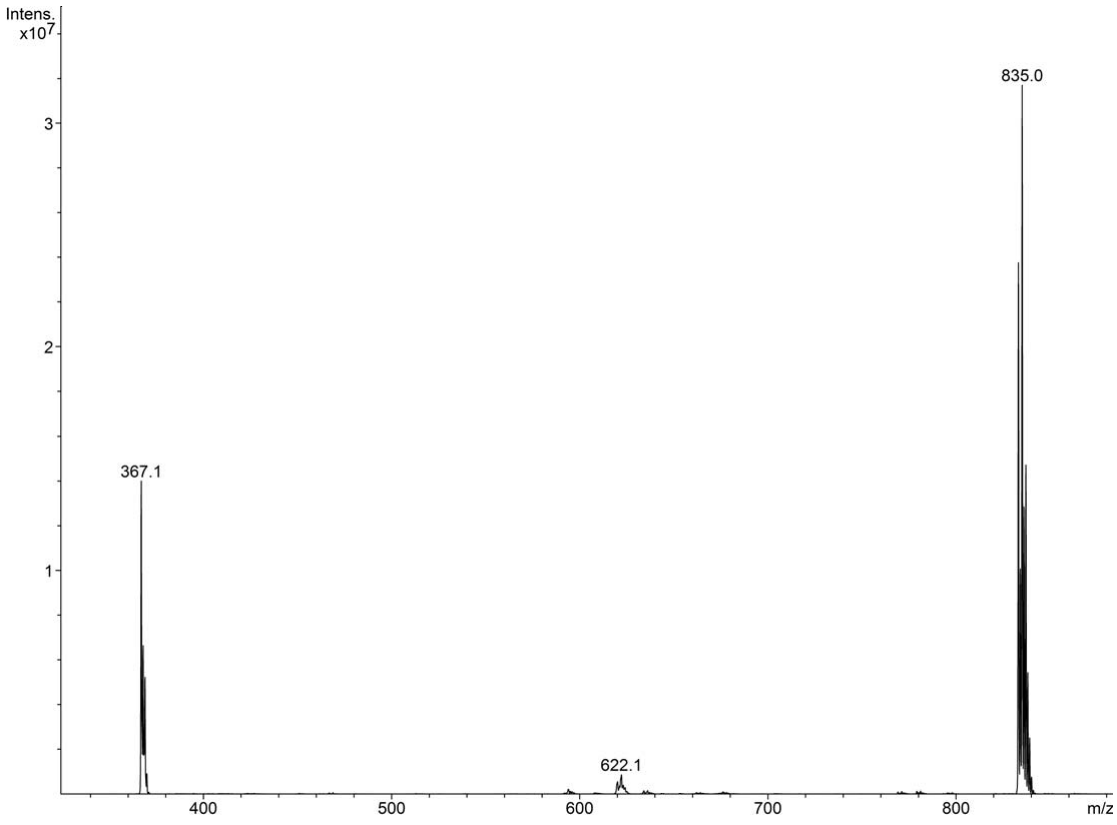

Figure S33. ESI-MS spectrum of $Cu_2L^1_2$ in acetonitrile, where 833.0 m/z correspond to the molecular ion $[Cu_2L^1_2+ClO_4]^+$ and 367.1 m/z to the fragment $[CuL^1]^+$.

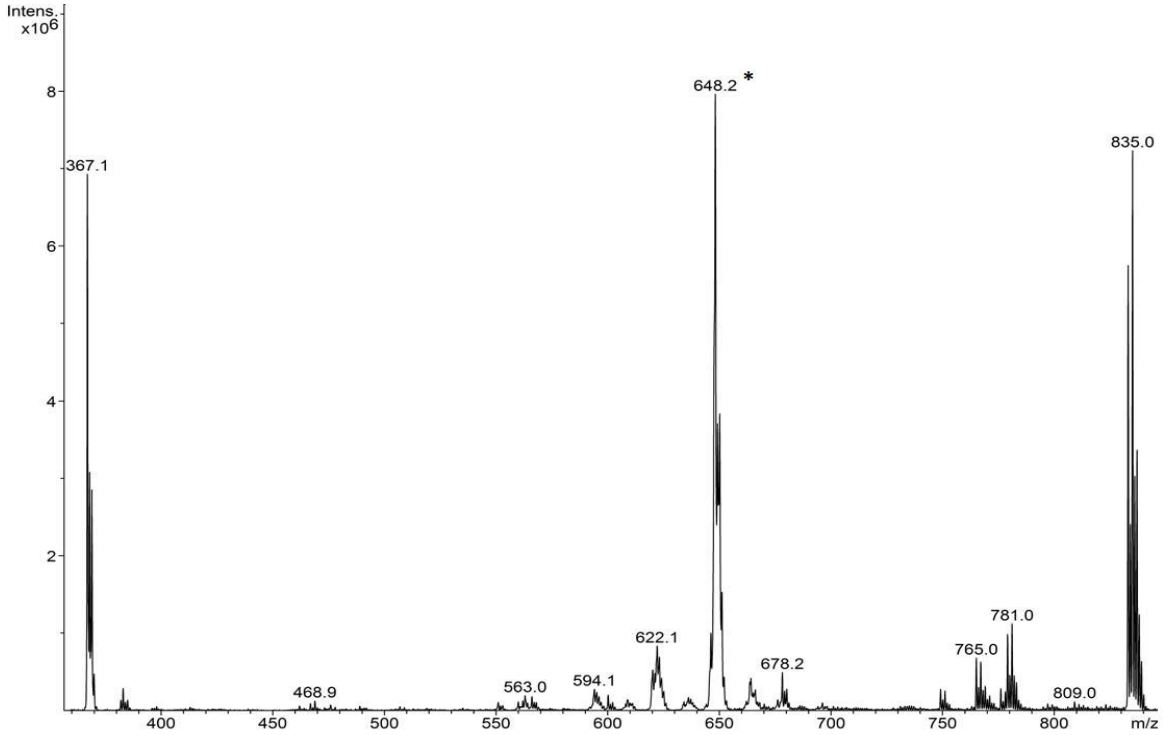

Figure S34. ESI-MS spectrum of $\mathbf{Cu_2L^1_2}$ in acetonitrile 90 min after the addition of H_2O_2 30 mM, where 833.0 m/z correspond to the molecular ion $[\mathbf{Cu_2L^1_2}+ClO_4]^+$ and 367.1 m/z to the fragment $[CuL^1]^+$ (* eluent impurity).

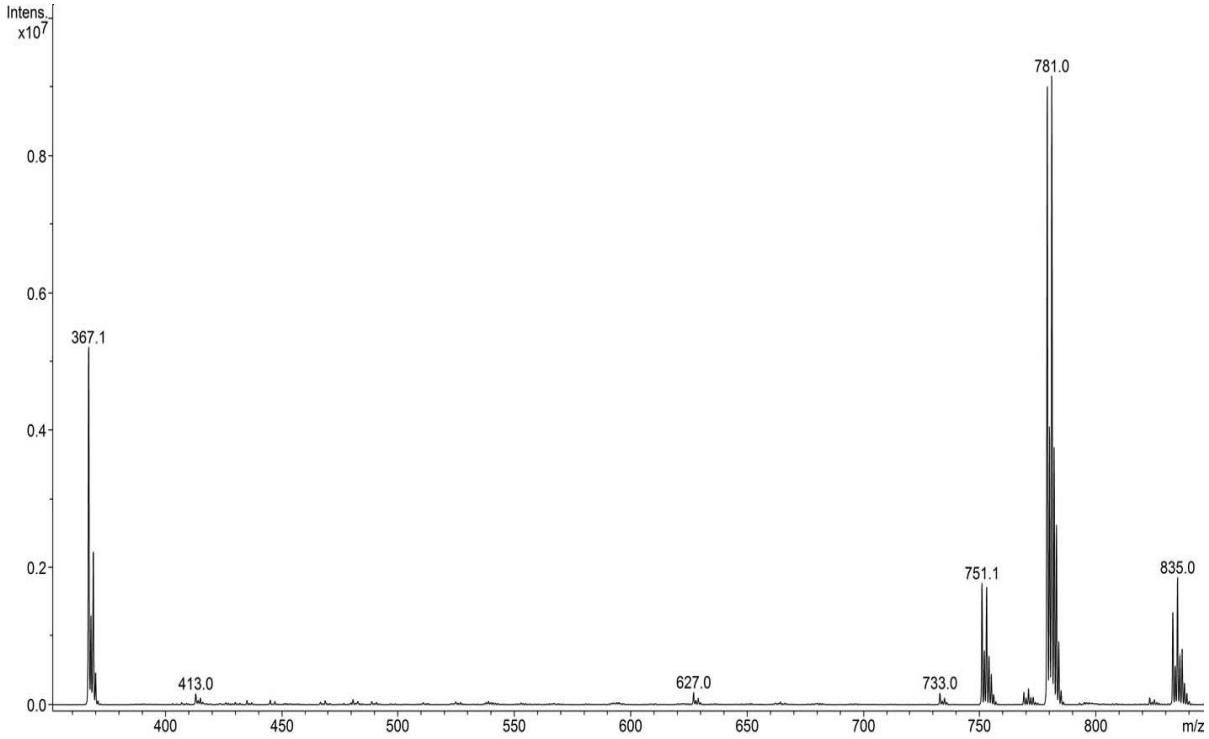

Figure S35. ESI-MS spectrum of $\mathbf{Cu_2L^1_2}$ in water, where 779.0 correspond to the molecular ion $[\mathbf{Cu_2L^1_2}+HCO_2]^+$, 751.1 to $[\mathbf{Cu_2L^1_2}+OH]^+$ and 833.0 m/z $[\mathbf{Cu_2L^1_2}+ClO_4]^+$ and 367.1 m/z to the fragment $[CuL^1]^+$.

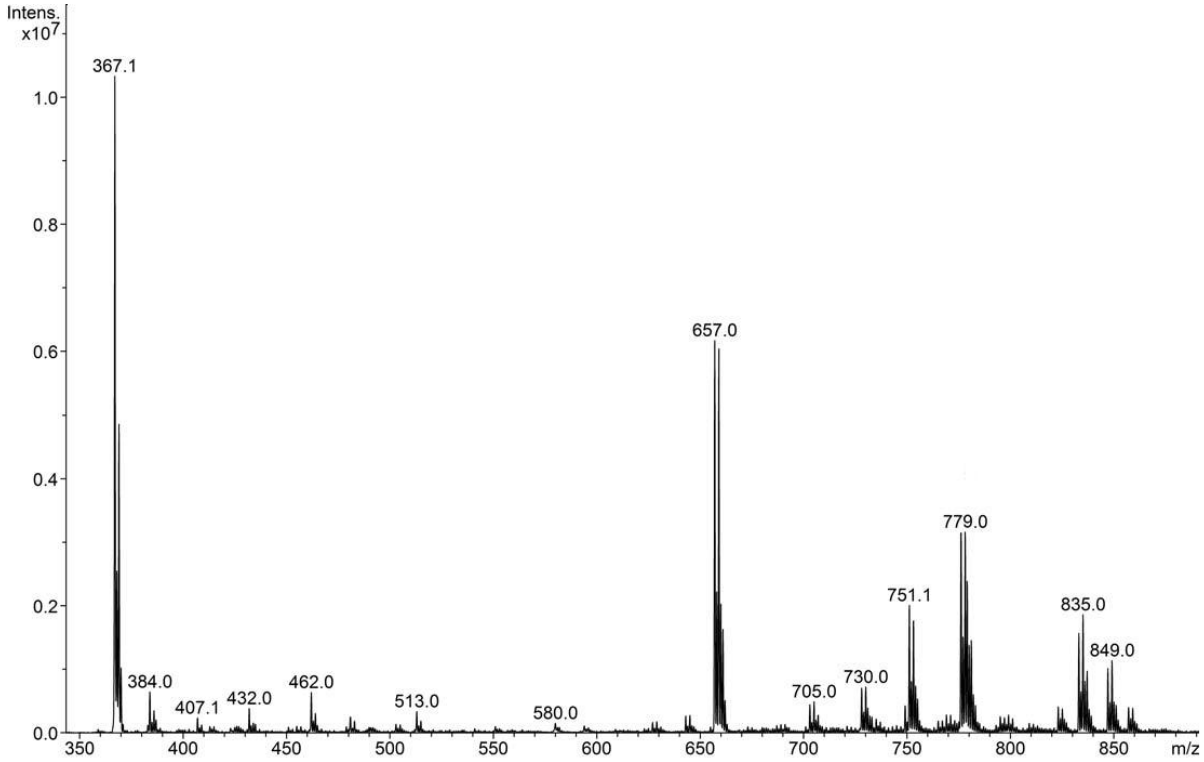

Figure S36. ESI-MS spectrum of $\mathbf{Cu_2L^1_2}$ in borate buffer 50 mM, 25 min after the addition of H_2O_2 30 mM, where 657.0 m/z correspond to the dinuclear copper specie $[\mathbf{Cu_2L^{Ox}L^{Cl}}(O)]^+$ and 384.0 to the inactive mononuclear copper(III) specie $[\mathbf{CuL^1}OH]^+$.

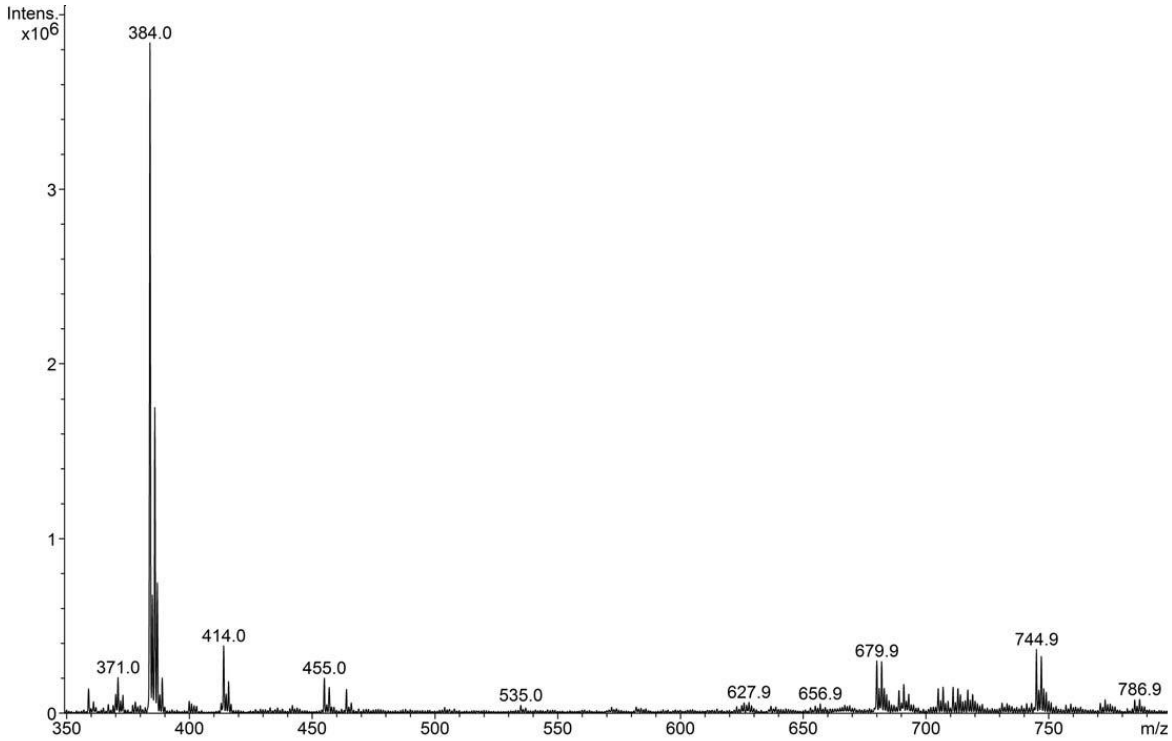

Figure S37. ESI-MS spectrum of $\mathbf{Cu_2L^1_2}$ in borate buffer 50 mM, 240 min after the addition of H_2O_2 30 mM, where 384.0 correspond to the inactive mononuclear copper(III) specie $[\mathbf{CuL^1}(OH)]^+$.

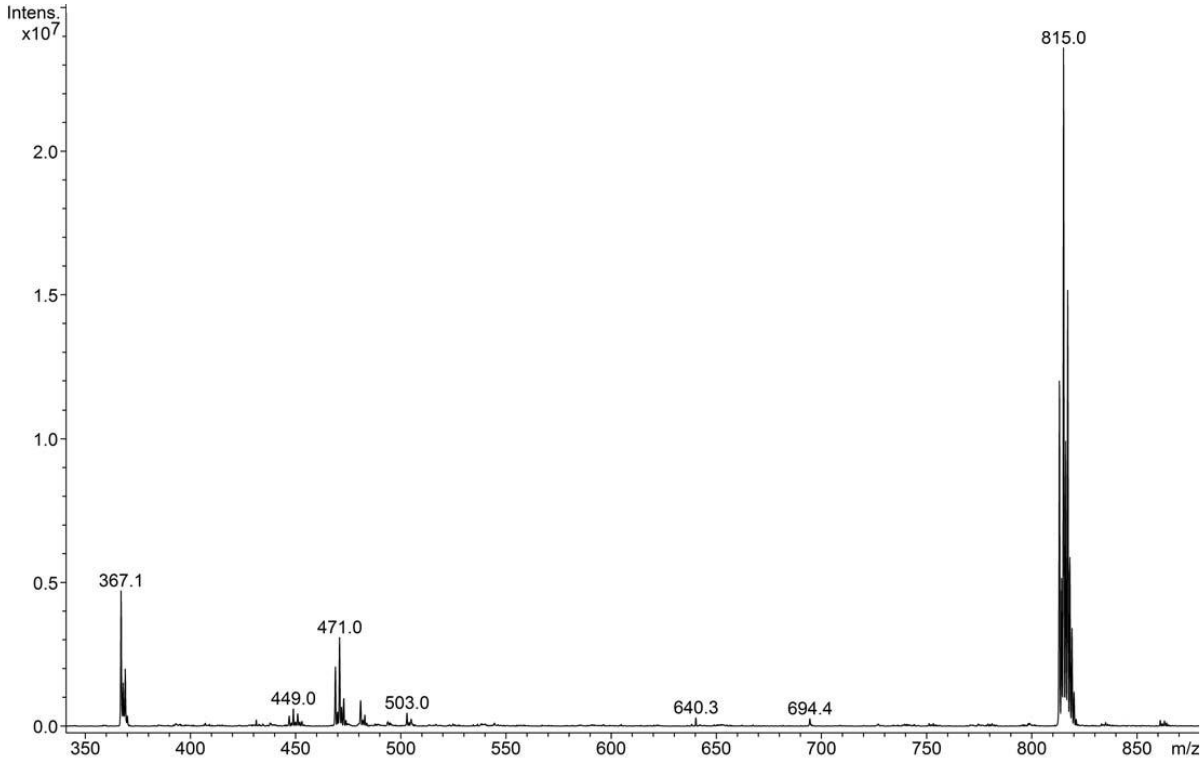

Figure S38. ESI-MS spectrum of $\mathbf{Cu_2L^1_2}$ in borate buffer 50 mM with NaBr 50 mM, where 813.0 m/z correspond to the molecular ion $[\mathbf{Cu_2L^1_2}+Br]^+$ and 367.1 m/z to the fragment $[CuL^1]^+$.

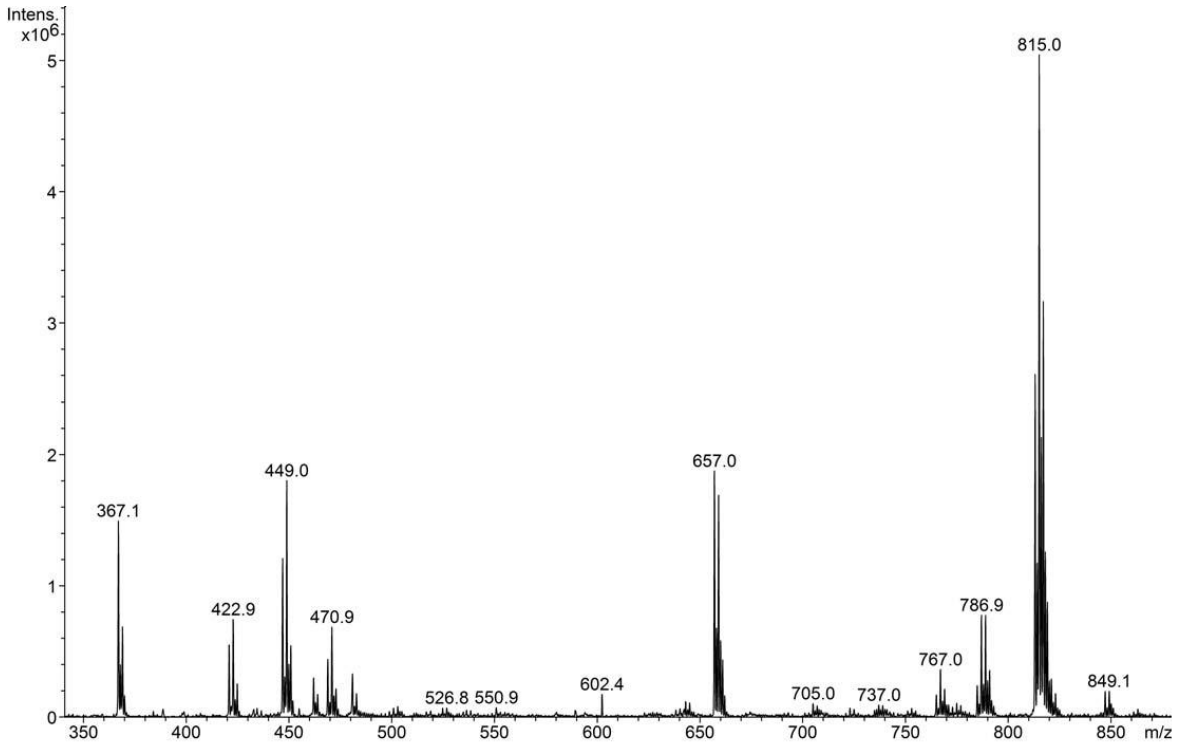

Figure S39. ESI-MS spectrum of $\mathbf{Cu_2L^1_2}$ in borate buffer 50 mM with NaBr 50 mM, 80 min after the addition of H_2O_2 30 mM where 657.0 and 784.9 m/z correspond respectively to the molecular ions $[\mathbf{Cu_2L^1L^{Cl}}+2Br]^+$ and $[\mathbf{Cu_2L^{Ox}L^{Cl}}(O)]^+$ and 420.9 m/z correspond to the inactive specie $[\mathbf{CuL^{Cl}}(H_2O)_2+Br+HCO_2H]^+$.

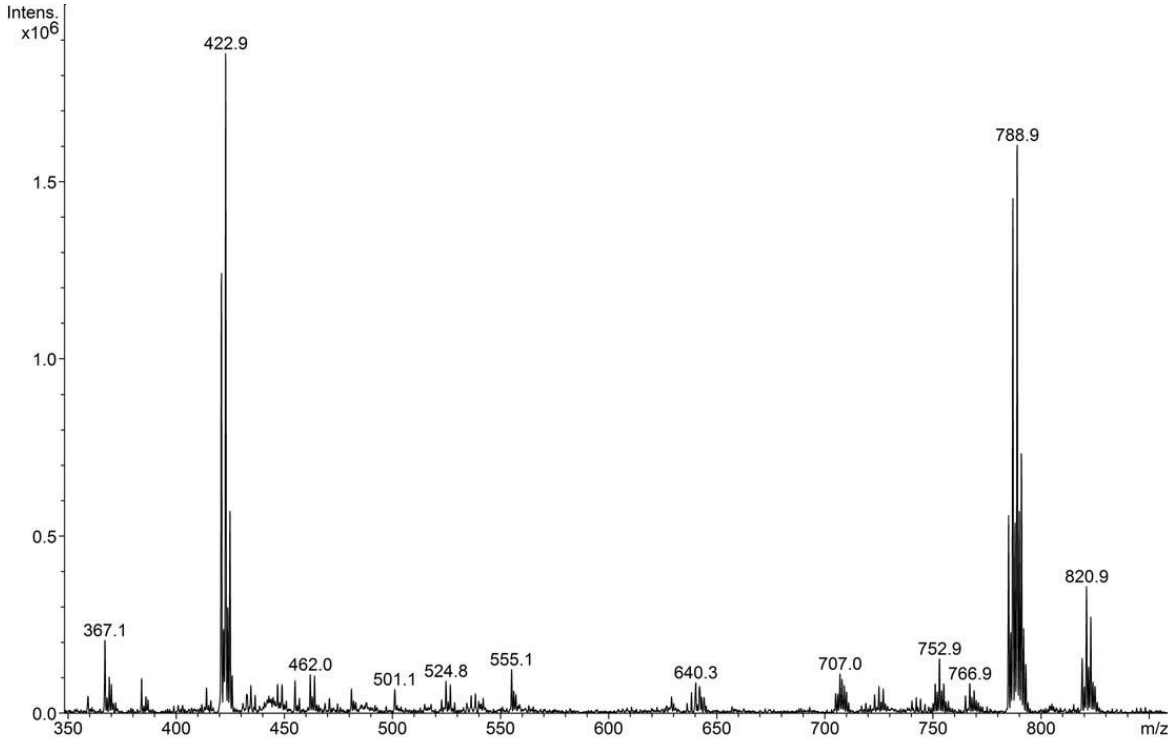

Figure S40. ESI-MS spectrum of $\mathbf{Cu_2L^1_2}$ in borate buffer 50 mM with NaBr 50 mM, 240 min after the addition of H_2O_2 30 mM where 784.9 m/z correspond to the molecular ion $[\mathbf{Cu_2L^1L^{Cl}}+2Br]^+$ and 420.9 m/z to the inactive specie $[\mathbf{CuL^{Cl}}(H_2O)_2+Br+HCO_2H]^+$.

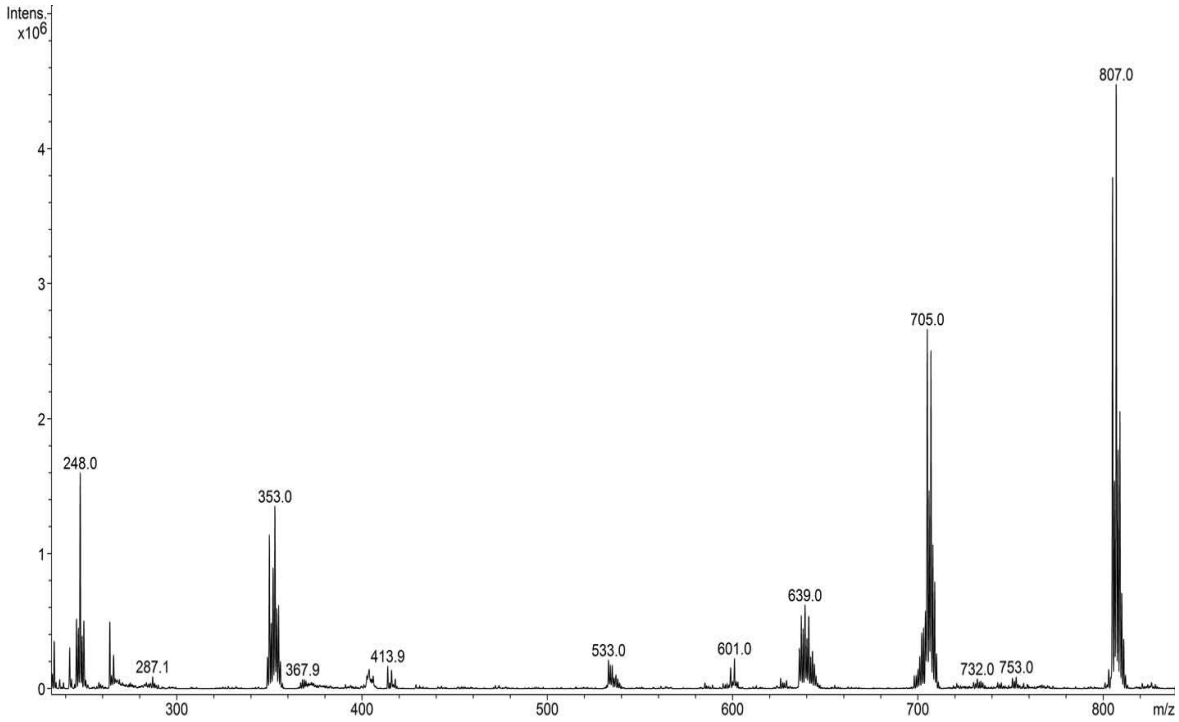

Figure S41. ESI-MS spectrum of $\mathbf{Cu_2L^2_2}$ in acetonitrile, where 805.0 m/z correspond to the molecular ion $[\mathbf{Cu_2L^2_2}+ClO_4]^+$, 705.0 m/z to $[\mathbf{Cu_2L^2_2}-H]^+$ and 353.1 m/z to the fragment $[CuL^2]^+$.

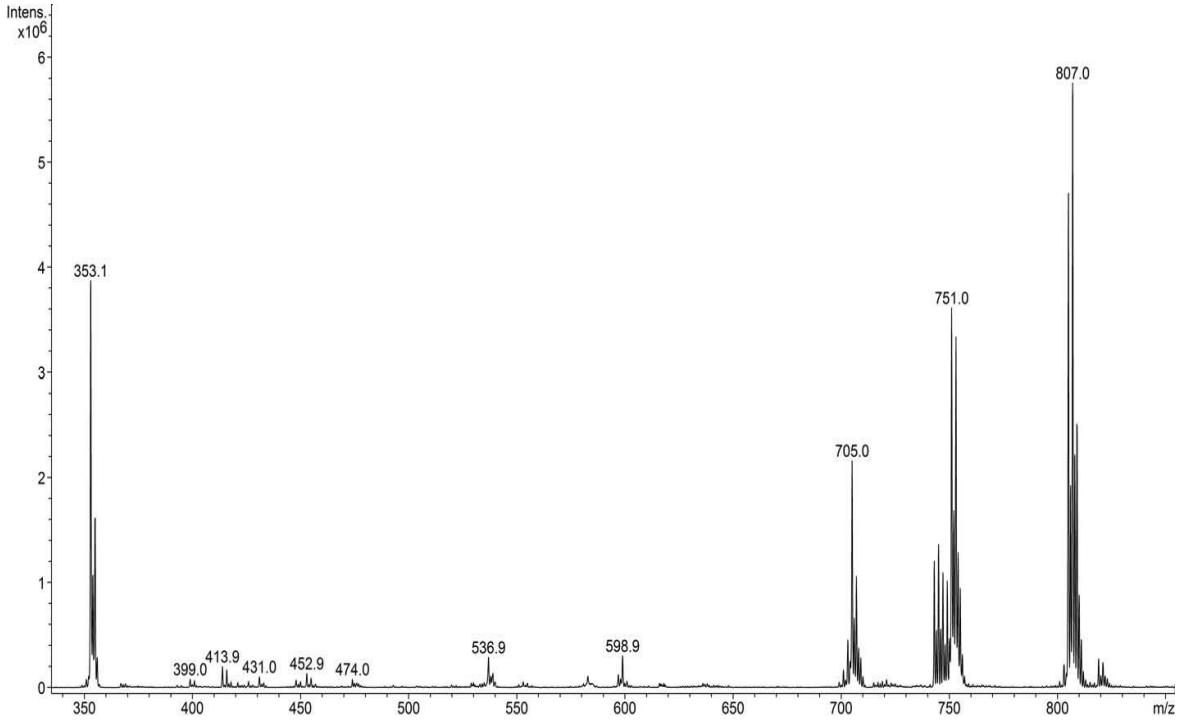

Figure S42. ESI-MS spectrum of $\mathbf{Cu_2L^2_2}$ in water, where 805.0 m/z correspond to the molecular ion $[\mathbf{Cu_2L^2_2}+ClO_4]^+$, 751.0 m/z to $[\mathbf{Cu_2L^2_2}+HCO_2]^+$ and 353.1 m/z to the fragment $[CuL^2]^+$.

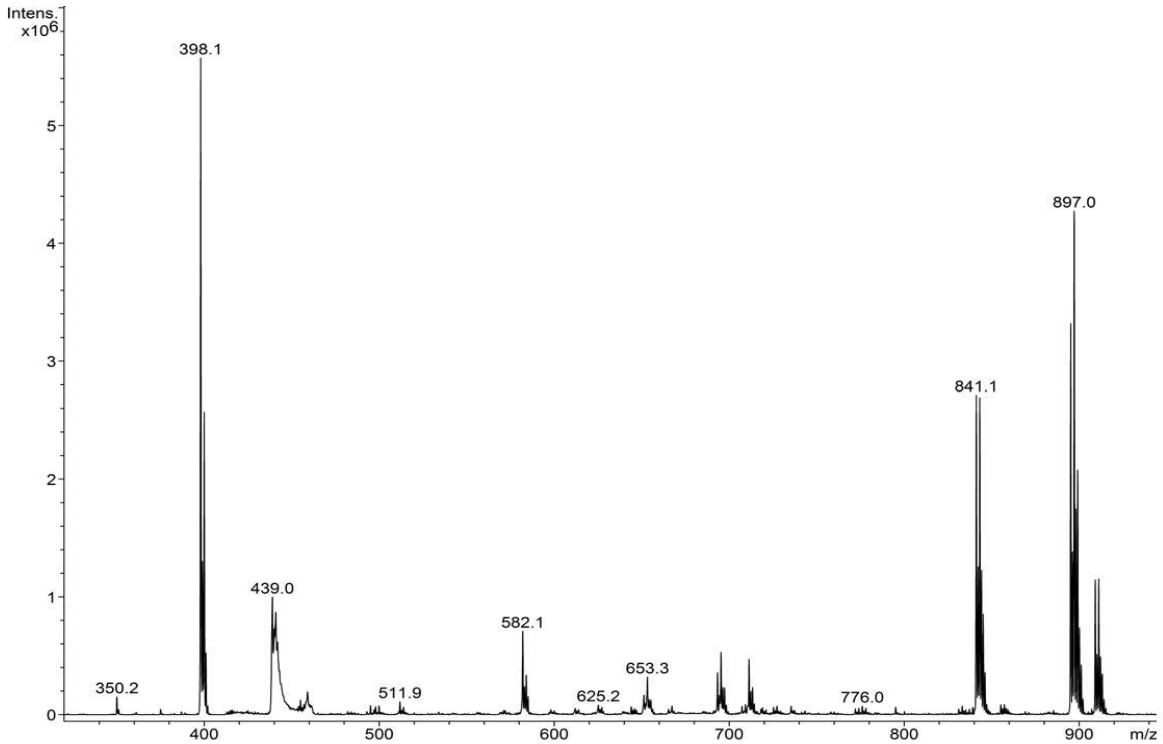

Figure S43. ESI-MS spectrum of $\mathbf{Cu_2L^3_2}$ in acetonitrile, where 895.0 m/z correspond to the molecular ion $[\mathbf{Cu_2L^3_2}+ClO_4]^+$, 841.1 m/z to $[\mathbf{Cu_2L^3_2}+HCO_2]^+$ and 398.1 m/z to the fragment $[CuL^3]^+$.

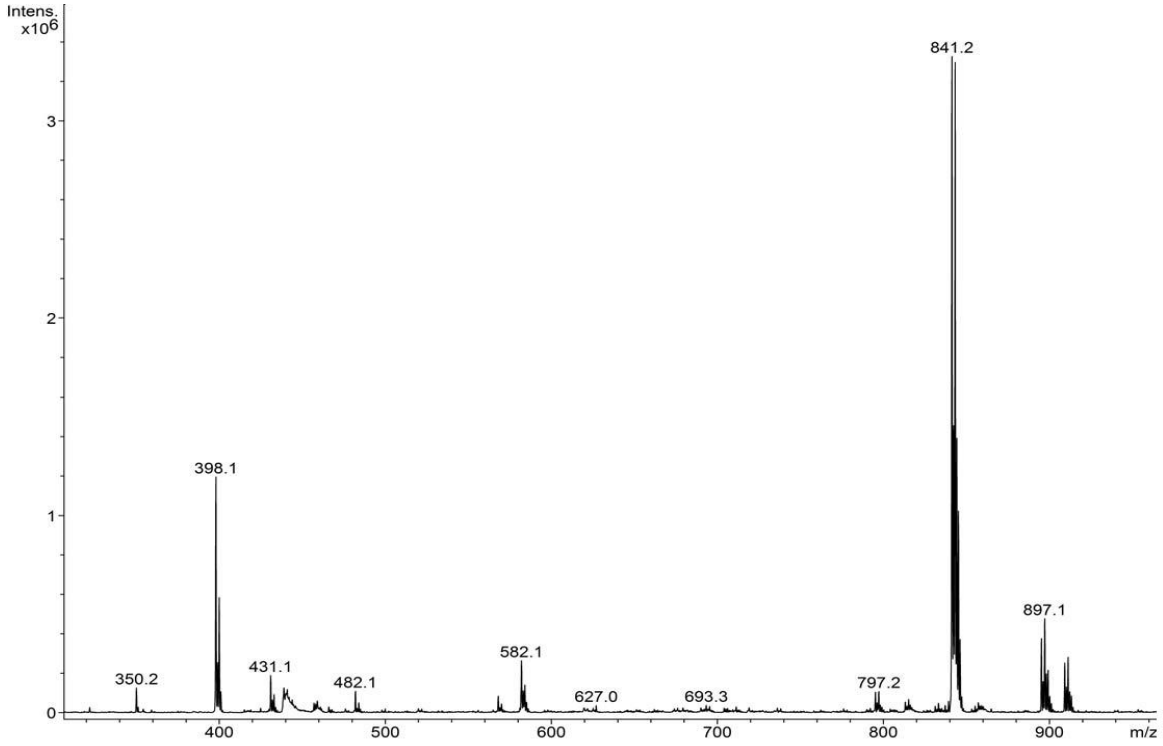

Figure S44. ESI-MS spectrum of $\mathbf{Cu_2L^3_2}$ in water, where 895.0 m/z correspond to the molecular ion $[\mathbf{Cu_2L^3_2}+ClO_4]^+$, 841.2 m/z to $[\mathbf{Cu_2L^3_2}+HCO_2]^+$ and 398.1 m/z to the fragment $[CuL^3]^+$.

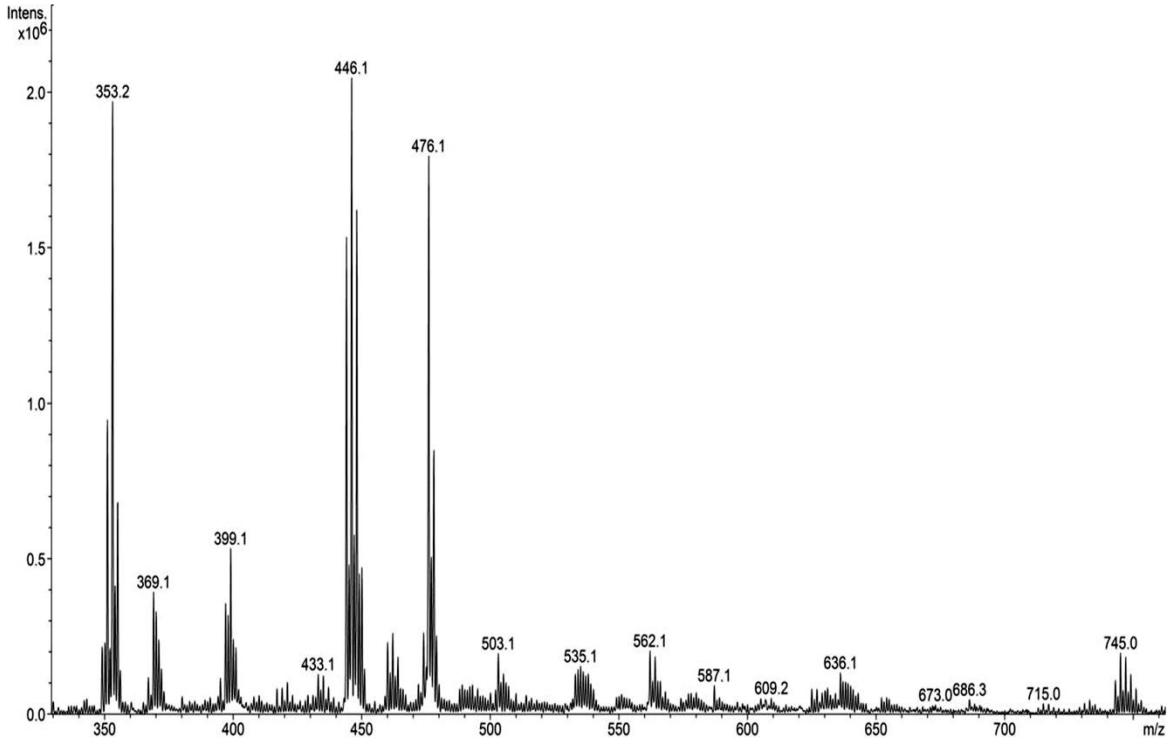

Figure S45. ESI-MS spectrum of $\mathbf{Cu_2L^2_2}$ in borate buffer 50 mM, 30 min after the addition of H_2O_2 30 mM, where 353.2 and 444.1 and correspond to the inactive mononuclear copper species. For details see Table S3 and Figure S51.

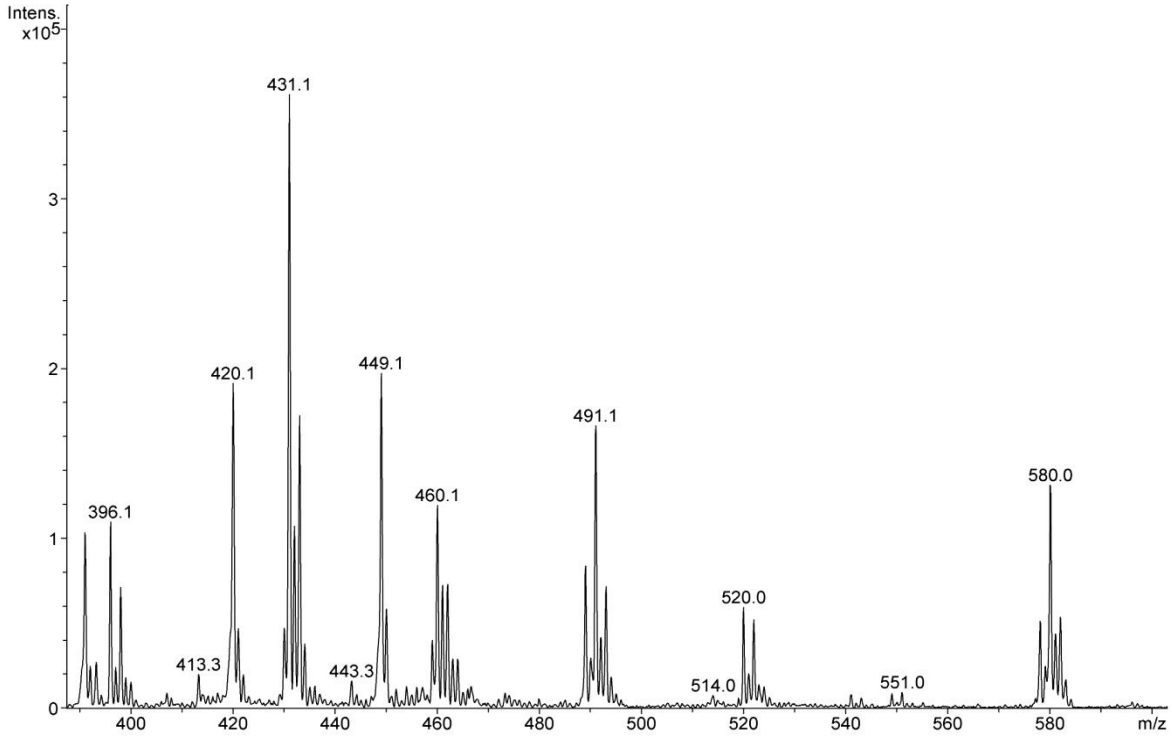

Figure S46. ESI-MS spectrum of $\mathbf{Cu_2L^3_2}$ in borate buffer 50 mM, 30 min after the addition of H_2O_2 30 mM, where 396.1 and 489.1 correspond to the inactive mononuclear copper species. For details see Table S3 and Figure S51.

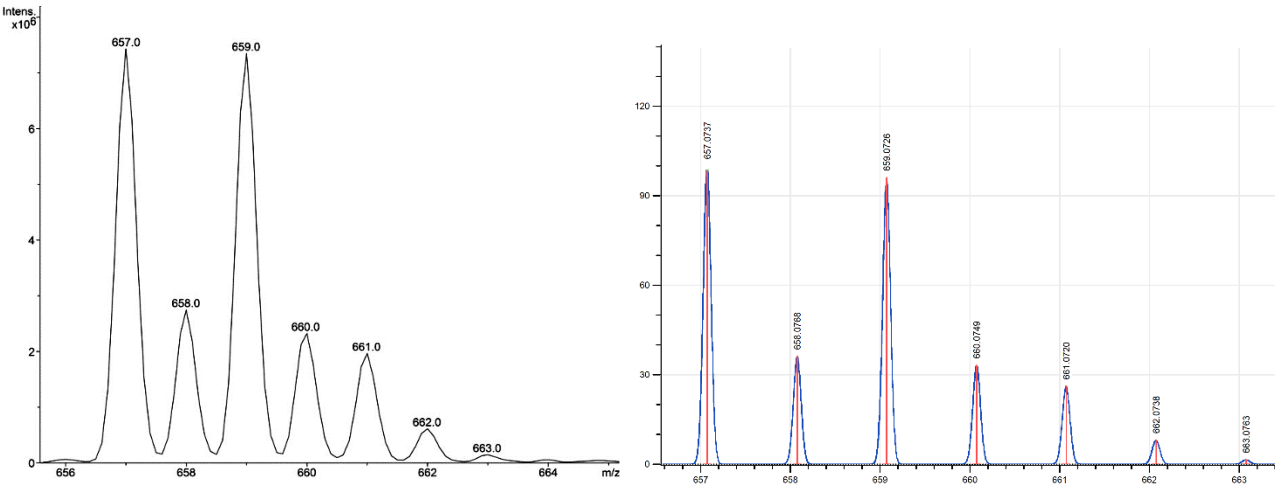

Figure S47. Comparison between the experimental (left) and calculated (right) isotopic pattern for $[\mathbf{Cu_2L^{Ox}L^{Cl}}(O)]^+$ (m/z = 657.0).

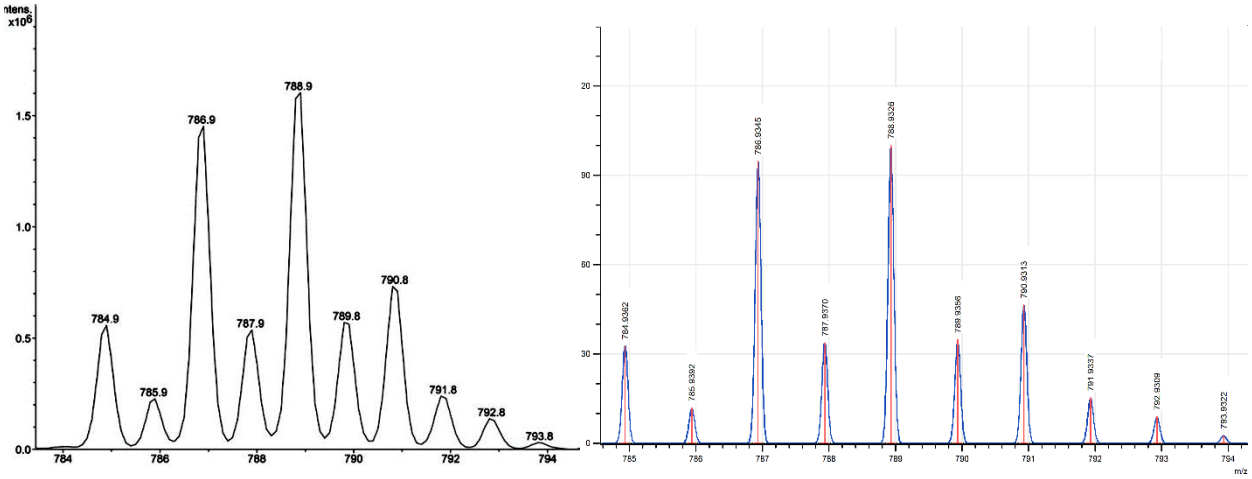

Figure S48. Comparison between the experimental (left) and calculated (right) isotopic pattern for $[Cu_2L^1L^{Cl} + 2Br]^+$ (m/z = 784.9).

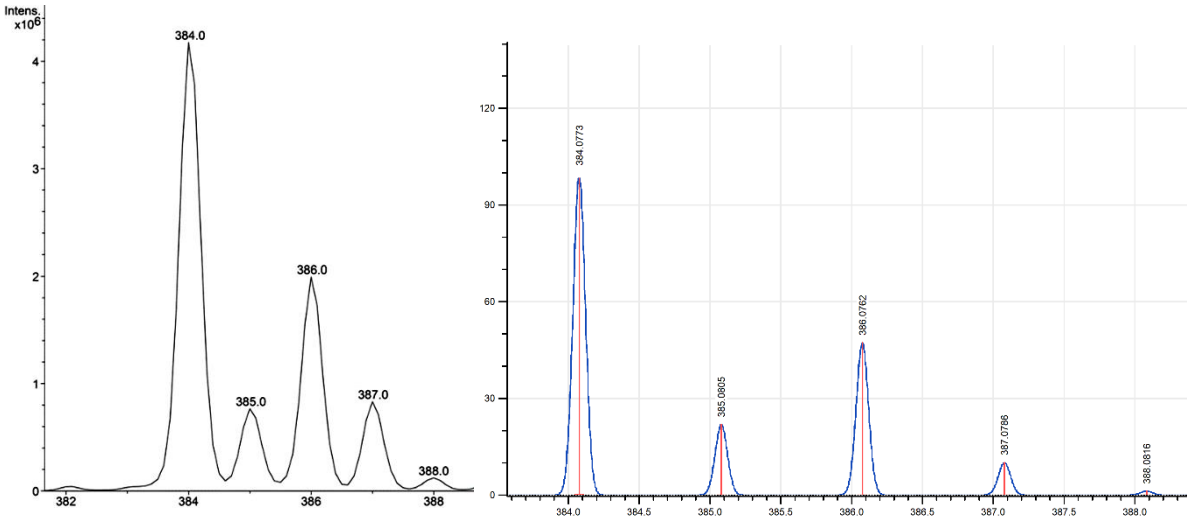

Figure S49. Comparison between the experimental (left) and calculated (right) isotopic pattern for $[CuL^1(OH)]^+$ (m/z = 384.0).

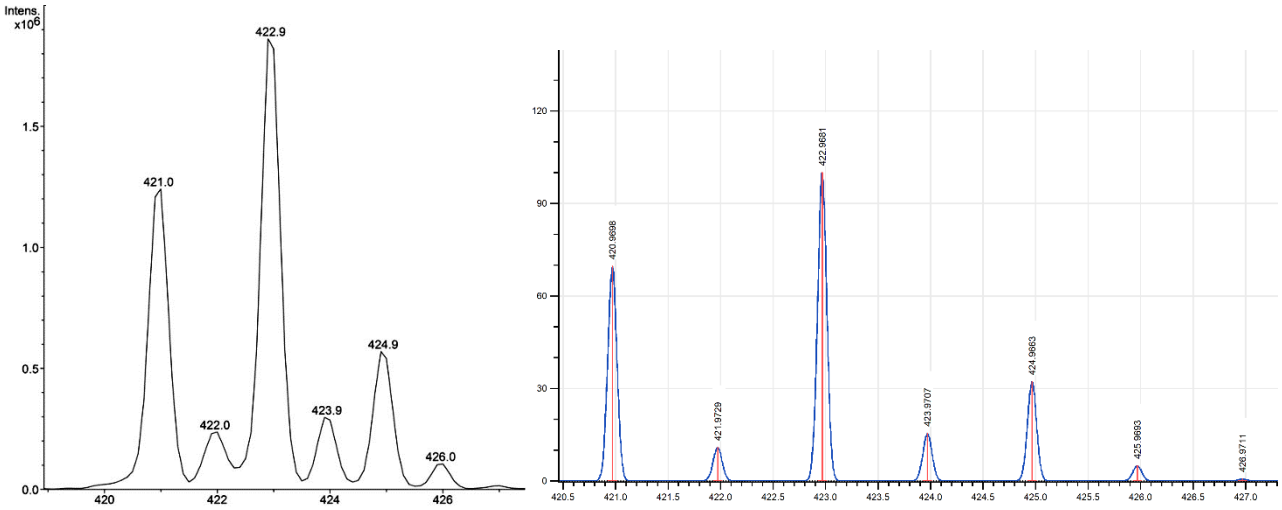

Figure S50. Comparison between the experimental (left) and calculated (right) isotopic pattern for $[CuL^{Cl}(H_2O)_2 + Br + HCO_2H)]^+$ (m/z = 420.9).

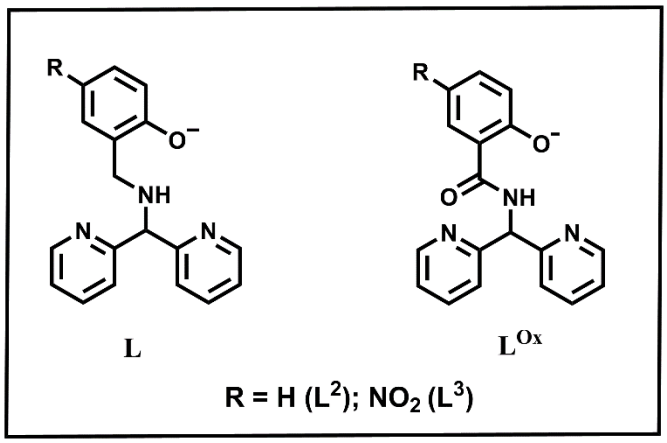

Figure S51. Schematic representation of the ligand oxidation during the reaction of $Cu_2L^2_2$ and $Cu_2L^3_2$ (200 μM) with H_2O_2 (30 mM) in BBS 50 mM.

Table S3. ESI-MS(+) molecular peaks for the $Cu_2L^x_2$ molecular ions.

Molecular ions	Assignment	Calculated (m/z)	Found (m/z)
$[Cu_2L^1_2]^{2+}$ (1)	$[Cu_2L^1_2 + OH]^+$ $[Cu_2L^1_2 + HCO_2]^+$ $[Cu_2L^1_2 + Br]^+$ $[Cu_2L^1_2 + ClO_4]^+$	751.2 779.2 813.1 833.1	751.1 779.1 813.0 833.0
$[Cu_2L^{Ox}L^{Cl}]^{3+}$ (2)	$[Cu_2L^{Ox}L^{Cl}(O)]^+$	657.1	657.0
$[Cu_2L^1L^{Cl}]^{3+}$ (2)	$[Cu_2L^1L^{Cl} + 2Br]^+$	785.0	784.9
$[CuL^1]^{2+}$ (3)	$[CuL^1 + OH]^+$	384.1	384.0
$[CuL^{Cl}]^{2+}$ (3)	$[CuL^{Cl} + HCO_2H + 2H_2O + Br]^+$	420.9	421.0
$[Cu_2L^2_2]^{2+}$	$[Cu_2L^2_2 + HCO_2]^+$ $[Cu_2L^2_2 + ClO_4]^+$	751.1 805.1	751.0 805.0
$[CuL^2]^+$	$[CuL^2]^+$	353.1	353.2
	$[CuL^2\text{-}2H]^+$	351.1	351.1
$[CuL^{2Ox}]^+$	$[CuL^{2Ox} + Br\text{-}2H]^+$	444.0	444.1
$[Cu_2L^3_2]^{2+}$	$[Cu_2L^3_2 + HCO_2]^+$ $[Cu_2L^3_2 + ClO_4]^+$	841.3 895.2	841.2 895.1
$[CuL^3]^+$	$[CuL^3\text{-}2H]^+$	396.1	396.1
	$[CuL^3 + OH + H_2O\text{-}2H]^+$	431.1	431.1
$[CuL^{3Ox}]^+$	$[CuL^{3Ox} + Br\text{-}2H]^+$	489.0	489.1

Exact mass calculated for the molecular ions : $[Cu_2L^1_2]$ = 734.2; $[Cu_2L^{Ox}L^{Cl}]$ = 641.1; $[Cu_2L^1L^{Cl}]$ = 627.1; $[CuL^1]$ = 367.1; $[CuL^{Cl}]$ = 260.0; $[Cu_2L^2_2]$ = 706.1; $[Cu_2L^3_2]$ = 816.2; $[CuL^2]$ = 353.1; $[CuL^{2Ox}]$ = 367.1; $[CuL^3]$ = 398.1; $[CuL^{3Ox}]$ = 412.1. The subtraction of two protons (-2H) indicates the formation of the corresponding ligand imine.

8. SOD-like Activity

SOD-like activity of the complexes was measured by using the cyt c assay, described by McCord and Fridovich, with some modifications.[S9] Screening of catalysts as SOD-mimicking systems was performed by spectrophotometric analysis of the inhibition of the superoxide-dependent reduction of the cyt c chromophore to ferricythocrome (Figure S52).

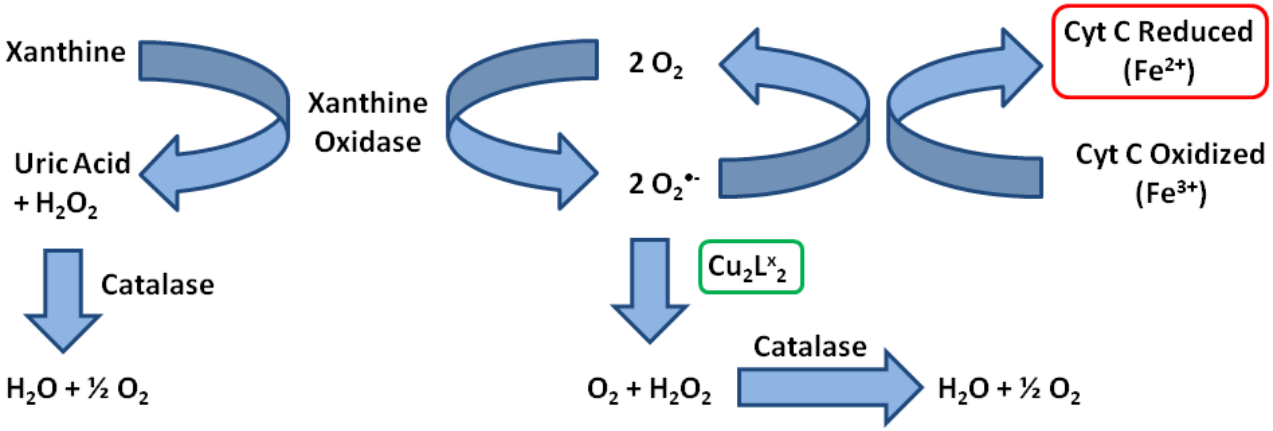

Figure S52. Scheme of cytchrome c assay for SOD activity. The green box highlight the function of the SOD active catalyst and in the red box is highlighted the chomophore monitored during the reaction.

The superoxide radical anions was generated by the xanthine/xanthine oxidase system. In all experiments, the reaction mixture was prepared with 40 µM xanthine, 10 µM cyt c, catalase 15 µg/ml, 50 mM phosphate buffer (pH=7.80) and xanthine oxidase 0.0053 U/ml. Catalyst solutions (64-550 nM) were prepared upon dilution of a stock solution in water. Possible interference through inhibition of the xanthine/xanthine oxidase reaction by test compounds was examined by following the rate of urate accumulation at 295 nm in the absence of cyt c.[S9] The concentration of the stock catalyst solutions was chosen in order to obtain approximately an inhibition interval of the superoxide-dependent reduction of the cyt c between 40-60 %. Among standard conditions the apparent rate constant, k_{McF} can be determined from the IC_{50} value as $k_{McF} = k_{cyt}[cyt]/IC_{50}$ (where k_{cyt} is 2.6×10^5 M^{-1} s^{-1}). Each experiment was performed in triplicate.

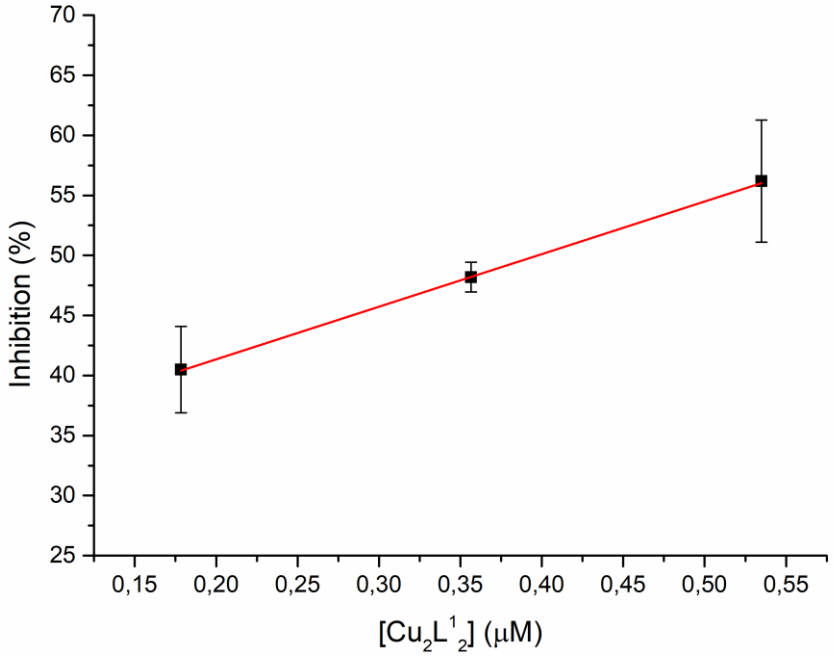

Figure S53. Plot of inhibition of cyt c reduction versus [$Cu_2L^1_2$], in 50 mM phosphate buffer at pH 7.8 25° C, 40 μM xanthine, 2 nM xanthine oxidase.

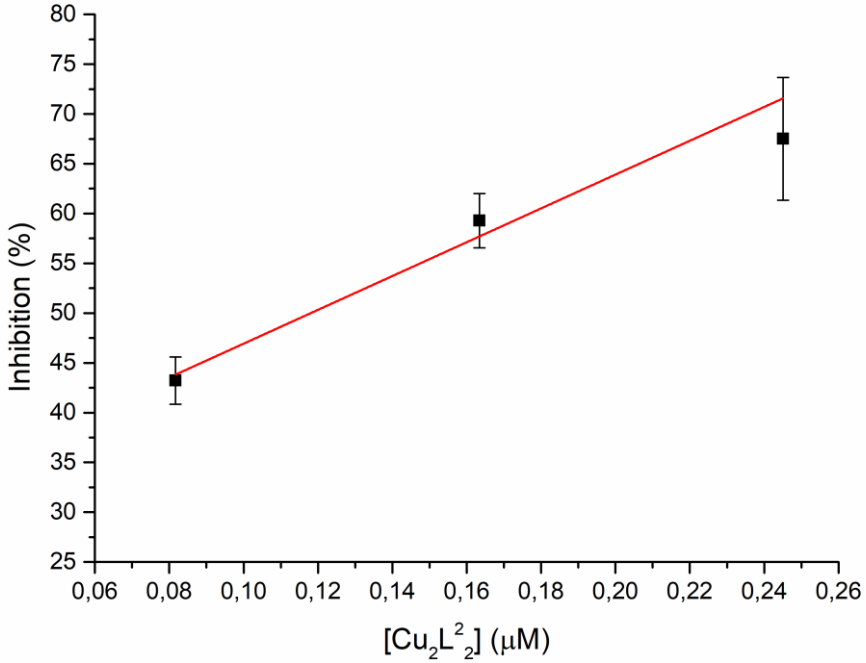

Figure S54. Plot of inhibition of cyt c reduction versus [$Cu_2L^2_2$], in 50 mM phosphate buffer at pH 7.8 25° C, 40 μM xanthine, 2 nM xanthine oxidase.

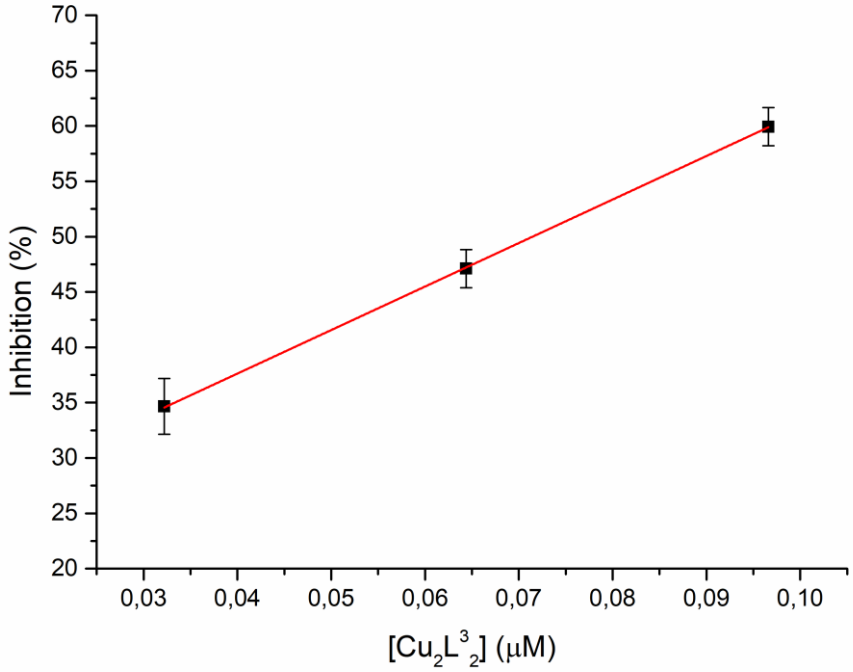

Figure S55. Plot of inhibition of cyt c reduction versus [$\mathbf{Cu_2L^3_2}$], in 50 mM phosphate buffer at pH 7.8 25° C, 40 μM xanthine, 2 nM xanthine oxidase.

9. CAT-like activity

CAT-like activity was determined by adding to a solution of H_2O_2 (30 mM) in BBS 50 mM (pH=7.8) or Krebs-Henseleit (KH) buffer (pH=7.4) (12 ml), 300 μL of a 8 mM acetonitrile solution of the $\mathbf{Cu_2L^x_2}$ complex to start the dismutation reaction. The reactor was maintained at 25 °C by a circulating thermostat, and the progress of reaction was determined by monitoring the pressure developed by molecular oxygen generated from dismutation of hydrogen peroxide into a closed vessel. The amount of O_2 was determined by continuous detection of pressure variation, through a pressure transducer. Initial rates were calculated by linear regression of data within 10 % H_2O_2 conversion. Kinetic runs were performed in triplicate. Control experiments performed without the Cu_2-based catalyst, confirmed that no oxygen evolution is detected from the buffer solution in the presence of H_2O_2.[S10]

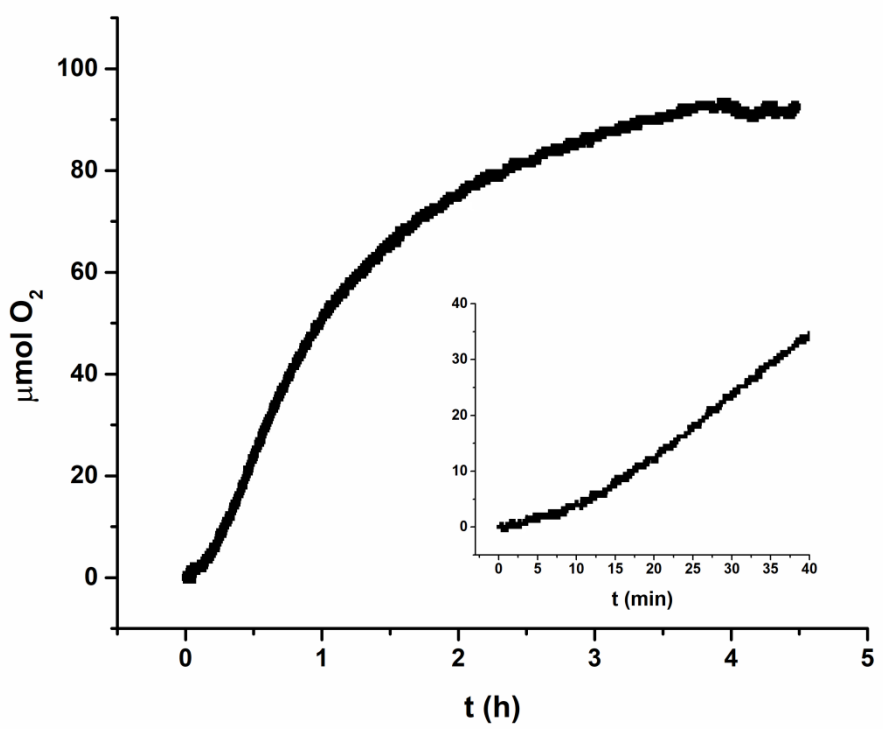

Figure S56. O_2 evolution kinetics by $\mathbf{Cu_2L^1_2}$ (200 µM) upon incubation with H_2O_2 (30 mM) at 25°C in borate buffer (50 mM, pH=7.8).

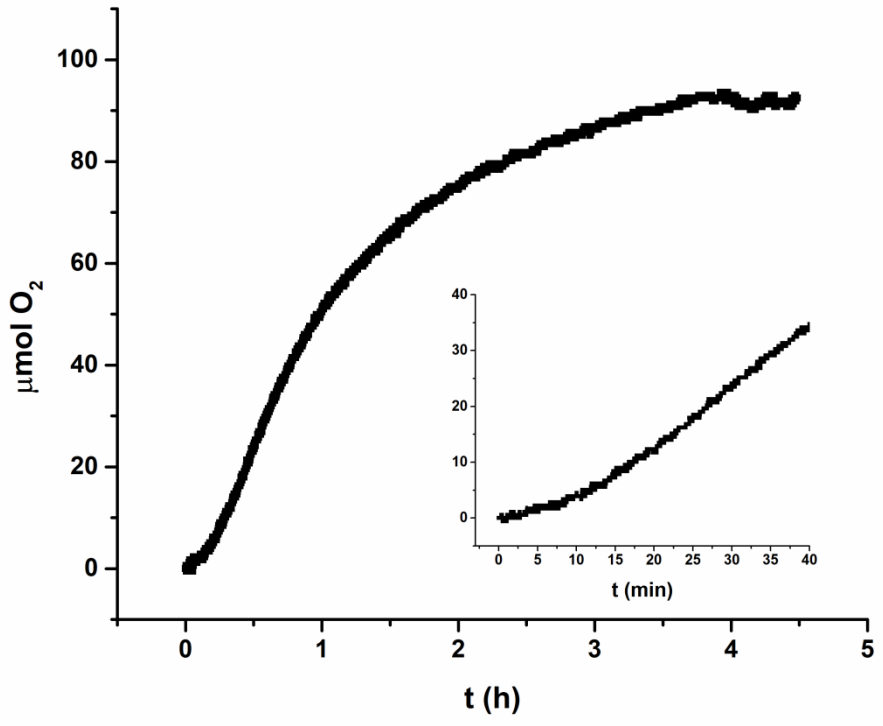

Figure S57. O_2 evolution kinetics by $\mathbf{Cu_2L^1_2}$ (200 µM) upon incubation with H_2O_2 (30 mM) at 25°C in KH buffer (pH = 7.4).

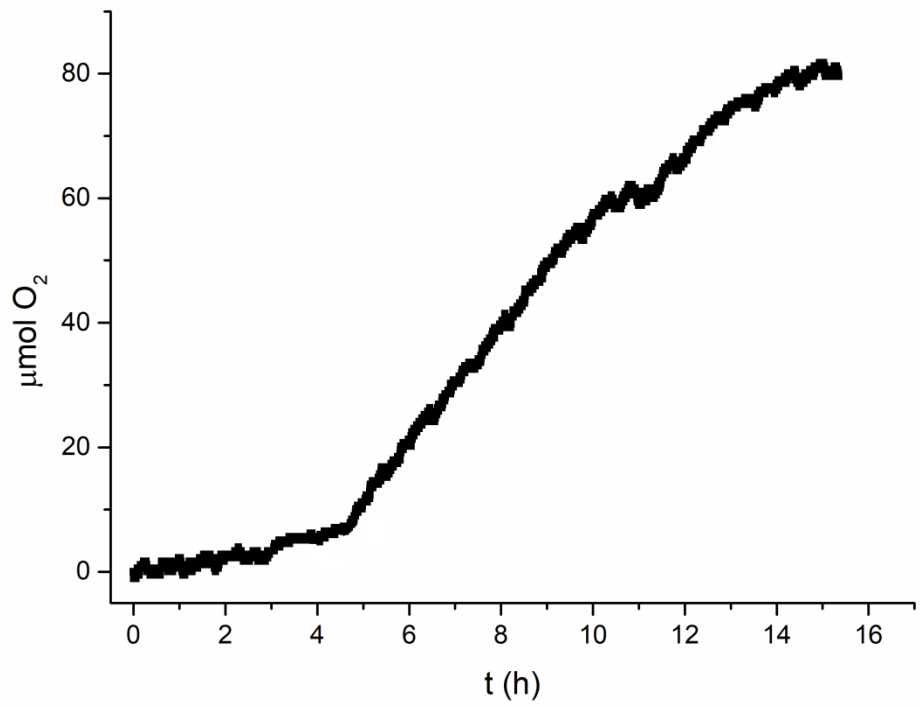

Figure S58. O_2 evolution kinetics by $\mathbf{Cu_2L^1_2}$ (200 µM) upon incubation with H_2O_2 (30 mM) at 25°C in phosphate buffer (20 mM, pH = 7.8).

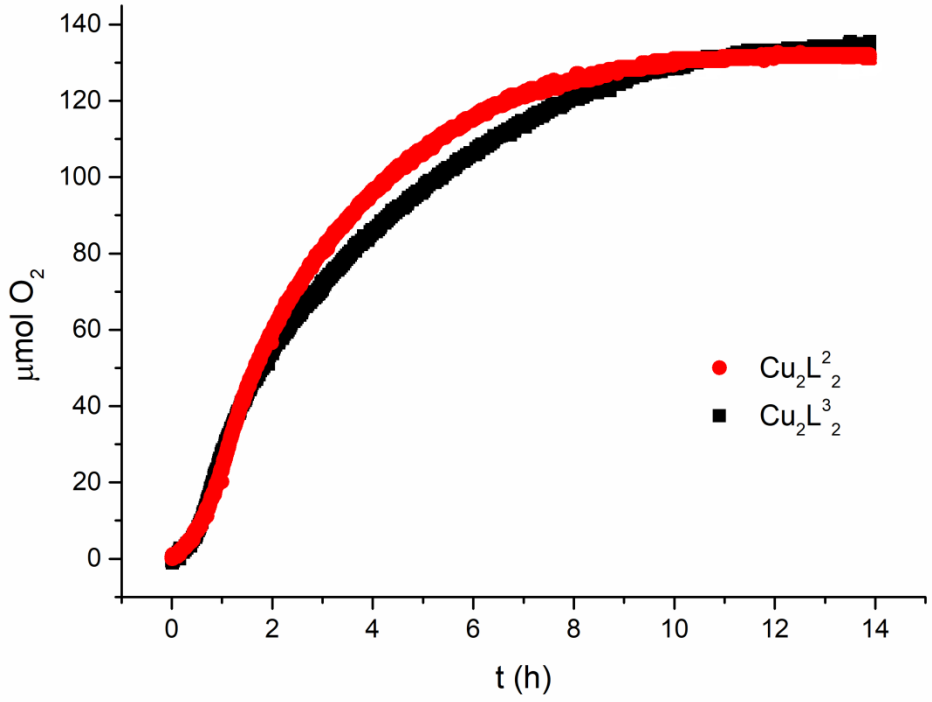

Figure S59. O_2 evolution kinetics by $\mathbf{Cu_2L^2_2}$ and $\mathbf{Cu_2L^3_2}$ (200 µM) upon incubation with H_2O_2 (30 mM) at 25°C in KH buffer (pH=7.4).

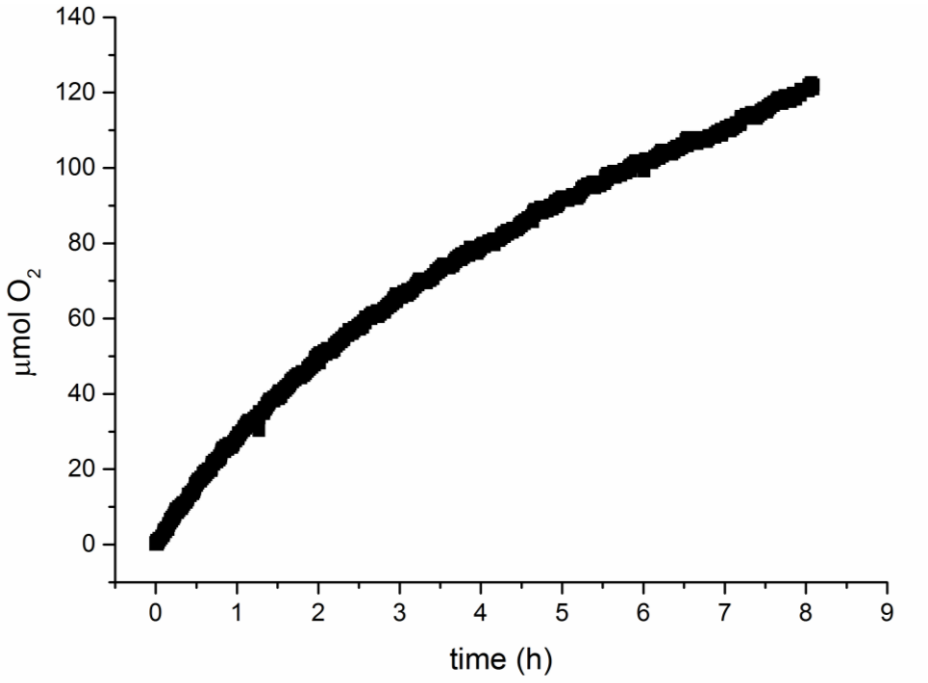

Figure S60. O_2 evolution kinetics by Cu^{2+} (400 µM) upon incubation with H_2O_2 (30 mM) at 25°C in borate buffer (50 mM, pH=7.8).

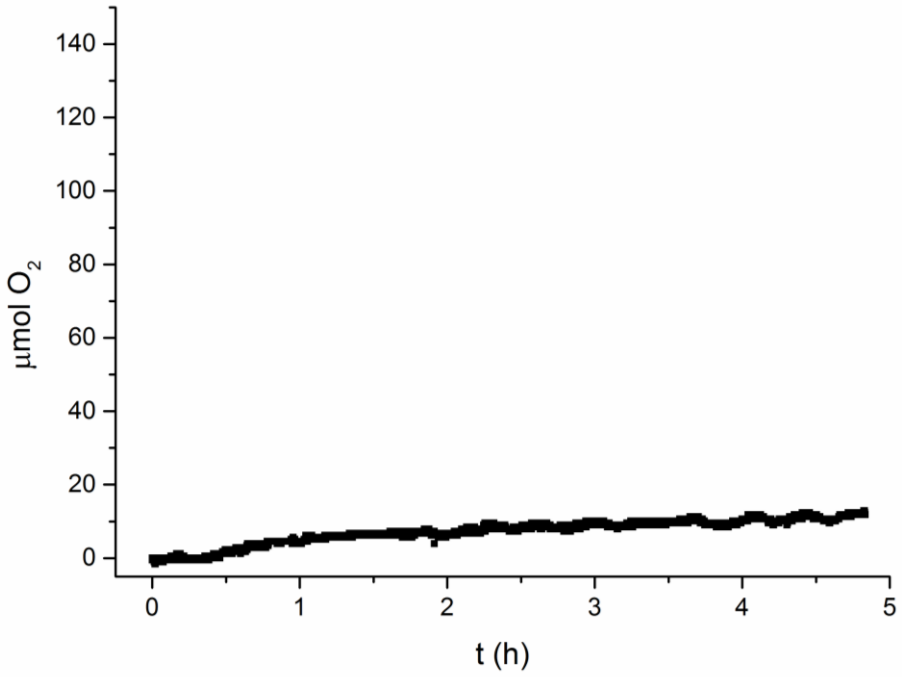

Figure S61. O_2 evolution kinetics by $\mathbf{Cu_2L^1_2}$ (200 µM) upon incubation with H_2O_2 (30 mM) at 25°C in acetonitrile.

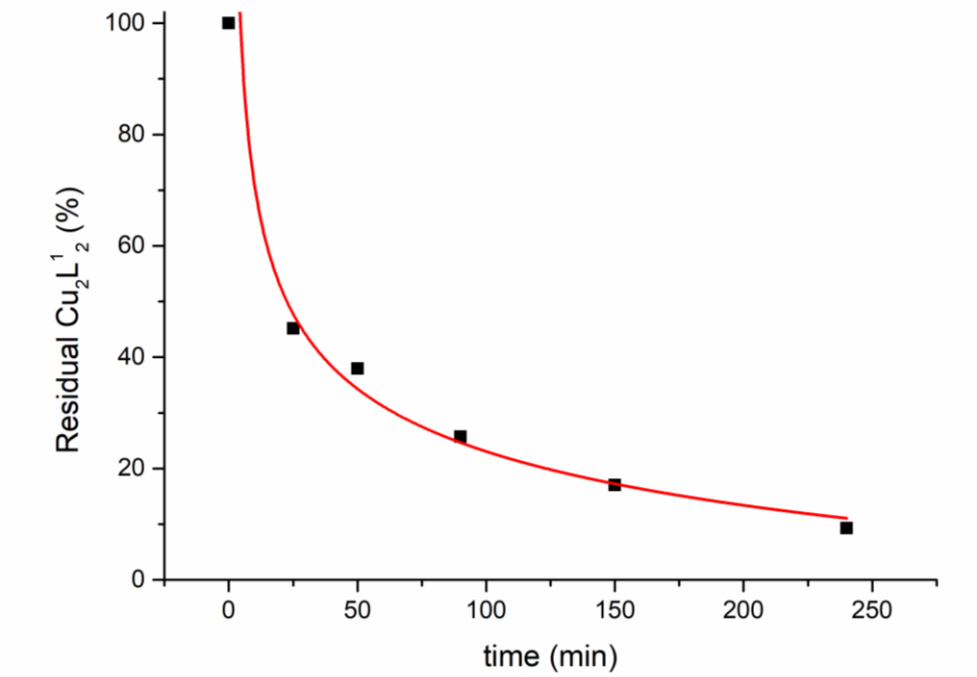

Figure S62. Kinetics profile of **$Cu_2L^1_2$** (200 μM) degradation with 30 mM H_2O_2 in acetonitrile, based on the molecular peak [**$Cu_2L^1_2$** $+ClO_4]^+$ (m/z = 833.0).

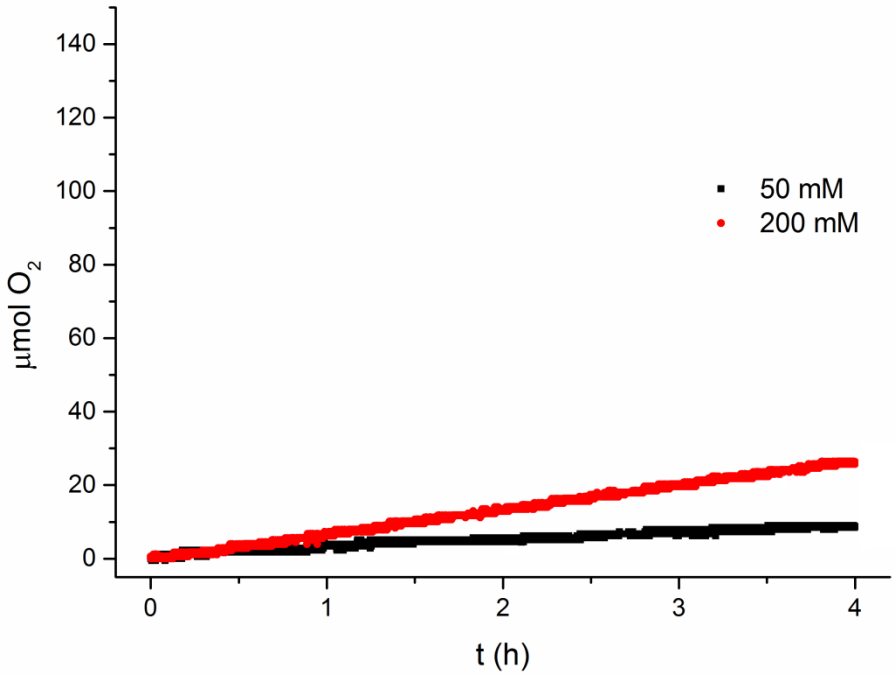

Figure S63. O_2 evolution kinetics by incubation of H_2O_2 (30 mM) at 25°C in borate buffer (50 mM, pH=7.8) with different concentration of NaBr.

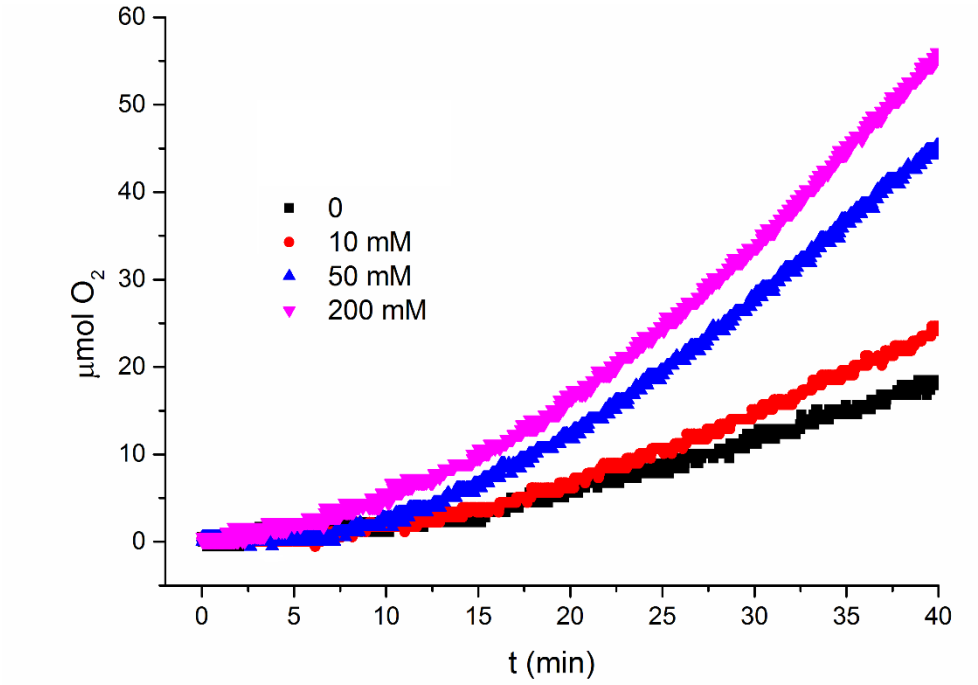

Figure S64. Initial lag phase in O_2 evolution kinetics by $\mathbf{Cu_2L^1_2}$ (200 µM) upon incubation with H_2O_2 (30 mM) at 25°C in borate buffer (50 mM, pH=7.8) in presence of different concentration of NaBr.

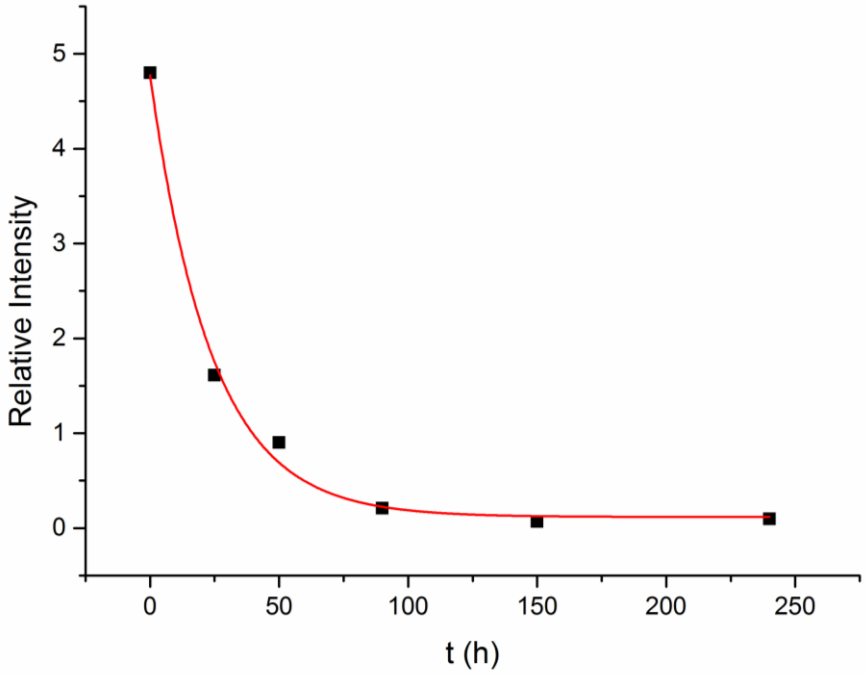

Figure S65. Kinetics profile of $\mathbf{Cu_2L^1_2}$ (200 µM) degradation with 30 mM H_2O_2 in borate buffer (50 mM, pH = 7.8).

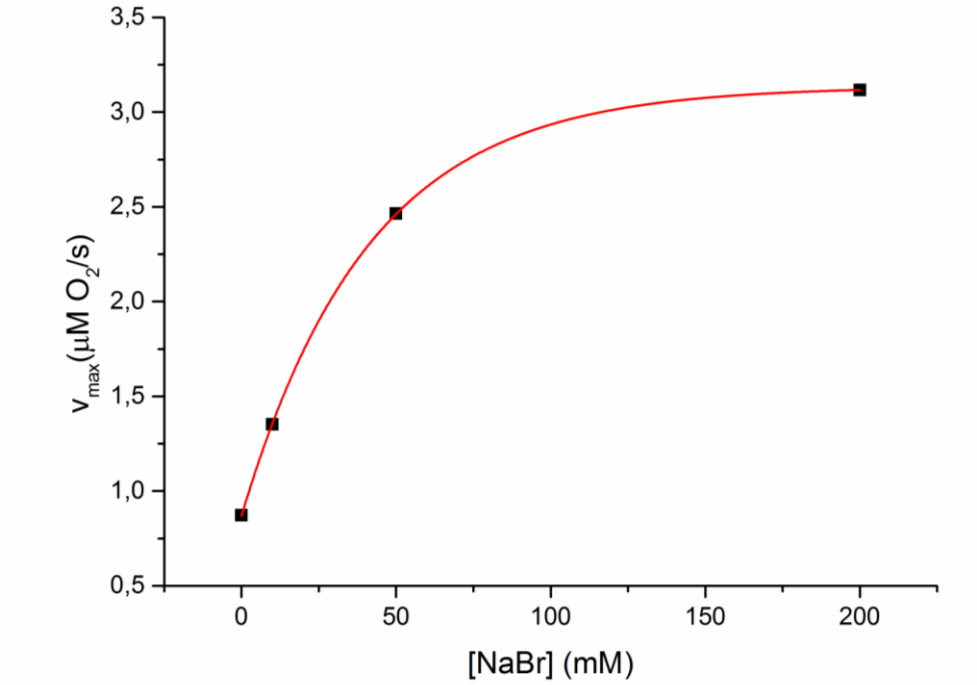

Figure S66. Dependence of the reaction rate of O_2 production with **$Cu_2L^1_2$** (200 μM) in borate buffer (50 mM, pH 7.8) in presence of NaBr at different concentration.

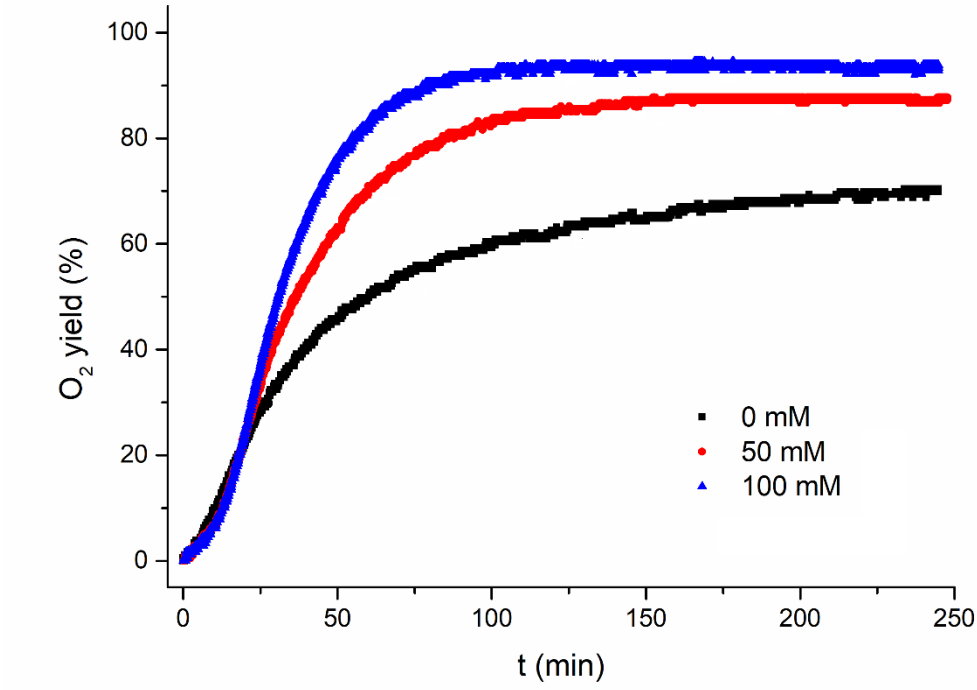

Figure S67. O_2 evolution kinetics by **$Cu_2L^2_2$** (200 μM) upon incubation with H_2O_2 (17 mM) at 25°C in borate buffer (50 mM, pH=7.8) with 0-100 NaBr.

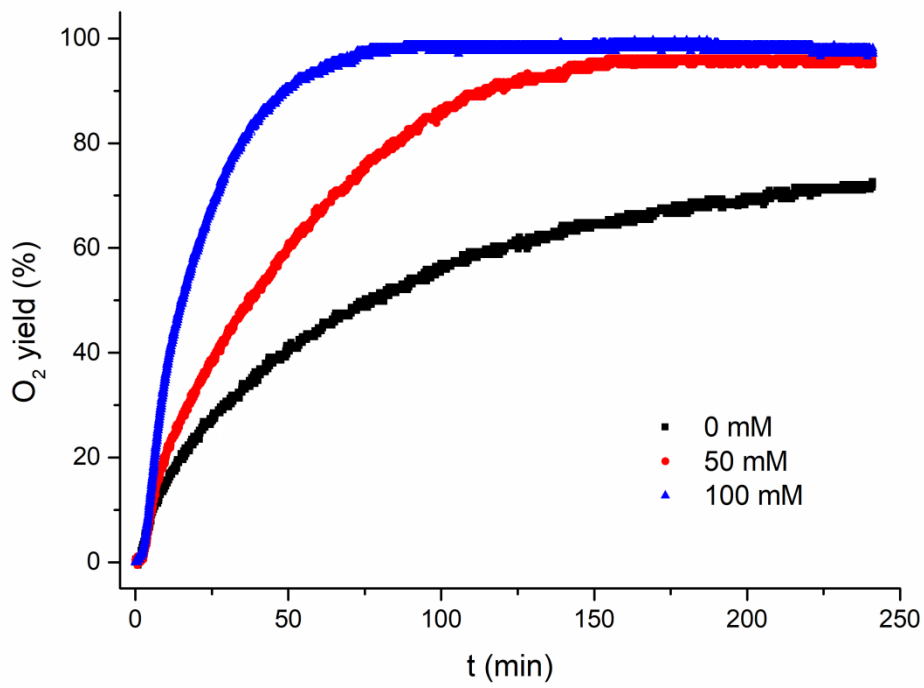

Figure S68. O_2 evolution kinetics by $Cu_2L^3_2$ (200 µM) upon incubation with H_2O_2 (17 mM) at 25°C in borate buffer (50 mM, pH=7.8) with 0-100 NaBr.

Table S4. Dependence of the reaction rate of O_2 production with $Cu_2L^2_2$ and $Cu_2L^3_2$ (200 µM) in presence of NaBr at different concentrations in BBS (50 mM, pH 7.8), H_2O_2 (17 mM).

	[NaBr] (mM)	R_{max}[a] (uM O_2/s)	Yield (%)	TON
$Cu_2L^2_2$	0	1.8	70	58
	50	2.8	87	73
	100	3.4	93	79
$Cu_2L^3_2$	0	2.2	72	61
	50	4.2	95	80
	100	7.4	>95[b]	83[b]

[a]R_{max} were obtained by linear regression of data within 10 % H_2O_2 conversion, the estimated errors are within ± 10%.[b] A small overestimation of the Yield and TON values is attributed to the slow reaction occurring between Br^- and H_2O_2 (see Figure S63).

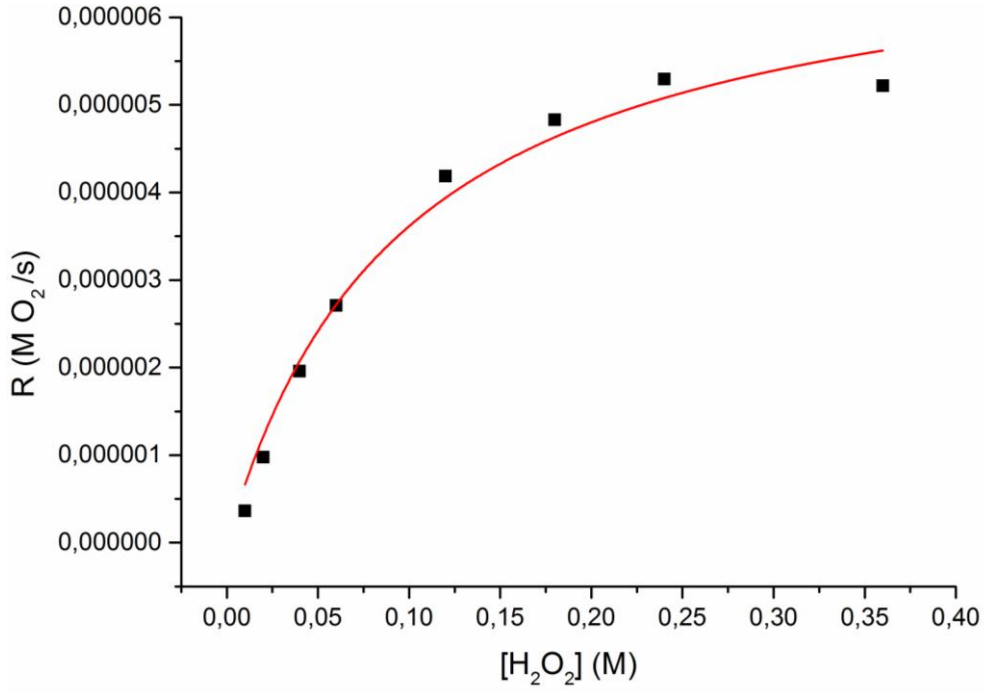

Figure S69. Effect of the H_2O_2 concentration on the disproportionation rate by **$Cu_2L^1_2$** (200 µM) at 25 °C in a borate buffer (50 mM, pH=7.8).

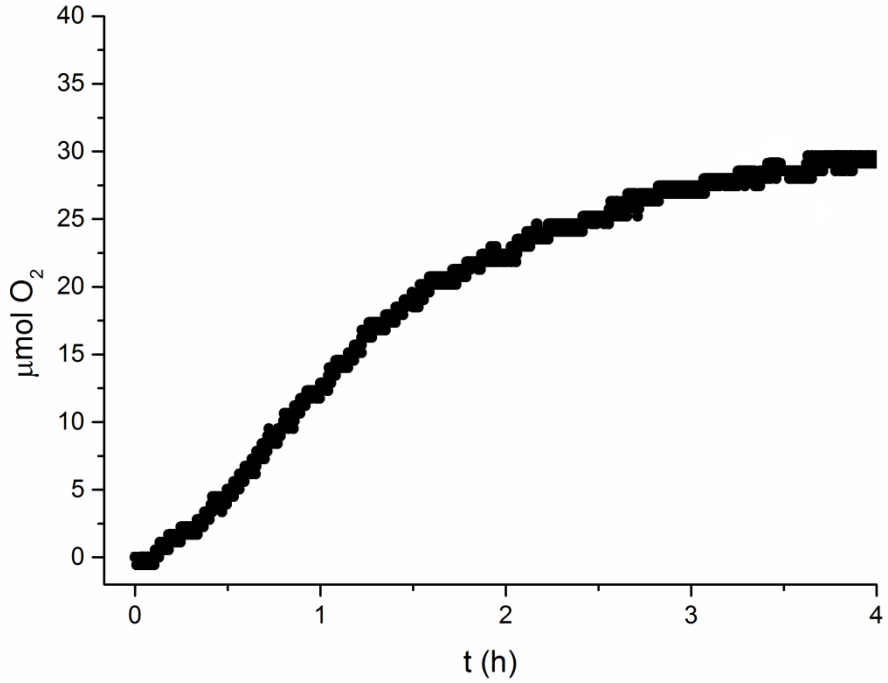

Figure S70. O_2 evolution kinetics by **$Cu_2L^1_2$** (200 µM) upon incubation with H_2O_2 (10 mM) at 25°C in borate buffer (50 mM, pH=7.8).

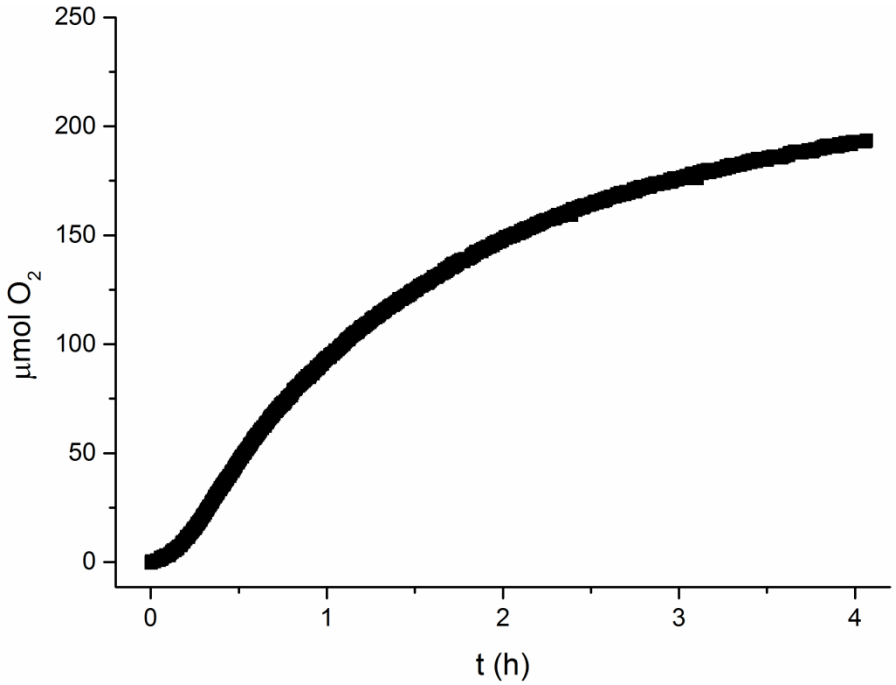

Figure S71. O_2 evolution kinetics by $\mathbf{Cu_2L^1_2}$ (200 µM) upon incubation with H_2O_2 (60 mM) at 25°C in borate buffer (50 mM, pH=7.8).

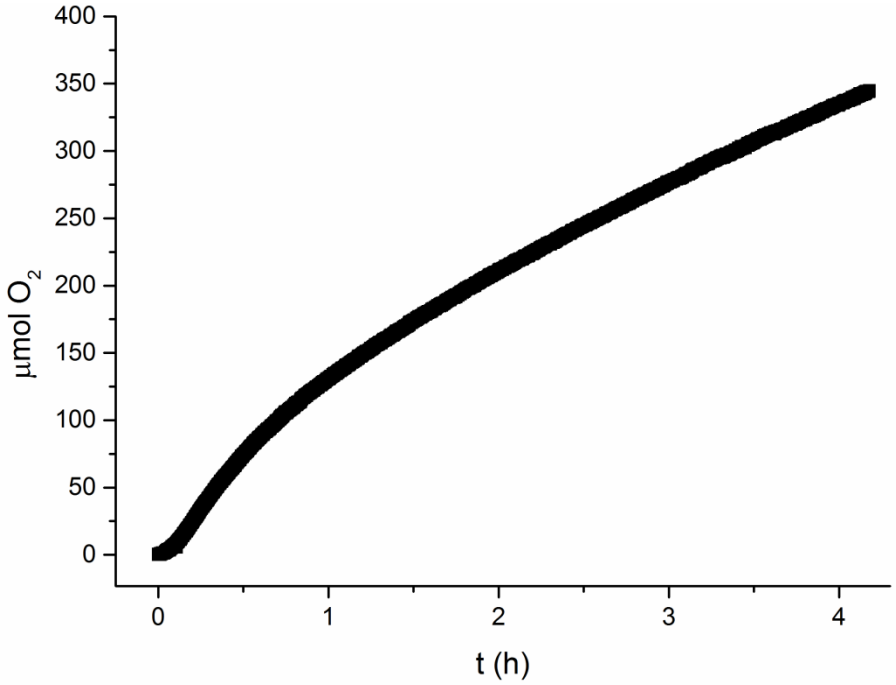

Figure S72. O_2 evolution kinetics by $\mathbf{Cu_2L^1_2}$ (200 µM) upon incubation with H_2O_2 (120 mM) at 25°C in borate buffer (50 mM, pH=7.8).

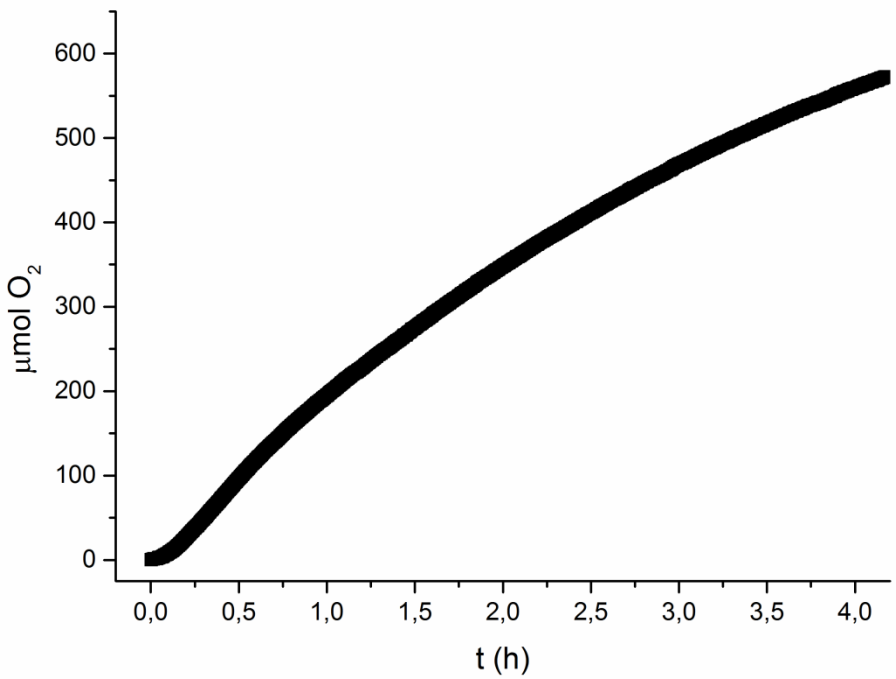

Figure S73. O_2 evolution kinetics by **$Cu_2L^1_2$** (200 µM) upon incubation with H_2O_2 (360 mM) at 25°C in borate buffer (50 mM, pH=7.8).

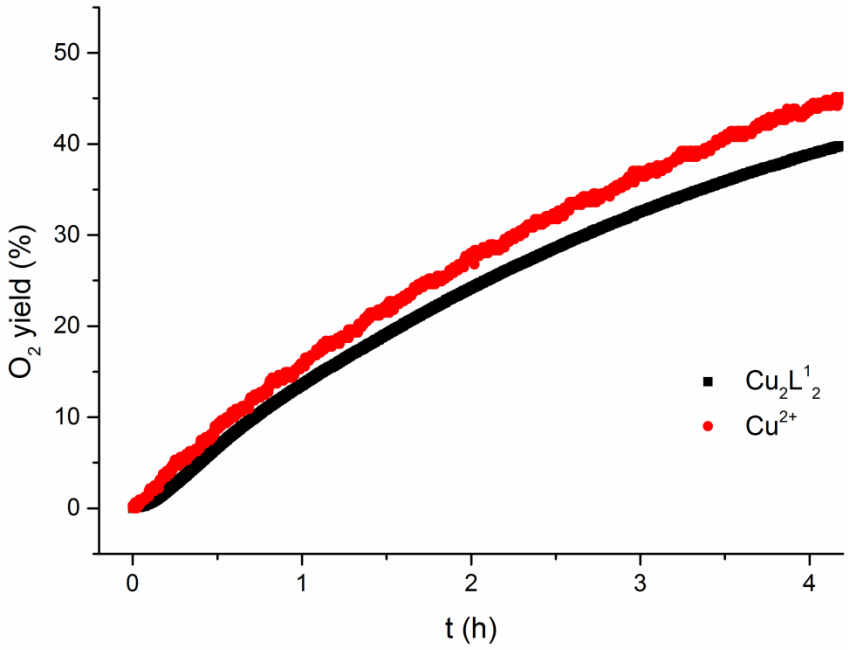

Figure S74. Comparison between the O_2 evolution kinetics by **$Cu_2L^1_2$** (200 µM) upon incubation with H_2O_2 (360 mM, black) and free copper (400 µM, red) upon incubation with H_2O_2 (30 mM) at 25°C in borate buffer (50 mM, pH=7.8).

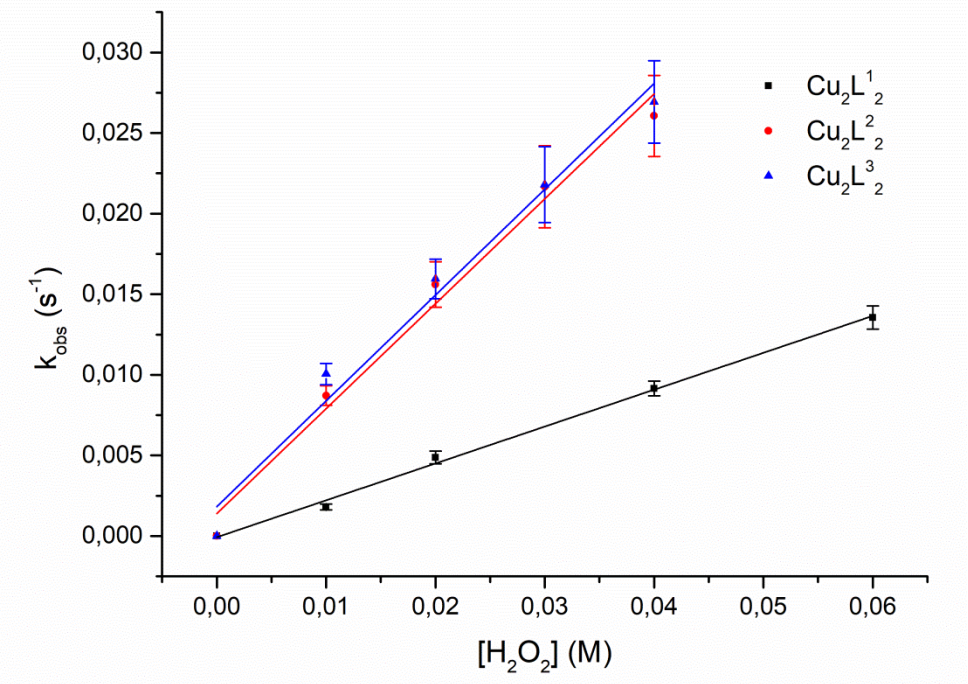

Figure S75. Linear dependence of pseudo-first-order rate constants k_{obs} on [H_2O_2], determined for hydrogen peroxide dismutation by **$Cu_2L^1_2$** (black), **$Cu_2L^2_2$** (red), **$Cu_2L^3_2$** (blue) (200 μM) at 25°C in borate buffer (50 mM, pH 7.8). The second-order rate constants was determined from linear plots of the observed k_{obs} vs [H_2O_2], $k_{obs} = k[H_2O_2]$.

10. EPR investigation

Sample preparation. EPR spectra of all three complexes were recorded before and after addition of H_2O_2 at 50 K. A 200 μM solution in BBS (50 mM pH=7.8) of each complex (150 μL) was mixed with a large excess of hydrogen peroxide (30 mM), immediately transferred to a quartz EPR tube and frozen putting the tube in dry ice. The total time from mixing to the complete freezing of the solution can be estimated to be around 3 minutes. When present, NaBr was added at a concentration of 50 mM.

Simulations. Spectral simulations have been performed with Easyspin (version 5.2.20).

Spin Quantitation. Quantitative measurements were performed for all samples using identical instrumental conditions, volume and position of the sample tube. First, the spectra were corrected by subtracting the baseline obtained as the spectrum of a sample of buffer solution without complex. Then, quantitation of the absolute number of paramagnetic species in each sample was achieved by double integration of the first derivative EPR spectra. The absolute concentration was obtained by comparing the double integral of each sample with that of a freshly prepared copper standard (Cu:EDTA 1:3, [Cu(II)] = 246 μM, volume 150 μL).

EPR Spectra of $Cu_2L^2_2$ and $Cu_2L^3_2$. In Figure S76, the evolution of the EPR spectra of **$Cu_2L^2_2$** and **$Cu_2L^3_2$** are reported. Before the addition of hydrogen peroxide, both complexes are diamagnetic

and decompose to the monomeric form as reported for the parent **$Cu_2L^1_2$** showing an analogous behaviour. In the presence of bromide, the breakdown to paramagnetic monomers is remarkably slowed down.

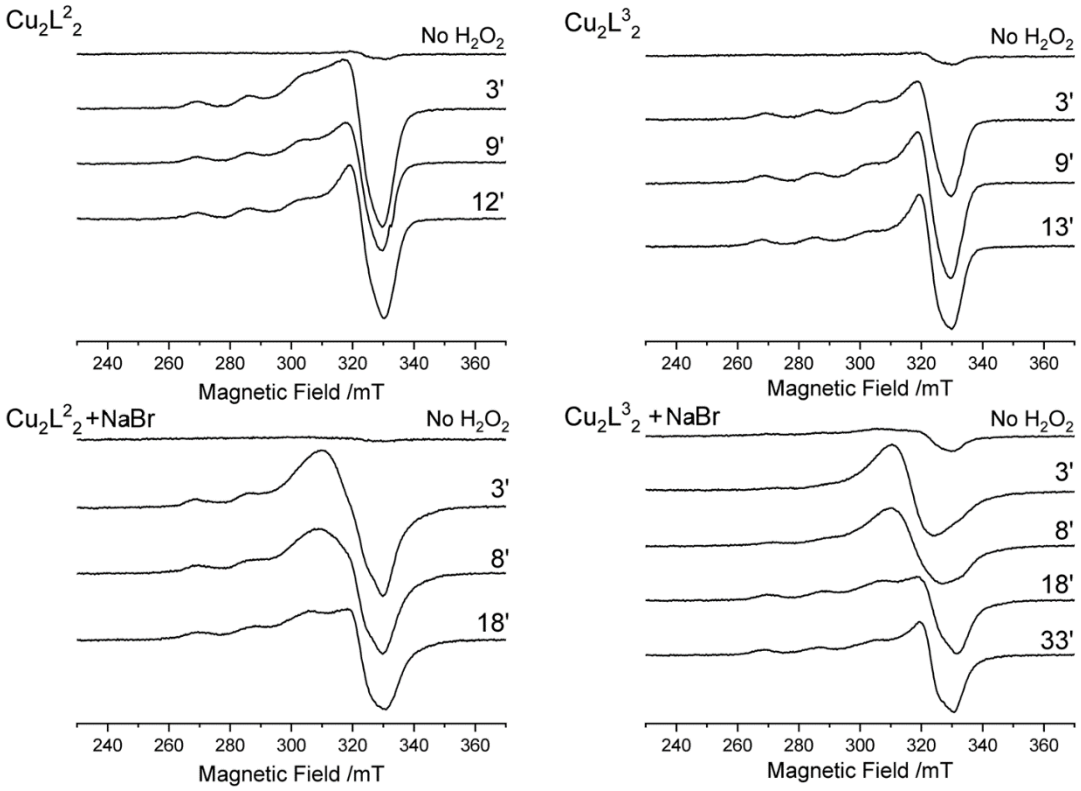

Figure S76. EPR spectra of **$Cu_2L^2_2$** (left) and **$Cu_2L^3_2$** (right) in the absence (top) or in the presence (bottom) of NaBr (50 mM).

11. Morin test

Pro-oxidant activity of the complexes was measured by following the oxidative degradation of morin in the presence of hydrogen peroxide by UV-Vis spectroscopy.[S11]

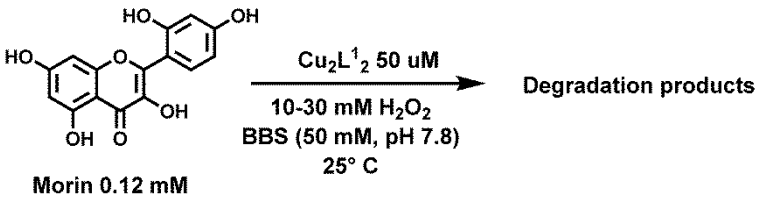

Scheme S1. Morin bleaching with H_2O_2 catalysed by $Cu_2L^1_2$.

The reactions were carried out in borate buffer (50 mM, pH 7.8) at 25°C over a period of 3 hours. A freshly prepared morin solution in DMSO was diluted in borate buffer to obtain a morin solution of 0.12 mM in all the experiments. To this mixture, a stock catalyst solution (1 mM) was added in order to obtain the desired catalyst concentration (50 μM). Finally, a commercial H_2O_2 stock

solution (30% w/w) was added to get a concentration between 10-30 mM. The change in the absorption maximum of morin at 390 nm was monitored at intervals of 10 min, to evaluate the peroxidase-like activity of the complexes. Considering the excess of hydrogen peroxide employed in the experiments we can extrapolate a pseudo-first order kinetic constant k_b, where $v = k_{obs} \cdot [morin]$. The value of k_b was obtained by linear regression of the initials rate of morin degradation at different hydrogen peroxide concentration (10-30 mM). Second-order rate constants were determined from linear regression of the observed pseudo-first-order rate constants vs $[H_2O_2]$.

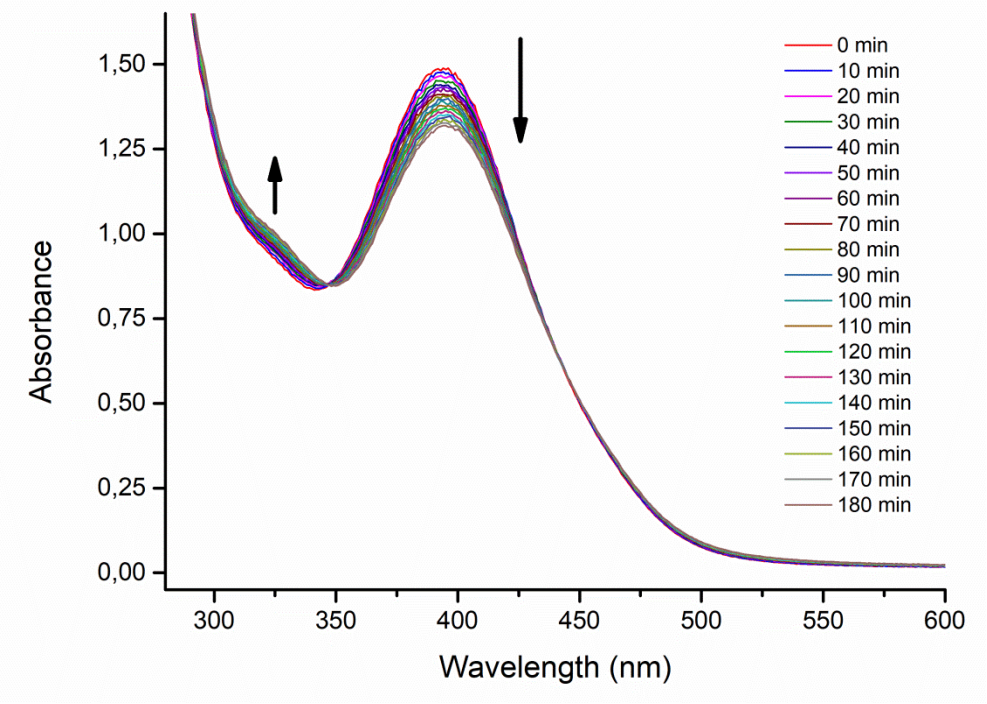

Figure S77. UV–visspectra over time of a 0.12 mM solution of morin in borate buffer (50 mM, pH 7.8) in the presence of 10 mM H_2O_2 and **$Cu_2L^1_2$** (50 µM).

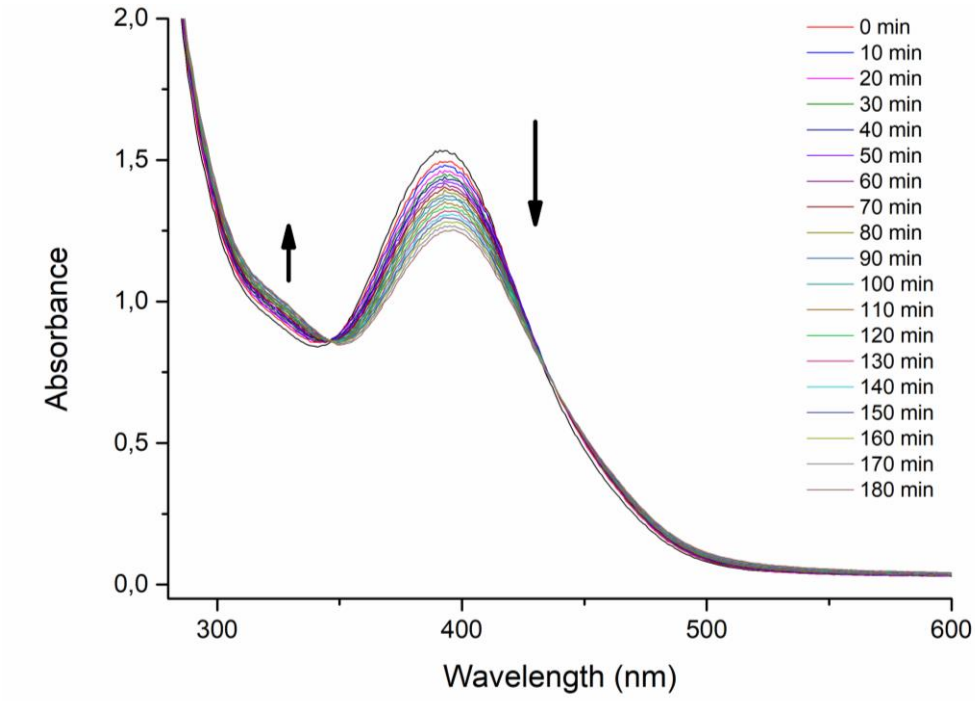

Figure S78. UV–vis spectra over time of a 0.12 mM solution of morin in borate buffer (50 mM, pH 7.8) in the presence of 20 mM H_2O_2 and $\mathbf{Cu_2L^1_2}$ (50 μM).

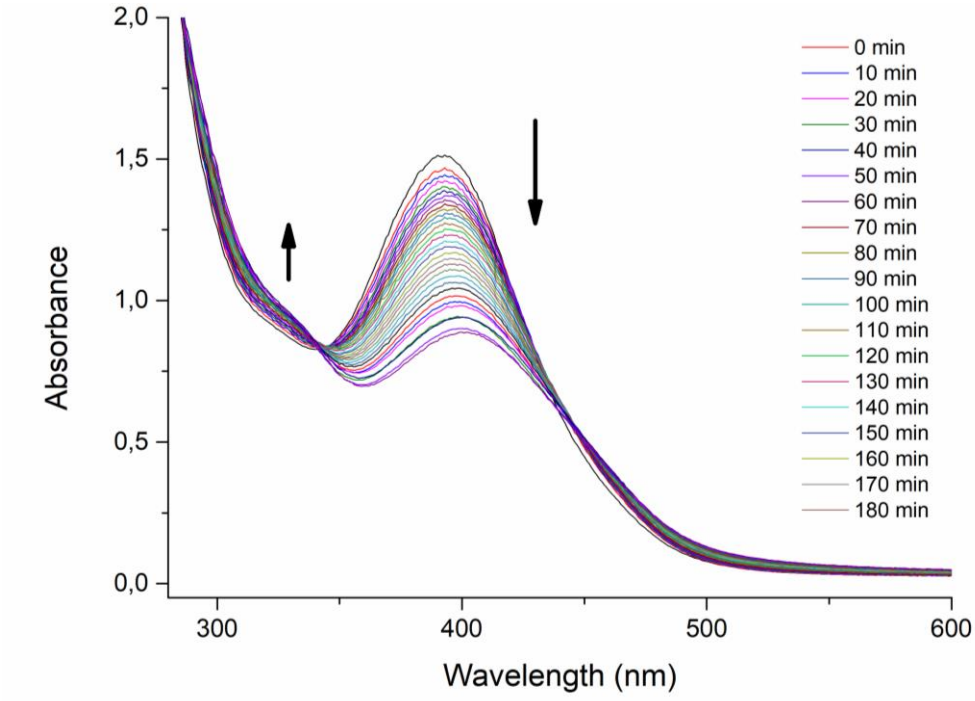

Figure S79. UV–vis spectra over time of a 0.12 mM solution of morin in borate buffer (50 mM, pH 7.8) in the presence of 30 mM H_2O_2 and $\mathbf{Cu_2L^1_2}$ (50 μM).

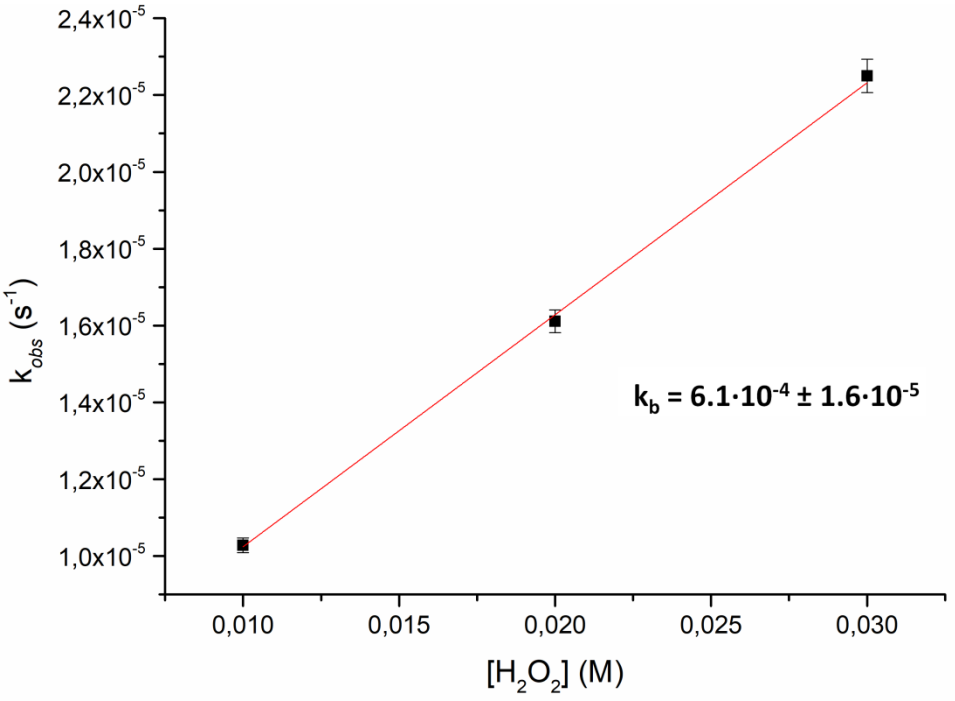

Figure S80. Linear dependence of pseudo-first-order rate constants k_{obs} on $[H_2O_2]$, varied in the range 10-30 mM, determined for oxidation of morin by **$Cu_2L^1_2$** (50 μM) at 25°C in borate buffer (50 mM, pH 7.8). The second-order rate constant was determined from linear plots of the observed k_{obs} vs $[H_2O_2]$, $k_{obs} = k_b[H_2O_2]$.

Table S5. Pseudo-first order rate constant k_{obs} and rate constant k_b for oxidative degradation of morin with $Cu_2L^1_2$.

	$[H_2O_2]$ (mM)		
	10	**20**	**30**
k_{obs} (s^{-1})	1.0×10^{-5}	1.6×10^{-5}	2.2×10^{-5}
k_b ($M^{-1}s^{-1}$)		6.1×10^{-4}	

Table S6. Pro-oxidant and anti-oxidant activity for catalytic anti-oxidants.

	k_{H2O2} ($M^{-1}s^{-1}$)	k_b ($M^{-1}s^{-1}$)	*p*	Ref.
$Cu_2L^1_2$	0.23 [a]	6.1×10^{-4} [d]	377	this work
Mn_2L_2P2	1890 [b]	116 [e]	16	[S8]
$[Cu(PBMPA)]^+$	0.030 [c]	181 [d,f]	~10^{-4}	[S11]

Mn_2L_2P2 obtained by the self-assembly of Mn_2L_2 (HL = HL^1) and P2 (Mn-meso-tri(N-methylpyridinium-4-yl)mono(N-4-carboxybenzyl-4-pyridyl) porphyrin); HPBMPA = N-propanoate-N,N-bis-(2-pyridylmethyl)amine (see also Table 1). [a] Based on oxygen evolution kinetics, monitored by a pressure transducer (see Table 1).[b] Based on oxygen evolution kinetics, monitored using a Clark electrode, [catalyst] = 10 μM, $[H_2O_2]$ = 0.1−10 mM in BBS 50 mM pH 7.8 at 25 °C. [c] Based on graduate burette method [catalyst] = 0.5 mM, $[H_2O_2]$ = 0.23 M in PBS 0.1 M pH 11 at 20 °C. [d] Based on morin bleaching monitored by UV-vis, $[Cu_2L^1_2]$ = 50 μM and [Cu(PBMPA)] = 2.5 μM, $[H_2O_2]$ = 10−30 mM. [e] Based on Mn-porphyrin bleaching monitored by UV-vis, [catalyst] = 10 μM, $[H_2O_2]$ = 50−200 μM. [f] calculated from the reported pseudo-first order $k_{app} = k_b[H_2O_2] = 1.81\ s^{-1}$ with $[H_2O_2]$ = 0.01 M.

12. References

[S1] Vicario, J.; Eelkema, R.; Browne, W. R.; Meetsma, A.; La Crois, R. M.; Feringa, B. L. Catalytic Molecular Motors: Fuelling Autonomous Movement by a Surface Bound Synthetic Manganese Catalase. *Chem. Commun.*, **2005**, 3936-3938.

[S2] La Crois R.M.; Manganese Complexes as Catalysts in Epoxidation Reactions A Ligand Approach, PhD dissertation, University of Groningen, NL, **2000.**

[S3] Kabsch, W.; XDS. *Acta Crystallogr., Sect. D: Biol. Crystallogr.* **2010**, *66*, 125−132.

[S4] Kabsch, W.; Integration, Scaling, Space-Group Assignment and Post-Refinement. *Acta Crystallogr., Sect. D: Biol. Crystallogr.* **2010**, *66*, 133−144.

[S5] Burla, M. C.; Caliandro, R.; Carrozzini, B.; Cascarano, G. L.; Cuocci, C.; Giacovazzo, C.; Mallamo, M.; Mazzone, A.; Polidori, G. Crystal Structure Determination and Refinement *via SIR2014*. *J. Appl. Crystallogr.* ***2015***, *48*, 306−309.

[S6] Sheldrick, G. M. A Short History of *SHELX*. Acta Cryst. **2008**, *A64*, 112−122.

[S7] Farrugia, L.J. WinGX and ORTEP for Windows: an Update. *J. Appl. Cryst.* **2012**, *45*, 849−854.

[S8] Squarcina, A.; Sorarù, A.; Rigodanza, F.; Carraro, M.; Brancatelli, G.; Carofiglio, T.; Geremia, S.; Larosa, V.; Morosinotto, T.; Bonchio, M. Merged Heme and Non-Heme Manganese Cofactors for a Dual Antioxidant Surveillance in Photosynthetic Organisms. *ACS Catal.* **2017**, 7, 1971 − 1976.

[S9] McCord, J. M.; Fridovich, I. Superoxide dismutase. An Enzymic Function for Erythrocuprein (Hemocuprein). *J. Biol. Chem.* **1969** 244, 6049-6055.

[S10] Grau, M.; Rigodanza, F.; White, A. J. P.; Sorarù, A.; Carraro, M.; Bonchio, M.; Britovsek, G. J. P. Ligand Tuning of Single-Site Manganese-Based Catalytic Antioxidants with Dual Superoxide Dismutase and Catalase Activity. *Chem. Commun.*, **2014**, 35, 4607-4609.

[S11] Pap, J.S.; Kripli, B.; Bors, I.; Bogáth, D.; Giorgi, M.; Kaizer, J.; Speier, G. Transition Metal Complexes Bearing Flexible N_3 or N_3O Donor Ligands: Reactivity Toward Superoxide Radical Anion and Hydrogen Peroxide. *J. Inorg. Biochem.,* **2012**, 117, 60-70.